

Alma Mater Studiorum – Università di Bologna

DOTTORATO DI RICERCA IN

GEOFISICA

Ciclo XXVIII

**Settore Concorsuale di afferenza:** 04/A4

**Settore Scientifico disciplinare:** GEO/10

**MORPHOMETRIC ANALYSIS OF MOUNT ETNA LAVA FLOWS  
USING HIGH RESOLUTION DIGITAL ELEVATION MODELS**

**Presentata da:** Alessandro Fornaciai

**Coordinatore Dottorato**

Prof.ssa Daria Pinardi

**Relatore**

Dott. Massimiliano Favalli

**Esame finale anno 2017**

*A Ginevra,  
perché in fondo tutto  
quello che faccio,  
lo faccio per essere  
un padre migliore*

---

# Contents

---

<b>Contents</b>	<b>i</b>
<b>Acknowledgements</b>	<b>iv</b>
<b>Abstract</b>	<b>vi</b>
<b>List of Figures</b>	<b>vii</b>
<b>List of Tables</b>	<b>x</b>
<b>Abbreviations</b>	<b>xi</b>
<b>1. Introduction</b>	<b>1</b>
1.1 Digital Elevation Model. An introduction	1
1.1.1 Topographic surface and morphometric parameters	1
1.1.2 Digital Elevation Models (DEMs). Definition, data structure and sources	2
1.1.3 Spatial and temporal DEM resolutions	4
1.2 Airborne Light Detection and Ranging (LiDAR) system	7
1.2.1 Airborne LiDAR data generation	8
1.3 Structure from Motion (SfM) photogrammetry	10
1.3.1 Single, stereo and multi-view photogrammetry	10
1.3.2 Structure from Motion methods	12
1.4 Research goal and structure of the thesis	15
<b>2. Detection of topographic changes and quantification of eruptive products on Mount Etna (Sicily, Italy) by multi-temporal LiDAR acquisitions</b>	<b>19</b>
2.1 High-resolution LiDAR dataset of Mount Etna	21
2.2 Volume calculation from multi-temporal LiDAR-derived DEMs	25
2.3 Mount Etna eruptive activity from 2004 to 2010	26
2.3.1 2004-05 Mount Etna eruption	26
2.3.2 2006 Mount Etna eruption	27
2.3.3 2007-2010 eruptive events	30
2.4 2004-05 lava flow volume	32
2.5 Volume and dynamics of the 2006 lava flow	35

2.6	Topographic change detection from 2007 to 2010	38
<b>3.</b>	<b>Visualization and comparison of DEM-derived parameters. Application to lava flows</b>	<b>41</b>
3.1	Grid to grayscale image conversion and image enhancement	42
3.2	DEM-derived surface parameters	43
3.2.1	Shaded relief maps	45
3.2.2	Slope, aspect and curvature maps	47
3.2.3	Topographic position index (TPI) and deviation from mean elevation (DEV) index	48
3.2.4	Roughness maps	49
3.2.5	Sky View Factor	51
3.2.6	Openness maps	54
3.3	Image combination	55
3.4	Surface parameter comparison	57
3.5	Case studies. Roques Blancos phonolitic lava flow	62
3.6	Discussion	63
<b>4.</b>	<b>LiDAR-derived morphometry of Etna's channel-fed lava flows</b>	<b>67</b>
4.1	Channel-fed lava flow morphometry. An introduction	68
4.2	Method for extracting morphometric parameters from DEM	70
4.3	Morphometric analysis of selected channel-fed lava flows	74
<b>5.</b>	<b>UAV-based remote sensing surveys and Structure from Motion technique for generating a very-high-resolution DEM of 1974 Mount Etna Lava flow</b>	<b>82</b>
5.1	The 1974 Mount Etna flank eruption	84
5.2	UAV field survey of the 1974 lava flow	85
5.3	DEM and orthomosaic generation	87
5.3.1	SfM DEM generation	87
5.3.2	SfM DEM accuracy	90
5.3.3	DEM-derivative maps	90
5.4	A 20-cm versus 1-m DEMs: Qualitative and quantitative analysis	91
5.4.1	Interpretation of lava flow surfaces	92
5.4.2	Crust structures: a tripartite classification and flow regime association	92
5.4.3	Qualitative analysis of surface folds	95

5.5	Hazard assessment applications	96
<b>6.</b>	<b>Conclusions</b>	<b>101</b>
	<b>References</b>	<b>106</b>

---

## Acknowledgements

---

Quando ti ritrovi a prendere un Dottorato a 42 anni compiuti, senti di dover ringraziare poche persone. La prima di esse è certamente la mia, a breve, sposa Silvia. Devo ringraziarla perché se non ci fosse stata lei ad insistere affinché mi imbarcassi in questa follia con Ginevra in arrivo, mai e poi mai mi sarei sognato di iniziare un dottorato. Non solo si è sobbarcata il peso della mie assenze durante le lunghe trasferte a Bologna (mai dimenticherò il suo sorriso quando stremata la sera metteva fra le mie braccia Ginevra di pochi mesi) e nei numerosi fine settimana dedicati allo studio e alla stesura della tesi, ma soprattutto devo ringraziarla perché la sua determinazione ha sostituito la mia nei momenti più difficili e mi ha permesso di arrivare fino in fondo.

Devo anche certamente ringraziare Raffaella perché anche lei ha fortemente voluto che mi buttassi in questa avventura. Ogni volta che Silvia insisteva nel volermi far prendere il dottorato, mi rifugiavo in ufficio per sottrarmi alle sue insistenze e lì trovavo Raffaella determinata e pronta a continuare le pressioni iniziate fra le mura domestiche. Ovviamente devo ringraziare Paolo perché mi ha permesso di fare il dottorato nonostante l'enorme carico di lavoro che ero chiamato a svolgere sotto la sua supervisione, ma anche, e soprattutto, perché i suoi preziosi consigli hanno permesso di dare a questo lavoro l'ultima e decisiva svolta finale.

Vorrei evitarlo, ma sono costretto anche a ringraziare Massimiliano: mio supervisore, collega, amico e, se non fa cavolate nel frattempo, fra pochi mesi anche testimone di nozze. Ha sempre detto che non ce l'avrei fatta, ma ha fatto di tutto affinché ce la facessi. Secondo lui io ho sempre avuto due problemi (da un punto di vista lavorativo, s'intende): uno era che non avevo il dottorato e l'altro che non volevo andare via da Pisa. Dato che adesso il dottorato me lo ha fatto quasi prendere, mi chiedo se a breve inizierà a lavorare per spedirmi il più lontano possibile da lui.

Sento di dover ringraziare anche Luca, perché senza di lui sopportare Massimiliano sarebbe stato troppo gravoso per un semplice assegnista di ricerca. Ma non solo, grazie alla sue abilità di pilota, ho imparato a contenere la mia ansia quando vedo il drone in volo.

Infine, vorrei ringraziare Laura, paziente insegnante di inglese, e il professor Michele Dragoni e la professoressa Daria Pinardi per la competenza, professionalità e disponibilità più volte evidenziate in questi quattro lunghi anni di dottorato.

---

## Abstract

---

Morphometric analysis of lava flows provides crucial information for a better understanding of the processes of lava flow dynamics and emplacement. In this thesis, high-resolution digital elevation models (DEMs) obtained by the airborne LiDAR system and the Unmanned Aerial Vehicle - Structure from Motion system are used for an extensive morphometric analysis of the Mount Etna (Italy) lava flow. A digital comparison of pre- and post-eruptive LiDAR DEMs of Etna was made to quantify the lava volumes emitted in the 2004-2005, 2005-2006 and 2007-2010 intervals. The total erupted volume of 2004-2005 is  $\sim 63.3 \times 10^6 \text{ m}^3$  entirely emitted by the 2004-05 eruption. The total erupted volume of 2005-2007 is  $\sim 42.0 \times 10^6 \text{ m}^3$ , of which  $\sim 33.5 \times 10^6 \text{ m}^3$  emitted by the September-December 2006 eruption. The total erupted volume of 2007-2010 is  $>86 \times 10^6 \text{ m}^3$ , most of which ( $\sim 74 \times 10^6 \text{ m}^3$ ) is formed by the lava flows of the 2008-2009 flank eruption. Lava flow morphometric analysis was performed over LiDAR DEM for eleven channel-fed lava flows through a semi-automatic procedure and using *SVF* and openness down parameters to better detect and delimit surface-specific elements, i.e. lava levees, base and channel-bed. The results show an inverse relation between slope and channel width, a certain coherence between average slope of levees and pre-emplacing slope, and the same trend between the channel width and channel-bed width. Finally, in order to investigate less costly methods for producing DEMs, we created a high-resolution DEM of the 1974 lava flow using the UAV-SfM system and then we compared it with the LiDAR-derived DEM. The UAV-SfM system can be effectively used to produce topographic data for large areas with an accuracy and resolution that are even higher than those of the LiDAR system. Therefore, the UAV-SfM system can be effectively used to update the topography of active volcanic areas with reasonable costs and short time of deployment.

---

## List of Figures

---

- Figure 1.1 The suitable cell size for DEM interpolation.
- Figure 1.2 LiDAR system.
- Figure 1.3 The basic principles of stereo-photogrammetry.
- Figure 1.4 Bundle adjustment in multi-view photogrammetry.
- Figure 2.1 Hillshaded map of Mt. Etna derived from TINITALY DEM
- Figure 2.2 LiDAR data acquired during the 2004 and 2005 campaigns over Mount Etna.
- Figure 2.3 LiDAR data acquired during the 2006 campaigns on Mount Etna.
- Figure 2.4 LiDAR data acquired during the 2007 and 2010 campaigns on Mount Etna.
- Figure 2.5 Sketch representing the main Mount Etna activity phases between two successive LiDAR surveys.
- Figure 2.6 The 2004-05 lava flow field
- Figure 2.7 LiDAR point density map focused on the area involved in the 2004-05 lava field.
- Figure 2.8 The 2006 lava field.
- Figure 2.9 LiDAR point density map of the east flank of the volcano inundated by the 2006 lava flow.
- Figure 2.10 Maps of eruptive products emitted from 2007 to 2010.
- Figure 2.11 LiDAR point density map in the area interested by the 2007-2009 activity.
- Figure 2.12 The 2004-05 lava flow imaged on 16 September 2004.
- Figure 2.13 Thickness map of the 2004-05 lava flow field.
- Figure 2.14 DEM difference maps calculated from the 2005, 2006 and 2007 LiDAR data set.

- Figure 2.15 DEM showing thicknesses of deposits (mostly lava flows) of the eruptive activity between the 2007 and 2010 LiDAR surveys.
- Figure 3.1 Mount Etna test area.
- Figure 3.2 Shaded relief maps of an area of 1200 m × 1200 m on Mt. Etna.
- Figure 3.3 Slope, aspect, curvature, *TPI* and *DEV* maps of an area of 1200 m × 1200 m on Mt. Etna.
- Figure 3.4 Roughness maps for an area of 1200 m × 1200 m on Mt. Etna
- Figure 3.5 The *SVF* is defined by the ratio of the solid angle ( $W_{sky}$ ) of the visible sky above a certain observation point.
- Figure 3.6 Sky view factor (*SVF*) and openness maps for an area of 1200 m × 1200 m on Mt. Etna.
- Figure 3.7 Examples of map composition for an area of 1200 m × 1200 m on Mt. Etna.
- Figure 3.8 Matrix of the squared correlations.
- Figure 3.9 Matrix of the squared correlations among the quantities considered in this paper.
- Figure 3.10 Extraction of the main features from a lava channel belonging to the Roques Blancos lava flow (Tenerife Island).
- Figure 4.1 Orthophoto of a sector of Mount Etna's 1974 lava flow field overlaid on the shade relief derived from high resolution DEMs.
- Figure 4.2 Conceptual scheme of the flow unit morphological elements and morphometric parameters measured by the morphometric tool:
- Figure 4.3 Main steps of the morphometric analysis procedure.
- Figure 4.4 Selected lava flow.
- Figure 4.5 Summary of plot of selected morphometric data.
- Figure 5.1 UAV-data-derived orthophoto mosaic of Mt. Etna's 1974 lava flow.
- Figure 5.2 The platform and sensor system used during the survey operation.
- Figure 5.3 Flight plan for the survey of the 1974 lava flow field.
- Figure 5.4 Point density distributions of the SfM and LiDAR 3D models.
- Figure 5.5 Specific zone extracted from the 3 cm orthomosaic image showing the cm-scale grain distribution of the lava surface at different scales.
- Figure 5.6 SfM and LiDAR DEMs difference quantifies the displacement and show its distribution.

- Figure 5.7 SfM-UAV and LiDAR DEMs qualitative comparison of a selected zone.
- Figure 5.8 Openness down map of a selected area including a dispersed flow and lava channel of two different flows, calculated from the SfM-UAV DEM.
- Figure 5.9 1974 lava flow profiles measured on DEMs with corresponding *S*-spectrum plots.
- Figure 5.10 1974 lava flow profiles measured on DEMs with corresponding *S*-spectrum plots.

---

## List of Tables

---

Table 2.1 The Mount Etna LiDAR data base of INGV

Table 4.1 Notation of all parameters.

Table 4.2 Selected lava channels with the eruption and the year of post- and pre-emplacment of DEMs.

---

## Abbreviations

---

AGL	Above Ground Level
ALTM	Airborne Laser Terrain Mapper
BN	Bocca Nuova
CMRU	Control Monitoring and Recording Unit
DEM	Digital Elevation Model
DEV	DEVIation from mean elevation
DGPS	Differential GPS
DJI	Dà-Jiāng Innovations
ENAC	Ente Nazionale per l'Aviazione Civile
GCP	Ground Control Point
GIS	Geographic Information System
GPS	Ground Position System
IDW	Inverse Distance Weight
IMU	Inertial Measurements Unit
INGV	Istituto Nazionale di Geofisica e Vulcanologia
InSAR	Interferometry SAR
LA	Laser Altimeter
LCU	LiDAR Control Unit
LiDAR	Light Detection And Ranging
LRU	Laser Ranging Unit
MDF	Mount De Fiore
MSV	Multiview stereo matching
MtB	Monti Barbagallo
MtC	Monti Centenari
MtS	Monte Simone
NEC	North East Crater

NN	Nearest Neighbor
NSEC	New South East Crater
OMSD	Opto Mechanical Scanning Device
PCS	POS Computer System
POS	Position Orientation System
RC	Rocca Capra
RM	Rocca Musarra
RMS	Root Mean Square
RRIM	Red Relief Image Map
SAPR	Sistemi Aeromobili a Pilotaggio Remoto
SAR	Synthetic Aperture Radar
SC	Serracozzo
SEC	South East Crater
SfM	Structure from Motion
SGS	Serra Giannicola
SIFT	Scale Invariant Feature Transform
SRTM	Shuttle Radar Topography Mission
SVF	Sky View Factor
TIN	Triangular Irregular Network
TPI	Topographic Position Index
UAV	Unmanned Aerial Vehicle
VdB	Valle del Bove
VOR	Voragine

---

# Chapter 1

---

## Introduction

### 1.1 Digital Elevation Model. An introduction

#### 1.1.1 Topographic surface and morphometric parameters

Topography<sup>1</sup> is one of the main factors controlling the flow and emplacement of lava flows (e.g. Greg and Fink 2000; Harris 2013; Tarquini et al., 2012; Favalli et al., 2012a). At the same time, as a result of the interaction between erupting conditions, lava rheology and Earth's surface, topography of solidified lava flow reflects the dynamics of flow during the eruption (Griffiths 2000; Lev and James 2014; Dieterich et al., 2015). Topographic change detection has been the most accurate method for quantifying the effusive products emitted during an eruption (Favalli et. al., 2009, 2010a, 2011; Cashman et al., 2013; Behncke et al., 2016; Bagnardi et al., 2016). Consequently, qualitative and quantitative topographic information has been widely used in lava flow studies, first as topographic maps (Stevens et al., 1999) and since the mid-1950s mainly as Digital Elevation Models (DEMs) (e.g. Mazzarini et al., 2005, 2007; Favalli et al., 2010a), i.e. a two-dimensional discrete function of the elevation.

The topographic surfaces<sup>2</sup> are used for approximating the real Earth's surfaces, which are too complex for a rigorous mathematical treatment owing to their coarseness and irregularity (Shary 2008). A topographic surface can be defined mathematically as a closed, oriented and continuously

---

<sup>1</sup> From the Greek word *τοπος* (place) and *γραφειν* (to draw).

<sup>2</sup> In this thesis, the term topographic surface is referred to the Earth's surface, in particular as a contact surface between the lithosphere and atmosphere.

differentiable two-dimensional manifold  $S$  in a three dimensional Euclidean space  $E^3$  (Florinsky 2016).

A topographic surface can be described by a continuous single-valued bivariate function  $z = f(x, y)$ , where elevation  $z$  depends on plan coordinates  $x, y$ . It follows that  $z$  has only one value for any location  $(x, y)$  (Cayley 1859). This restriction is a simplification that means that caves, grottos, and similar landforms are not considered topographic surfaces. Other restrictions (Evans 1979; Mark 1979; Shary 1991, 1995; Florinsky 2016) are the following: i) Function  $z$  is smooth, i.e. the topographic surface has derivatives of all orders; ii) The topographic surface is situated in a uniform gravitational field, where the gravitational acceleration vector is parallel to the Z-axis and directed downward; iii) The planar size of the topographic surface is essentially less than the Earth's radius; iv) The topographic surface is a scale-dependent surface (Clarke 1988), which means that the fractal component of topography can be considered as a high-frequency noise.

A morphometric (or topographic) variable (or parameter) is a single valued bivariate function  $v = u(x, y)$  describing properties of the topographic surface (Florinsky, 2016). Morphometric variables derive directly from the elevation and can be classified as local and regional variables (Olaya 2009). Local variables describe the geometry of the topographic surface in the vicinity of each point of the surface (Florinsky 2016) and can be divided into geometric (i.e. slope, aspect and curvature) and statistical (e.g. roughness) variables. Regional morphometric variables describe a relative position of a point on the surface (e.g. catchment area) (Florinsky, 2016). Florinsky (2016) also introduces structural lines (i.e. ridge and valley lines), solar and combined variables. Relevant local morphometric variables for the aim of this thesis are described in detail in Chapters 3 and 4.

### **1.1.2 Digital Elevation Models (DEMs). Definition, data structure and sources**

In computer science, a land surface is generally represented as Digital Elevation Model (DEM), a two-dimensional, discrete function of elevation of the topographic surface. When physically measuring the value of the surface, it is impossible to collect data for every point on the surface, which comprises an infinite number of points (El-Sheimy et al., 2005). Modern mapping technologies collect a sample  $S$  of  $N$  arbitrary points  $(x, y, z)$  and reconstruct the continuous surface  $z = f(x, y)$  by interpolating the points in  $S$ . Continuous surfaces derived from the 3D point dataset with known coordinates  $(x, y, z)$ , which are called point clouds, are generally represented either as regular grid DEM or as Triangular Irregular Network (TIN) model (Li et al., 2004; Shary 2008; Hengl and Evans 2009).

A triangulated irregular network (TIN) is a vector data structure where the starting points are arranged into polygons that share common points and lines. TIN is implemented using the triangulation method (Akima 1978), which consists in calculating triangles, usually following the

Delaunay criteria, with apices at the starting points. Delaunay triangulation produces a set of triangles that are as equiangular as possible. The resulting TIN contains the actual measurements (not the derived values) and also keeps the original irregular point distribution, which is more effective for describing complex land surfaces (Shary 2008; Hengl and Evans 2009).

A regular grid DEM is essentially a rectangular matrix of heights ( $z$ ) sampled at regular intervals in both the  $x$  and  $y$  planes (Fig. 1.1). Each grid cell has one single elevation value, which is usually obtained by interpolation among adjacent sampled points. Square grid DEM is the most frequently used DEM data structure, because it is the simplest and most efficient approach for storing and manipulating data (Wilson and Gallant 2000; Hengl and Evans 2009).

DEMs can have (almost) global, national and local coverage (Li et al., 2004). Global DEMs provide topographic data covering almost the entire globe (e.g. 90-m Shuttle Radar Topography Mission - SRTM DEM; <http://www2.jpl.nasa.gov/srtm>). Local DEMs describe small (or very small) areas with high accuracy and resolution. They are largely generated by laser scanning, photogrammetry and terrestrial geodesy methods. A national (or regional) DEM covers an area with size between local and global surfaces (e.g. TINITALY for Italy, Tarquini et al., 2012a).

Various techniques have been used for acquiring DEM data sources; however, the majority have now been replaced by the less labour-intensive remote sensing methods (Li et al. 2004; Nelson et al., 2009; Florinsky 2016), which include:

- 1) Stereo and multi-view photogrammetry. Knowing the geometry of acquisition, stereo-photogrammetry derives elevation information from a stereo-pair of aerial photographs, imaging an area with sufficient overlap and using Ground Control Points (GCPs). The multi-view photogrammetry method solves the camera pose and scene geometry simultaneously and automatically through the automatic identification of matching features in multiple images (Westoby et al., 2012). Multi-view photogrammetry methods are detailed in Section 1.3 and used for the data of Chapter 5.
- 2) Synthetic Aperture Radar (SAR) techniques. SAR is a group of active remote sensing techniques, characterized by an antenna that transmits electromagnetic radiation at microwave frequencies to the target and receives the echoes reflected by the target. The most widely used SAR techniques to generate DEMs are the interferometric SAR (InSAR) (Florinsky 2016), which uses phase-difference measurements derived from a pair of radar images of the same area, taken at slightly different positions, to derive the topographic map of the target.
- 3) Laser Altimetry (LA) technique. LA is a group of active remote sensing techniques where a laser altimeter emits laser pulses and a receiver detects the reflected signal from the ground surface. The time delay between transmission and reflection is recorded and the distance from the altimeter and the target is calculated considering the speed of light (Baltsavias 1999a, b and c; Wehr and Lohr 1999). Airborne and terrestrial light detection and ranging (LiDAR) are

laser altimetry technologies. The Airborne LiDAR system is detailed in Section 1.2, and used for the data of Chapters 2, 3 and 4.

### 1.1.3 Spatial and temporal DEM resolutions

A grid is a matrix with fixed resolution. Although it has a number of serious disadvantages, what makes a grid attractive is that most of its properties are only controlled by the resolution (Hengl, 2006). A grid resolution is expressed as cell size ( $w$ ), which is defined as the distance between two grid nodes of a mesh equally spaced in  $x$  and  $y$ , usually expressed in a metric system (Fig. 1.1) (Hengl and Evans 2009). The larger the cell size, the lower the resolution, and the overall information contents in the DEM will progressively decrease, and *vice versa* (Hengl 2006 and references therein).

In cartography the scale (level of abstraction) and resolution (level of detail) of spatial data are different strongly connected data. In general, coarser grid resolutions are connected with smaller scales and larger study areas, while finer grid resolutions are connected with larger scales and smaller study areas (Hengl and Evans 2009). From the relationship between scale and resolution results, it follows that there is not a unique definition of “high-resolution” DEM, because it depends also on the scale of observations. For example, a 10-meter DEM of the entire world can be considered as high resolution topographic data, but the same DEM used to analyse a lava channel, which consists in meter scale features, provides low resolution information. It is a fact that the expression “high-resolution” DEM has been spread with the advent of LiDAR technologies, which are able to produce a point cloud with density resolution of more than 0.5 points/m<sup>2</sup>.

Since the data produced by remote techniques are an (almost) irregular set  $S$  of 3D points  $p_i = (x_i, y_i, z_i)$ ,  $i = 1, \dots, n$ , constituted by million to billion points, it is necessary to interpolate  $S$  on a uniform grid of prescribed resolution. Interpolation techniques are based on the principles of spatial self-correlation, which assumes that closer points are more similar compared to farther ones. Interpolation in grid digital elevation modelling is used to estimate the terrain height value of a point (the node of the mesh) by using the known elevations of neighbouring points (Li et al., 2004). There are many interpolation methods for DEM generation, including deterministic methods such as inverse distance weight (IDW), Nearest Neighbor Interpolation (NN), and geostatistical methods such as Kriging. IDW calculates values to unknown points as weighted average of the values available at the surrounding known points. NN interpolation uses the value of the nearest point and does not consider the values of neighbouring points. Kriging utilizes a variogram that depends on the spatial distribution of data rather than on actual values.

Interpolation processes imply the definition of cell size. Selecting a suitable cell size for a point cloud of a given point density is not an easy task. In general, a finer DEM resolution means a more

accurate representation of topography and higher information content (Kuo et al., 1999), while a coarser DEM can be significantly different from the actual surface with some features that might disappear or be displaced (Fig. 1.1a and b). At the same time, if the cell size is too fine in relation to vertical accuracy, it might introduce local artefacts and slow down the computational processes (Fig. 1.1c). An optimum grid resolution must reflect the complexity of the features we want to represent, avoiding redundant information and artefacts.

Among the various methods, a suitable cell size can be selected for a point cloud of given point density ( $\rho$  in points/m<sup>2</sup>), considering the relation between cell size ( $w$ ) and variance of points, detrended for the mean slope ( $\sigma$ ), in the selected cell size. For a given point cloud the theoretical optimal cell size is  $w_o = \sqrt{1/\rho}$  (Fig. 1.1c). For example the ideal condition for a cloud with point density of 1 point/m<sup>2</sup> is to set a cell size of 1 m. However, the point cloud usually contains redundant information and therefore we can define a second optimal cell size derived from the same data with no redundant information  $w_o^* = \sqrt{1/\rho^*}$  (Fig. 1.1c).

For a cell size less than  $w_o$ , some cells could not be assigned an elevation value (Fig. 1.1a). In this case, the best solution to keep the final DEM at high resolution (this could be necessary if we want to compare different DEMs or because other portions of the same DEM have higher point density and we want to keep the grid regular), one should first generate a TIN and then convert the TIN into a regular grid (Fig. 1.1d). By increasing  $w$ , the number of points included in the cell size increase. We expect that  $\sigma$  will remain almost constant when  $z$  fluctuations are random; *vice versa*, when  $z$  variations are due to effective topographic changes,  $\sigma$  will increase (Fig. 1.1c and d). In other words, we expect  $\sigma$  to remain almost constant as long as  $w$  includes uncorrelated points or until  $w$  is equal to  $w_o^*$  (Fig. 1.1d).  $w_o^*$  cannot be calculated *a priori*, it follows that the graph of Fig. 1.1d should be produced to select the suitable cell size.

Since the topography imaged by the DEM is complex, in order to keep the grid regular, the selected cell size is usually as low as possible, even if the flat areas will be oversampled. The choice of the suitable cell size is made by the expert analyst taking into account the above discussion and also by visually inspecting the DEM. In case of topographic change detection analysis, the DEM resolution is also chosen taking into account the need to compare DEMs with the same resolution, regardless of the original data density.

DEMs contain the  $x$ ,  $y$  and  $z$  information of a modeled topographic surface. Three-dimensional processes such as lava flow are inherently dynamic. Remote sensing methods for 3D data production allow to image the investigated surface at different time steps quite easily and, consequently, the multi-temporal DEM comparison areas are often used for topographic change detection (e.g. Favalli et al., 2010a; Fornaciai et al., 2010a; Behncke et al., 2016; Richter et al., 2016). Recently, this possibility has been increased by the diffusion of the Structure from Motion

(SfM) photogrammetric methods that reduce the costs for producing DEM and offer relevant logistic advantages (e.g. Kolzemburg et al., 2016; Richter et al., 2016).

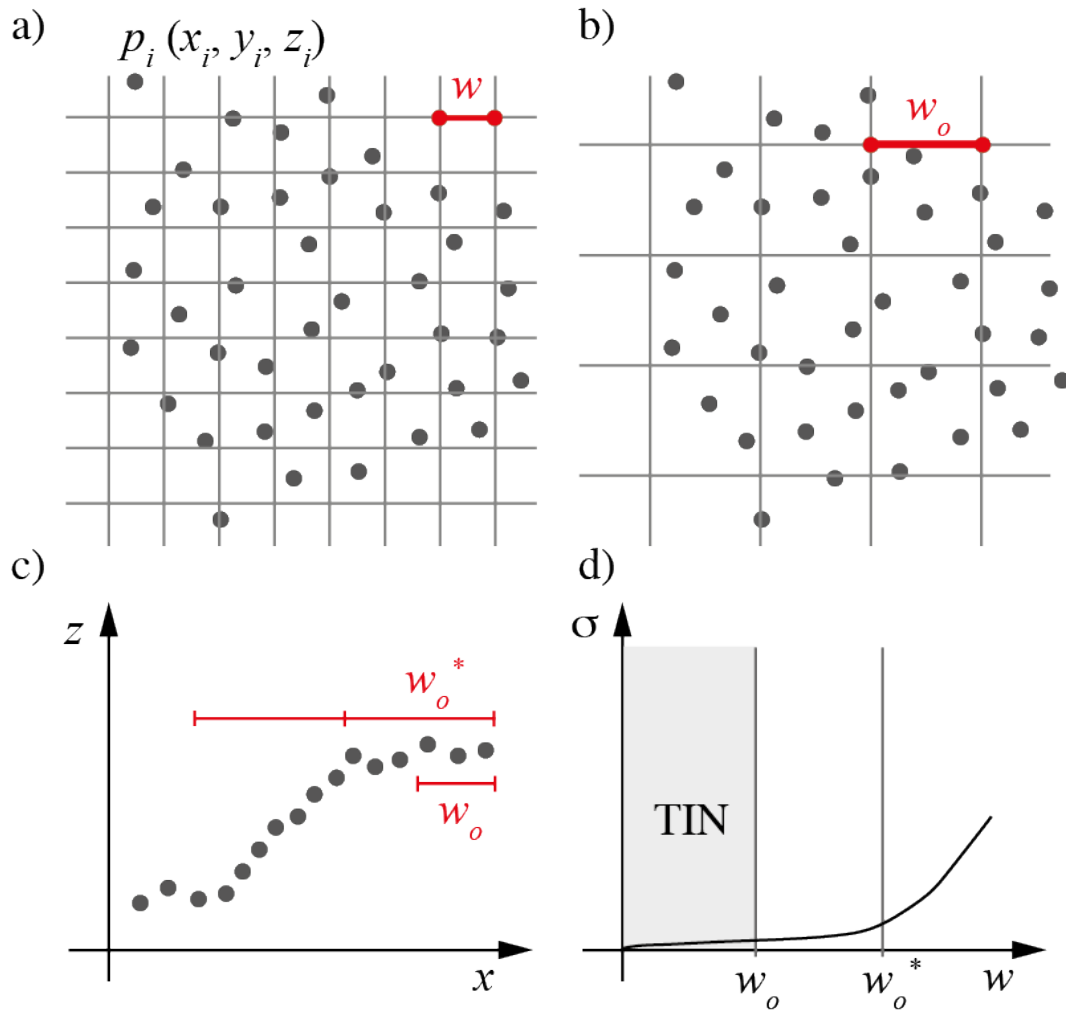


**Fig. 1.1** The suitable cell size for DEM interpolation. a) A cell size that is too small requires to interpolate data in some empty cells; b) with a proper cell size all cells have a value, calculated from the points inside the cell; c) Point cloud profile. The proper cell size can oversample the data point. The optimum cell size should take into account only the correlated informative contents such as the variation due to the real topographic changes; and d) The optimum cell size should be calculated considering the variation inside the cell.

Different DEMs of the same area derived from data collected at different times allow to introduce the fourth dimension of DEM: the temporal dimension ( $t$ ). Eitel et al., (2016) suggest distinguishing between multi-temporal ( $>1$  month return interval) and hyper-temporal ( $\leq 1$  month return interval) acquisitions.

## 1.2 Airborne Light Detection and Ranging (LiDAR) system

The past decade has seen a remarkable increase in the number of peer-reviewed papers on the morphometry of volcanic features (e.g. Fornaciai et al., 2012; Grosse et al., 2012; Cashman et al., 2013; Tarolli 2014; Favalli and Fornaciai 2017). This can be largely ascribed to the diffusion of airborne Light Detection and Ranging (LiDAR) technologies, which have significantly improved the quality and resolution of digital topographic data for large areas.

The Airborne LiDAR system consists of several integrated technologies to collect, during a flight, a dense cloud of points with known coordinates representing the 3D model of the imaged surface. Basically, an airborne LiDAR system implements a remote sensing component and a georeferencing component. The remote sensing component is the LiDAR itself and includes a Laser Ranging Unit (LRU), an Opto-Mechanical Scanning Device (OMSD), and a controlling and data-sampling unit. The georeferencing component is a position orientation system (POS), which includes a global positioning system (GPS) and an inertial measurement unit (IMU). The airborne platform, the LiDAR and the POS are the airborne segments. The Global Positioning System (GPS) reference stations and the processing hardware and software for off-flight data processing are the ground part of the system (Wehr 2009).

The LRU is basically composed by a transmitter and an optical receiver. The most direct ranging measurement consists in determining the time-of-flight of a light pulse; the traveling time  $t_L$  of a light pulse is  $t_L = 2R/c$ , where  $R$  is the distance between the ranging unit and the object surface;  $c$  is the speed of light (Fig. 1.2). The range resolution  $\Delta R$  is determined by the time resolution  $\Delta t_L$  of the traveling time measuring instrument and is given by  $\Delta R = c \Delta t_L / 2$ . The laser transmitter generates very short pulses with high peak power levels and high pulse repetition rates. The laser radiation is collimated by a lens that controls the beam divergence. The footprint diameter  $d$  is dependent on the ranging distance ( $R$ ) and on laser beam divergence ( $\omega$ ), which is itself a function of the size of the transmitting aperture ( $D$ ) and of the transmitted wavelength ( $\lambda$ ). Following Wehr (2009) a good approximation for footprint  $d$  is given by  $d = \omega R$ . At nadir,  $R$  equals the flying height  $H$ . All airborne laser scanners used in this work emit light in the near infrared at wavelengths of 1064 nm.

The OMSD deflects the transmitted beam across the flight line in order to obtain a surface coverage. The scanner must scan sufficiently fast to compensate for the forward velocity of the platform while achieving the desired sampling density in the flight path direction. In the LiDAR used in this work, the cross-track scanning of the ground is performed by oscillating plan mirrors. This results in a saw-tooth pattern of measured points over the ground (Favalli et al., 2009).

The control, monitoring and recording unit (CMRU) synchronizes the ranging unit with the scanner, triggering the pulsed laser synchronously with the incremental scanner steps. Additionally, this unit stores in the hard disk the ranging dataset, including the slant ranges of the return pulses, the return intensity if available, the instantaneous scanning angles and high precision time stamps. The time stamps, required for later synchronization with the POS data, derive from the GPS 1 pulse per second (pps) signal.

### 1.2.1 Airborne LiDAR data generation

During a survey, the LiDAR collects the line-of-sight slant ranges referencing the acquired data to its own coordinate system. These measurements are controlled and stored by the LiDAR control unit (LCU) (Fig. 1.2). At the same time, POS acquires the position and orientation of the system and the on-ground GPS stations collect data at known earth fixed positions for later off-line computing of differential GPS (DGPS) positions of the airborne platform. POS data are controlled and stored by the POS Computer System (PCS) (Fig. 1.2). LCU and PCS both work in their own time system and at the end of the survey they produce different files: the LCU outputs LiDAR raw data in a file stored with timestamps generated from the received GPS signal; the PCS outputs a file containing the instantaneous three-dimensional position and the orientation angles of the laser scanner as a function of the GPS time (GPS time |  $x_{WGS84}$ ,  $y_{WGS84}$ ,  $z_{WGS84}$  | roll, pitch and yaw).

The LCU and POS stored files are synchronized by using GPS time to obtain a file containing the following data: GPS time |  $x_{WGS84}$ ,  $y_{WGS84}$ ,  $z_{WGS84}$  | roll, pitch and yaw | slant range | intensity | scan angle. The coordinates are related to the LiDAR origin and the orientation angles are the rotations about the instantaneous local horizontal system.

Assuming a perfect inner orientation calibration, the LiDAR geocoded laser measurement points on the ground can be simply described by the vector approach (Fig. 1.2) (Wehr 2009):

$$\vec{G} = \vec{r}_L + \vec{s} \quad (1.1)$$

where  $\vec{G}$  is the vector from the earth centre to the ground point,  $\vec{r}_L$  is the vector from the earth centre to the LiDAR point of origin given by the POS, and  $\vec{s}$  is the slant ranging vector symbolizing the laser beam.  $\vec{s}$  is determined by the orientation of the LiDAR, measured by the POS in 3D space, and by the direction of the laser beam, defined by the instantaneous angular position of the laser beam deflection device in the scanner coordinate system.

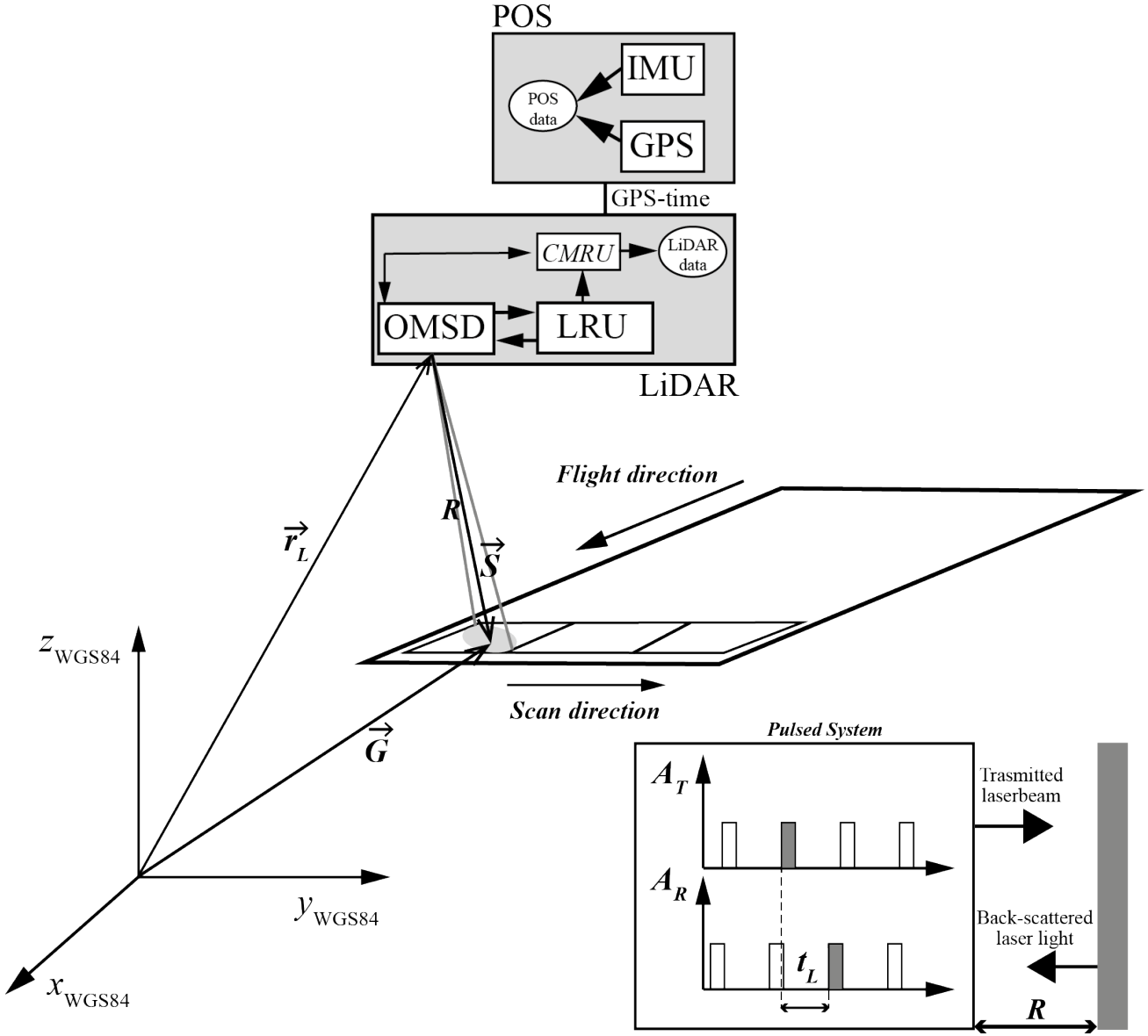


**Fig. 1.2** LiDAR system. The LIDAR component is formed by the laser ranging unit (LRU), an opto-mechanical scanning device (OMSD) and a controlling and data sampling unit (CMRU). The POS component is formed by a global positioning system (GPS) and an inertial measurement unit (IMU). POS and LiDAR are synchronized using the GPS time. In the pulsed system  $A_T$  is the amplitude of the transmitted signal and  $A_R$  is the amplitude of the received signal.  $t_L$  is the traveling time and  $R$  is the distance between the ranging unit and the object surface (Wehr 2009).

The LiDAR and POS do not have the same orientation, therefore a misalignment between POS and LiDAR must be taken into account, even considering that the accuracy of the georeferenced data strongly depends on the calibration data of the LiDAR and POS sensors. The misalignment is described by the bore sight misalignment angles in roll  $\delta\omega$ , pitch  $\delta\varphi$ , and yaw  $\delta\kappa$  between IMU and LiDAR, which are determined by a calibration process. The LiDAR data collected from the calibration areas is generally used to determine the misalignments. When a new set of calibration parameters is derived, the resulting improvement is checked and validated. The final output contains georeferenced laser measurement in chronological order (GPS time |  $x_{\text{laser\_WGS84}}$ ,  $y_{\text{laser\_WGS84}}$ ,  $z_{\text{laser\_WGS84}}$  | intensity).

The final product of a LiDAR survey is a high-density georeferenced 3D point cloud of the imaged surface that can be used to generate a high resolution DEM of the investigated surface (see Chapters 2, 3 and 4).

## 1.3 Structure from Motion (SfM) photogrammetry

### 1.3.1 Single, stereo and multi-view photogrammetry

Image-based 3D reconstruction photogrammetric technologies can be categorized into two broad groups: (traditional) stereo-photogrammetry and Structure-from-Motion (multiple image) photogrammetry.

The basic problem in analytical photogrammetry is that of mathematically relating the positions in a space of imaged objects to the position of their image points in the plane of image and *vice versa*. The most basic geometric concept utilized in developing solutions to this problem is the collinearity condition, according to which the perspective centre of the camera  $O (X_o, Y_o, Z_o)$ , the object point  $P (X_P, Y_P, Z_P)$  and its image  $p (x, y)$  on the photograph lie on the same line (Fig. 1.3). This concept is used to develop nonlinear collinearity equations, where the transformation of the object coordinates  $(X_P, Y_P, Z_P)$  into the corresponding image coordinates  $(x, y)$  is expressed as function of the position and orientation (pose) of the camera in the space of the object coordinate system, which is usually a geodetic coordinate system (exterior orientation); and of the position of the perspective centre of the sensor with respect to the image (interior camera orientation). Exterior orientation is defined by six parameters: the object space coordinates  $(X_o, Y_o, Z_o)$  of the perspective centre and the three orientation angles  $\omega, \varphi, \kappa$  of the image-space coordinate axes with respect to the object space system. These parameters allow the placement of the bundle of rays in the same place and orientation at the time of photogrammetric exposure. Interior orientation is defined by three parameters: the focal distance  $f$  and the coordinates of the principal point  $c (x_o, y_o)$ . They allow the reconstruction of the bundle of rays; by converging towards the perspective centre, the rays create the photographic image. The collinearity equations can be written as:

$$p(x, y) = F(X_o, Y_o, Z_o, \omega, \varphi, \kappa, x_o, y_o, f, X_P, Y_P, Z_P) \quad (1.2)$$

where the parameters  $x_o, y_o, f, X_P, Y_P, Z_P, X_o, Y_o, Z_o, \omega, \varphi, \kappa$ , are either unknown or known, depending on the particular photogrammetric problem.

Fig. 1.3 shows that a single image cannot provide any information about elevation. Point  $P$  can be placed along any position on the light ray  $OpP$  by using a single image. Two images of an object taken from different positions is the minimum condition necessary for a 3D object measurement. The object point coordinates  $P (X_P, Y_P, Z_P)$  can be determined from the intersection of the rays that join perspective centres and of the photographic images from (at least) two photographs with known interior and exterior orientation (Fig. 1.3). This procedure, called stereo-photogrammetry, uses a pair of stereo-images to form the stereo-model, and then to measure the 3D coordinates of the objects on the stereo-model. Fig. 1.3 shows the basic principles of stereo-photogrammetry:  $O$  and  $O'$  are the projection centres,  $p$  and  $p'$  are the two image points on the left and right images, respectively. The light rays from  $Op$  and  $O'p'$  intersect at point  $P (X_P, Y_P, Z_P)$ , which is on the stereo-model.

Traditional stereo-photogrammetry uses some known object space points (GCPs) and its image points on photographs to calculate exterior and interior parameters by applying the collinearity equations. It involves a first step for determining the corresponding point in both images (tie points), a second step in which the image-pair is oriented, and finally the 3D object measurement. The orientation of a stereo-pair provides the six exterior orientation parameters of both images. This process first calls for a relative orientation in which the translation and rotation of one image with respect to its stereo-partner is determined within a common local model coordinate system. Successively, absolute orientation, which consists of a spatial similarity transformation with three translations, three rotations and one scaling factor, describes the transformation of the local model coordinate system into the object coordinate system via reference points (Luhmann et al., 2014).

If multiple images of the same scene are acquired, each image generates a spatial bundle of rays, defined by the imaged points and the perspective centre (Fig. 1.4). When bundles of rays from multiple images are intersected, a dense network able to reconstruct the geometry of the acquiring system can be created. Considering 3D features  $P_j (X_{P_j}, Y_{P_j}, Z_{P_j}), j = 1 \dots n$ , imaged in  $i$  shots with camera pose and internal calibration parameters  $C_i, i = 1 \dots m$ , the collinearity equation can be expressed as:

$$p_{ij}(x_{ij}, y_{ij}) = F(C_i, P_j) \quad (1.3)$$

Without any further information, only the coordinates of corresponding points between images can be achieved. The number of unknowns can be calculated as follows (Luhmann et al., 2014):

$$u = u_e \cdot u_{images} + u_p \cdot u_{points} + u_c \cdot u_{cameras} \quad (1.4)$$

where  $u_e = 6$  parameters of exterior orientation per image,  $u_p = 3$  coordinates of new points and  $u_c = 0 \dots \geq 3$  parameters of interior orientation per camera. More generally, in addition to pose and to simple internal parameters, real cameras would require other parameters capable of modeling internal aberrations such as radial distortion. These aberrations should be corrected before the process and are not taken into account here. From Eq. 1.4 it results that there is a minimum number of photos that must be acquired to fix the geometry of the acquisition system starting only from the image points.

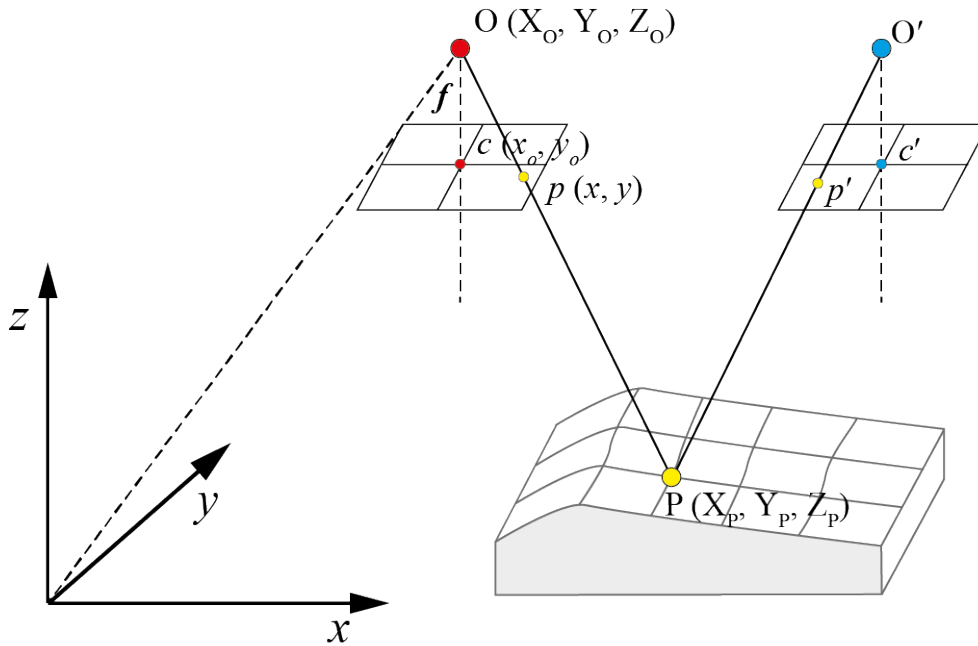


Fig. 1.3 The basic principles of stereo-photogrammetry

Where the configuration provides a suitable geometry, all the unknown parameters can be grouped into a simultaneous solution (with given or unknown interior orientation elements). The multi-image configuration can use the method of bundle adjustment for simultaneous camera orientation and for the calculation of the associated 3D object point location. Bundle<sup>3</sup> adjustment is a method employed for the simultaneous numerical fit of an unlimited number of spatially distributed images (ray bundles). The single process of simultaneously estimating the 3D geometry (or structure) of a scene and the different camera poses (i.e. motion) is called Structure from Motion (SfM) (Ullman 1979; Carrivick et al., 2016).

### 1.3.2 Structure from Motion methods

In the past few years, advances in computer vision have led to the development of Structure from Motion (SfM) technology, which has significantly simplified image-based 3D topographic surface

<sup>3</sup> The name “bundle” refers to “bundles” of light rays connecting the camera centers to 3D points, and “adjustment” to the minimisation of the re-projection error (Szeliski 2011).

reconstruction (e.g. Favalli et al., [under review](#)). The SfM method takes multi-view stereo images as input and uses advanced image feature detection, matching techniques and a highly redundant bundle adjustment procedure to yield a 3D point cloud and camera orientations/poses in a common arbitrary 3D model coordinate system. The point cloud generated from the SfM method is usually refined at a much finer resolution by using the Multi-View Stereo (MVS) method. Although the term SfM-MVS workflow would be more appropriate, it is common practice to refer to the system as SfM only. 3D point cloud can be then appropriately scaled and oriented in a global coordinate reference system by applying a simple 3D similarity transformation (Westoby et al., [2012](#)).

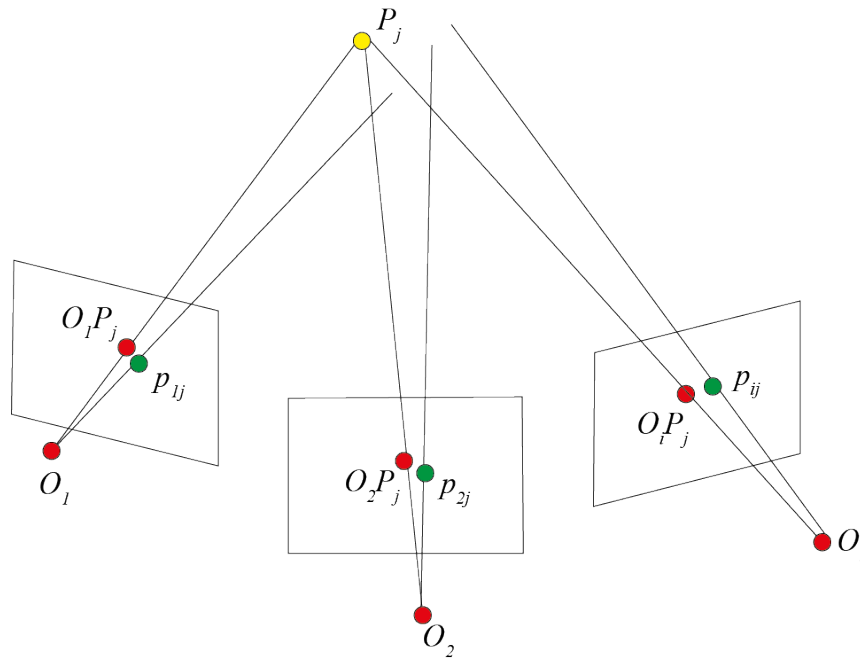


**Fig. 1.4** Bundle adjustment in multi-view photogrammetry.

The general workflow required to reconstruct the 3D scene geometry by the SfM method from a set of images with unknown interior and exterior orientation is described in detailed in Kolzenburg et al., ([2016](#)). The main steps are described below:

1. Feature detection and matching. The Features detection algorithm solves the problem of correct identification of the same features over a large image dataset, regardless of the changes in orientation, scale, illumination or 3D position. Among others, the scale-invariant feature transform (SIFT) object recognition system (Lowe [2004](#)) is the most widely used.
2. Structure from Motion method. Structure from Motion method uses the set of corresponding points between images to estimate simultaneously the 3D scene structure, the camera pose and the internal camera calibration parameters. The position of 3D features  $P_j$  on image ( $p_{ij}$ ) can be predicted by [Eq. 1.3](#). Given the uncertainties in the determination of  $p_{ij}$  (due to the random noise or to some systematic errors) there are some discrepancies between the true

image of feature  $P_j$  in image  $i$  and  $p_{ij}$  (Fig. 1.4). Structure from Motion deals with the problem of taking these measurements and jointly solving for the camera and scene parameters that predict these measurements as better as possible. This problem is usually posed as an optimization over the collective set of camera and scene parameters  $C = (C_1, C_2, \dots, C_n)$  and  $P = (P_1, P_2, \dots, P_m)$ , where function ( $E$ ) measures the discrepancy between the measured 2D point positions and those predicted by Eq. 1.3. Function  $E$  is the sum of squared projection errors:

$$E(C, P) = \sum_{j=1}^m \sum_{i=1}^n D(p_{ij}, O_i P_j)^2 \quad (1.5)$$

$E$  is minimized by using the non-linear least squares optimization bundle adjustment. Since bundle adjustment is an iterative process, unable to guarantee convergence to the optimal solution from an arbitrary starting point, an easily computable non-optimal solution and initial parameter values before the non-linear optimization are required. The scene reconstruction generally starts with a single pair of images, which should have a large number of corresponding points and guarantee a markedly different perspective for a robust reconstruction. Once the parameters have been estimated and as well as an initial set of 3D points, a two-frame bundle adjustment is performed to minimize the re-projection error between the initial pair. Then, another camera (or multiple camera) is introduced into the optimization process. For each new single view that is added, the camera position is first initialized and then further bundler adjustment is run (Snavely 2008; Luhmann et al., 2014). A global bundle adjustment is finally performed over all the cameras to refine the entire model (Szeliski 2011).

4. Multi-View Stereo (MVS) matching. SfM processes produce a 3D sparse point cloud and reconstruct camera poses. In order to obtain a more detailed high-quality surface reconstruction, the model is densified through a process known as the Multi-View Stereo (MVS) method. MVS provides a complete 3D scene reconstruction from a collection of images, the interior and exterior camera parameters of which have been previously determined by the SfM method. Compared with a sparse point cloud generated by SfM, a dense point cloud generated by MVS shows an increase in the point density of at least two orders of magnitude.
5. Scale and Georeferencing. SfM provides a 3D model in an arbitrary coordinate system. Absolute distances between cameras or between reconstructed points can never be recovered from images alone, regardless of how many cameras or points are used (Szeliski 2011).

Georeferencing and scaling of the point cloud require a minimum of three GCPs with XYZ coordinates or seven parameters for linear similarity transformation, which comprises three translation parameters, three rotation parameters and one scaling parameter (Carrivik et al., 2016).

The final product of the SfM method is a high-density georeferenced 3D point cloud of the imaged surface, which can be used to generate a high resolution DEM (see Chapter 5).

## **1.4 Research goal and structure of the thesis**

There are more than 1500 active volcanoes on our planet, with millions of people living on an active edifice. This means that about one person in ten is at risk from effusive volcanic eruptions. In Europe, especially in Italy (e.g., Mount Etna, Vesuvius and Stromboli), as well as in Europe's overseas territories (e.g., Île de La Réunion, France, Azores, Portugal, Canary Islands, Spain), effusive eruptions constitute a serious threat to infrastructure and property. Because lava flows advance slowly, they are unlikely to cause human fatalities. However, inundation by lava will cause total destruction of any fixed objects, including urban infrastructure, communications and industry. This was illustrated by the Nyiragongo 2002 eruption, which buried a major part of the city of Goma and its airport under lava, causing displacement of the population, civil disorder and deaths (due to an explosion at a petrol station).

Lava flows consist of an unconfined multiphase and multicomponent stream whose temperature, rheology, and emission rate all vary with time and space. The lava flow and emplacement dynamics are largely studied and debated because they have tremendous implications in terms of hazard and risk assessment. The natural complexity of these gravitational flows comes from the wide range of parameters involved in their advancement such as volume, emission rate, temperature, rheology of the fluid, composition, topographic constraints as well as the way in which these parameters vary and interact with each other in time and space during the flow.

Essential for studying the lava flow and emplacement dynamics is the data provided by a detailed morphometric analysis, including area, thickness and volume of the flow, spatial thickness variations, shape of the flow, geometry of the channel-fed lava flow. These data can be quantitatively compared to the results of experimental and numerical modeling of the lava flow, and can thus provide a means for building and testing hypotheses on the mechanisms at work during emplacement.

The aims of this thesis are: i) to provide high resolution measurements, with unprecedented details, of the topographic changes occurred on Mount Etna during the effusive activity between 2004 and 2010, using high-resolution multi-temporal LiDAR DEMs; ii) to provide high resolution morphometric data of eleven selected channel-fed lava flows during the 2006 and 2008-09 Etna eruption, using high-resolution, multi-temporal LiDAR DEMs; iii) to compare the effectiveness, in terms of lava flow morphometric analysis, of proven high-cost technologies for generating high-resolution DEMs, i.e. LiDAR, with low-cost emerging methods like the Structure from Motion method.

After introductory Chapter 1 where we provided a general overview of the methods and technologies used in this work, this thesis includes another four chapters and the conclusions.

In Chapter 2, the high resolution LiDAR-derived DEM of Mount Etna acquired during five different surveys conducted in September 2004, September 2005, November 2006, June 2007 and September 2010 was used to calculate with unprecedented details the volume, area and thickness of the lava emitted by Mount Etna during the 2004 eruption, the 2006 eruption and the activity from 2007 to 2010. The LiDAR data acquired in September 2004 and September 2005 over the summit area and the eastern flank of Mount Etna are compared so as to precisely map the 2004 lava flow areal extent and to measure with unprecedented accuracy the 2004 lava volume and thickness. Volume estimation also allows to constrain the mean output rate of this eruption. The LiDAR data acquired in September 2005 and June 2007 over the summit area and the eastern flank of Etna are compared to quantify with great precision the 2006 lava flow areal extent, thickness and volume as well as the mean output rate of the 2006 eruption. In addition, the LiDAR data obtained while the eruption was underway (November 2006) was also compared with pre- and post-emplacment for an analysis of the dynamics of the advancing lava flow. The LiDAR data achieved in September 2010 over the summit area and the eastern flank of Etna and the LiDAR data of 2007 of the same area, which integrated the results with volumes of eruptive products based on field/aerial surveys, were used to obtain more precise volumes for the September 2007 to May 2008 summit activity and the 2008-2009 flank eruption.

In Chapter 3, we review a number of analytical procedures used to parameterize and represent DEMs, in order to find crucial parameters for accurately mapping the surface-specific features of channel-fed lava flows, i.e. flow base, levees and channel bed. Firstly, we introduce some well-known parameters, such as hill-shaded maps, slope and aspect maps, curvature maps, roughness maps, and then we extend the review to some less common parameters such as Sky View Factor (SVF) maps, openness maps, Red Relief Image Maps (RRIM). As a test case, we use a 1200×1200 m LiDAR-derived DEM matrix acquired over the Valle del Bove valley on Mt. Etna during the June 2007 airborne survey with spatial resolution of 1 m. The test area is characterized by the presence of several lava channels variously superimposed. Since many of the surface parameters

reviewed have the same informative content, these parameters are cross-compared to infer which of them are most uncorrelated. The results are represented as a correlation matrix that can be employed to discard redundant maps. The highly uncorrelated parameters are used to carry out a morphometric analysis of a portion of 10-m resolution DEM of a phonolitic lava flow on Tenerife Island.

In Chapter 4 we use the high-resolution LiDAR-DEMs of Mount Etna to extract a large number of very accurate morphometric parameters from eleven channel-fed lava flows emplaced during the 2006 and 2008-09 Etna eruptions. Morphometric analysis takes advantage of the actual high-resolution topography above which the lava flows, builds its shape and emplaces. Here, for the first time, we are providing large amounts of data about pre-emplacment slope without interpolating the pre-existing topography under the flow. The morphometric analysis of selected lava flows is conducted through a semi-automatic procedure that measures the parameters over DEMs and that implies the tracking of surface-specific elements such as flow axes and base, levee ridges and edges of the channel bed. Tracking is supported by the automatic detection of surface-specific points and is performed over the SVF and openness down maps for a most effective DEM visualization. The morphometric parameters extracted include pre-emplacment slope, widths of flow, channel and channel base, as well as levee thickness and slope. Finally, these parameters are plotted together to investigate their mutual relationship.

In Chapter 5 we present the application of the UAV-SfM method to generate a high-resolution DEM and orthomosaics of the 1974 Mount Etna lava field. SfM-photogrammetry applied to these images enabled the extraction of very high-resolution (20 cm) DEMs and 3 cm orthomosaics for a total area of 1.35 km<sup>2</sup>. Data produced by the UAV-SfM were compared with airborne LiDAR data. In chapter 5 we show that SfM and UAV platforms can be effectively exploited to map volcanic features producing topographic data that cannot be obtained by the 1-m LiDAR-derived DEM.

While doing research for this thesis, some papers were submitted or published in peer-review journals. A summary of publications in relation to this thesis are presented below.

Karátson D., Yepes J., Favalli M., Rodríguez-Peces M. J. and Fornaciai A. (2016). Reconstructing eroded paleovolcanoes on Gran Canaria, Canary Islands, using advanced geomorphometry. *Geomorphology* 253, 123-134.

Behncke B., Fornaciai A., Neri M., Favalli M., Ganci G. and Mazzarini, F. (2016). Lidar surveys reveal eruptive volumes and rates at Etna, 2007–2010. *Geophysical Research Letters* 43(9), 4270-4278.

Kolzenburg S., Favalli M., Fornaciai A., Isola I., Harris A.J.L., Nannipieri L. and Giordano D. (2016). Rapid Updating and Improvement of Airborne LIDAR DEMs Through Ground-Based

SfM 3-D Modeling of Volcanic Features. *IEEE Transactions on Geoscience and Remote Sensing* 54(11), 6687-6699.

Richter N., Favalli M., Zeeuw-van Dalssen E. D., Fornaciai A., Silva Fernandes R.M.D., Pérez N. M., Levy J., Silva Victória S. and Walter T. R. (2016). Lava flow hazard at Fogo Volcano, Cabo Verde, before and after the 2014–2015 eruption. *Natural Hazards and Earth System Sciences* 16(8), 1925-1951.

Favalli M. and Fornaciai A. (2017). Visualization and comparison of DEM-derived parameters. Application to volcanic areas. *Accepted to Geomorphology*

Favalli M., Fornaciai A., Nannipieri L., Harris A., Calvari S. and Lormand C., UAV-based remote sensing surveys of lava flow fields: Very-high-spatial resolution methodologies for morphological modelling. *Submitted to Bulletin of Volcanology*.

---

## Chapter 2

---

### **Detection of topographic changes and quantification of eruptive products on Mount Etna (Sicily, Italy) by multi-temporal LiDAR acquisitions**

Volcanic activity causes rapid and dramatic changes to the Earth's surface. Large amounts of material are continuously added and removed from an active volcanic edifice in a complicated constructive and destructive sequence of effusive eruptions and explosive events. Accurate quantification analysis of topographic changes related to effusive activity allows crucial inferring parameters (e.g., area, thickness and volume of lava flow, and mean magma discharge rate) to produce lava flow hazard maps and to improve the existing lava flow models (Cashman et al., 2013). The detection of topographic changes measured by differentiating pre-, sin-, and post-eruptive high-resolution DEMs is nowadays considered the most suitable method to accurately quantify the volume of material emplaced or removed during an eruption (Cashman et al., 2013; Behncke et al., 2016; Richter et al., 2016; Bagnardi et al., 2016).

Mount Etna is an open-vent basaltic stratovolcano located along the Ionian coast of eastern Sicily (Fig. 2.1). It is the largest volcano in Europe and one of the most active on the Earth's surface. The activity mainly consists of effusive and explosive eruptions from either its summit craters or new vents opened on the flanks along the NE and S rift zones (Branca and Del Carlo 2004). The frequent occurrence of flank eruptions joined with the intense urbanization of its flanks exposes the Mount Etna flanks to high (mainly economic) volcanic risk. Over time, the volcano has fed long-lasting effusive eruptions and short-lasting, more powerful explosive episodes often associated with small lava flows (Branca and Del Carlo 2004; Andronico and Lodato 2005). As Mount Etna is characterized by an intense effusive activity, recent lava flows often cover the

previous volcanic products. This makes it difficult to accurately reconstruct and quantify its evolution. For this reason it is crucial to acquire topographic data with proper accuracy and extension as often as possible.

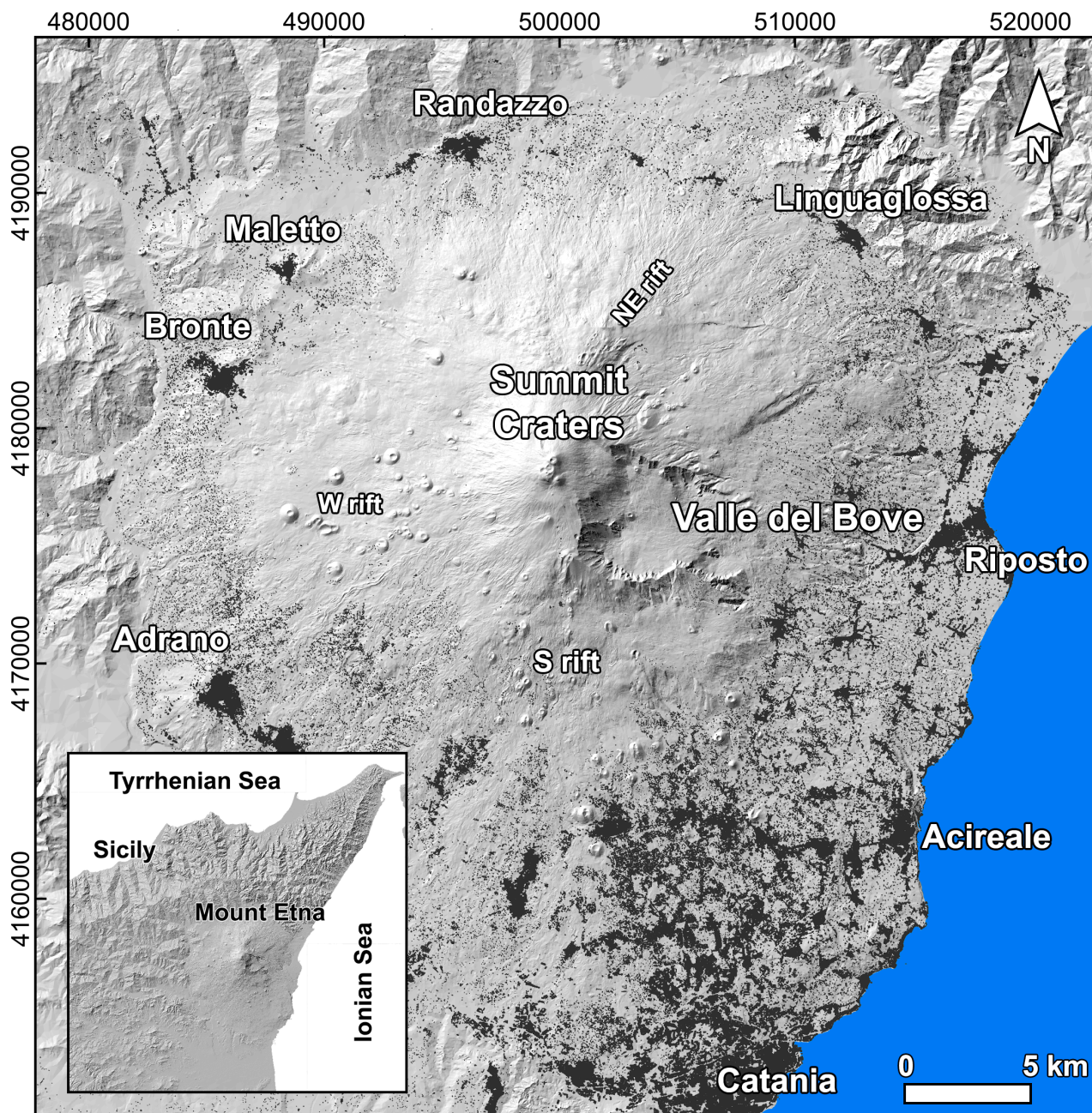


**Fig. 2.1** Hillshaded map of Mt. Etna derived from TINITALY DEM (Tarquini et al., 2012b). The populated areas are in black. Inset: map of NE Sicily showing the location of Mount Etna.

In this chapter, we quantify the Mount Etna topographic changes and the volume of eruptive products related to the volcanic activity between September 2004 and September 2010 by multi-temporal high-resolution LiDAR-derived DEMs. After the 2001 and 2002-2003 eruptions, which produced lava flows and an explosive activity of variable intensity (e.g. Acocella and Neri 2003), between 2004 and 2006 Mount Etna was predominantly involved in effusive eruptions (Burton et

al., 2005; Andronico et al., 2009). In 2007, episodic explosive activity and lava fountains were observed (Andronico et al., 2008), with the latter preceding the start of the 2008-2009 effusive eruption (e.g. Bonaccorso et al., 2011a; Behncke et al., 2016).

## 2.1 High-resolution LiDAR dataset of Mount Etna

LiDAR data used in this work were acquired during five different surveys (Table 2.1) conducted on 16 September 2004, 29-30 September 2005 (Figs 2.2 a and b), 17-18 November 2006 (Figs 2.3), 20-21 June 2007 and 17 September 2010 (Figs 2.4 a and b). These data are available at the Istituto Nazionale di Geofisica e Vulcanologia, Pisa Department. Although they have different extension and coverage, all surveys were planned to acquire the summit and eastern flank of the volcano (i.e., the areas most affected by topographic changes related to the volcanic activity), which were, consequently, imaged at different time intervals.

Date	Sensor	Coverage (m <sup>2</sup> )	N° of points	N° of strips	Pts/ m <sup>2</sup>	Res. (m)	Δz (m)	Δxy (m)
16/09/2004	ALTM 3033	249,072,690	104,037,769	20	0.42	1	0.16	0.55
29-30/09/2005	ALTM 3033	632,567,000	257,470,597	34	0.41	1	0.16	0.48
17-18/11/2006	ALTM 3033	42,504,530	124,319,482	53	2.92	1	0.10	0.71
20-21/06/2007	ALTM Gemini	459,882,349	231,153,619	38	0.50	1	0.09	0.60
22/07/-17/09/2010	ALTM Gemini	176,001,800	90,619,279	26	0.51	1	0.09	0.50
17/09/2010	ALTM Gemini	76,655,271	41,418,830	15	0.54	1	0.09	0.33

**Table 2.1** The Mount Etna LiDAR data base of INGV - Pisa. Pts. = points; Res. = resolution.

The 2004, 2005 and 2006 LiDAR datasets were acquired by an Optech ALTM 3033 sensor, the 2007 and 2010 data sets using an Optech Gemini sensor (for the characteristics of the ALTM 3033 and Gemini sensors see Favalli et al., 2009). The latter guarantee a better performance in terms of point density and accuracy, especially over poor reflective surfaces, like those covered by the volcanic products (Favalli et al., 2009; Fornaciai et al., 2010b).

The 2004 and 2005 LiDAR data were previously corrected for systematic errors, resulting in planimetric and vertical RMS errors of 0.55 and 0.16 m for the 2004 data and of 0.48 and 0.16 m for the 2005 data (Favalli et al., 2009). The point density of both LiDAR clouds was largely heterogenous and wide portions of the southern sector of Valle del Bove (VdB) had no data points (Fig. 2.2). The mean point density of the 2004 data was 0.42 points/m<sup>2</sup> and that of 2005 was 0.41 points/m<sup>2</sup>. A DEM with a resolution of 1 m was created from both LiDAR data sets.

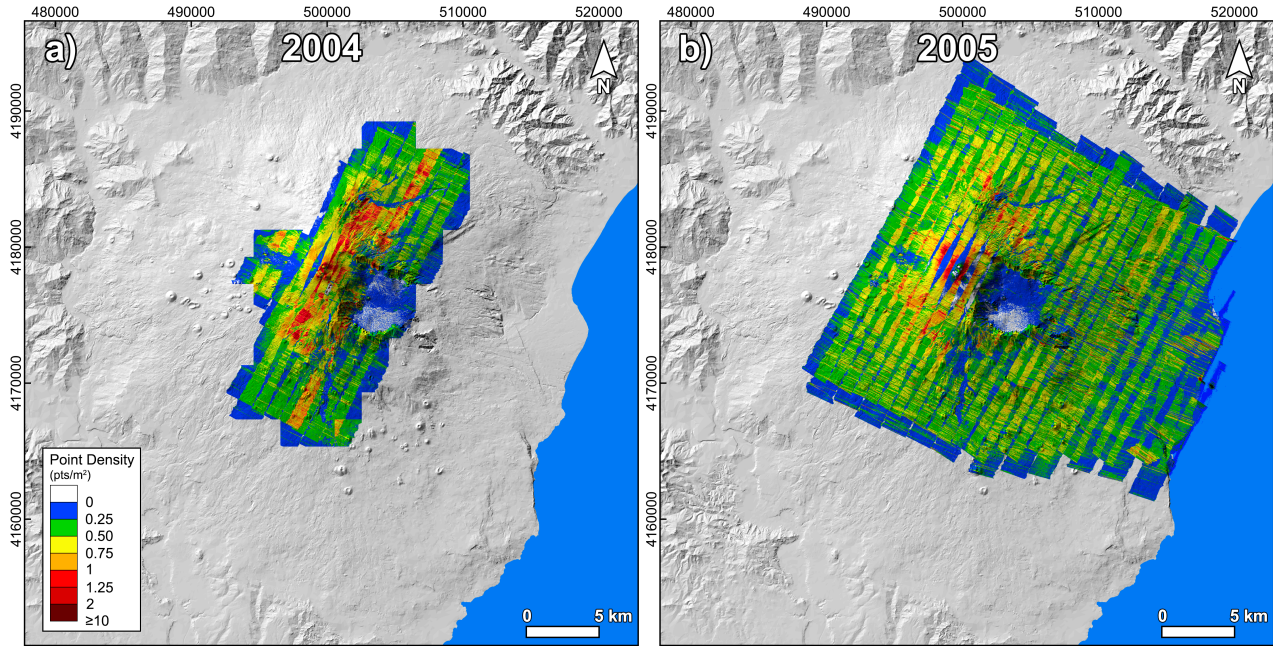


**Fig. 2.2** LiDAR data acquired during the 2004 and 2005 campaigns over Mount Etna. a) 2004 LiDAR point density map; and b) 2005 LiDAR point density map. The point density maps also show the extension of the surveys. The legend of frame b) is the same as that of frame a).

The 2006 LiDAR survey was specifically designed to obtain several strips of data of the same active flow at different times of the 2006 eruption (Favalli et al., 2010a). This resulted in an extremely dense point cloud with an average point density of  $\sim 2.92$  points/m<sup>2</sup> (Fig. 2.3). The planimetric and vertical RMS errors, calculated by following the procedure described in Favalli et al., (2009), were 0.71 and 0.10 m respectively. Given that the RMS error in  $z$  was reasonably low and owing to the particular features of this survey, no further corrections were applied to these data. To make these data comparable with those of the other LiDAR DEMs, we generated a DEM with a resolution of 1 m from the 2006 data.

The 2007 LiDAR data were previously corrected for the systematic errors, and resulted in planimetric and vertical RMS errors of 0.60 and 0.09 m respectively (Favalli et al. 2009). The point density of the 2007 data was more homogeneous than that of the data acquired with ALTM 3033. The average point density of 2007 data was  $\sim 0.50$  point/m<sup>2</sup> (Fig. 2.4a).

The 2010 LiDAR data were analysed in this thesis for systematic errors occurred by following the same procedure described in Favalli et al., (2009), which can be summarized in the following key steps: i) planimetric and altimetric discrepancies between overlapping strips were assessed at a number of chosen computational tie points; ii) at each tie point a local surface was constructed for each strip containing that point; iii) the displacements between different strips were calculated at each tie point; iv) major systematic errors were detected.

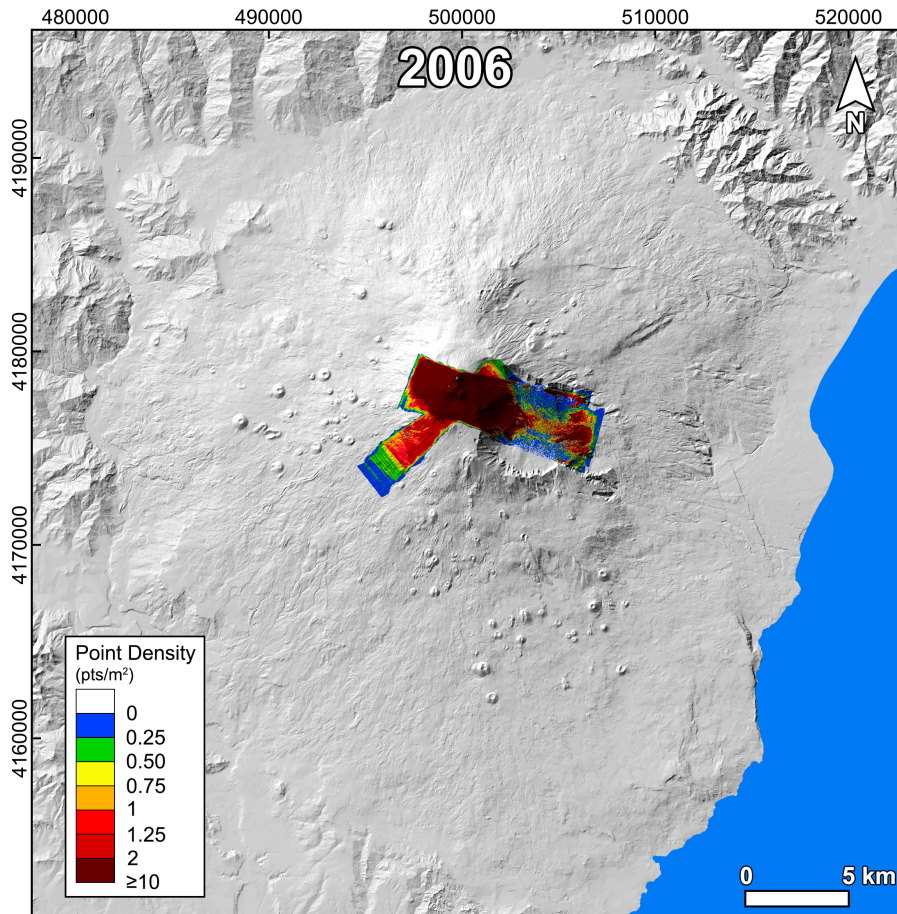


**Fig. 2.3.** LiDAR data acquired during the 2006 campaigns on Mount Etna.

The calculated planimetric and altimetric RMS errors of the 2010 LiDAR data were 0.33 and 0.09 m respectively. As shown by Favalli et al., (2009) for the 2007 LiDAR data, the correction of data with low starting RMS error was practically useless, considering the human and computational resources required for data correction. On account of the very low RMS error of the 2010 dataset (the lowest ever for the Mount Etna LiDAR INGV dataset, see Favalli et al., 2009), no further correction was made of the 2010 data. The average point density in the investigated area was 0.55 points/m<sup>2</sup>, yielding a sampling rate of ~1.35 m. For the same reasons stated above, we created a 2010 DEM with a grid step of 1 m.

All the LiDAR data imaging the summit and the eastern flank of the volcano presented large areas of superposition, widely interested by the volcanic activity between one acquisition and the following (Fig. 2.5). This made it possible to detect with unprecedented accuracy the topographic changes and to quantify the area, thickness and volume added or removed in those areas between two following acquisitions.

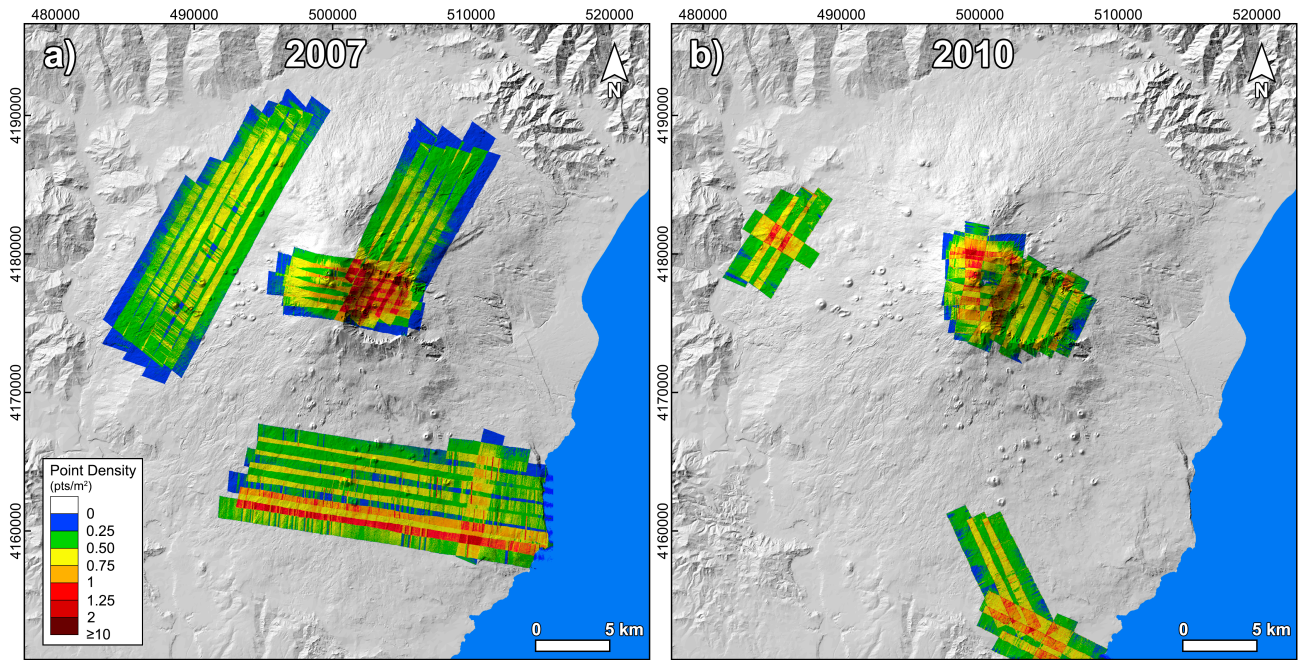


**Fig. 2.4** LiDAR data acquired during the 2007 and 2010 campaigns on Mount Etna. a) 2007 LiDAR point density map; and b) 2010 LiDAR point density map. The point density maps also show the extension of the surveys. The legend of frame b) is the same as that of frame a).

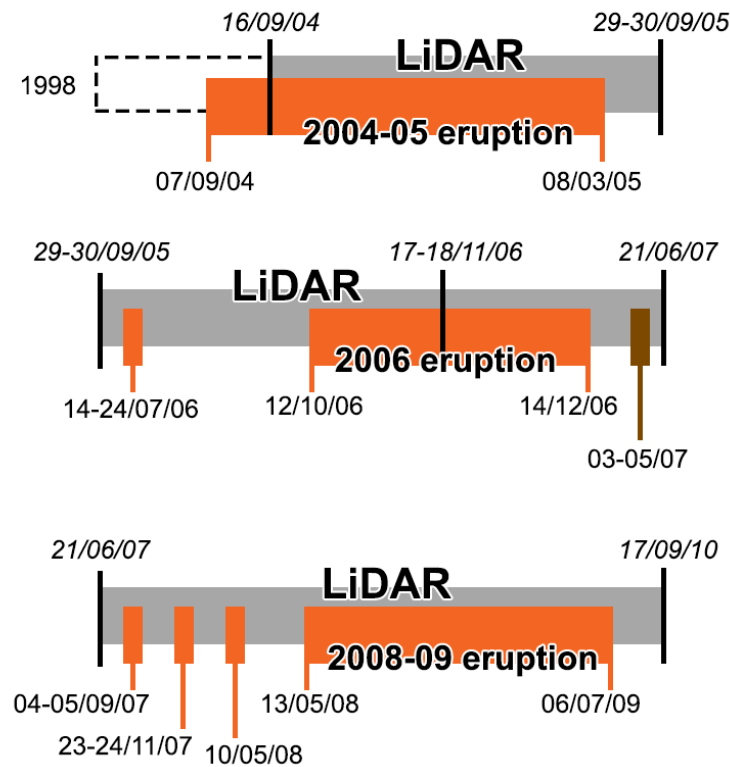


**Fig. 2.5** Sketch representing the main Mount Etna activity phases between two successive LiDAR surveys. The LiDAR acquisitions are reported in italics. 1998 refers to the TINITALY DEM (Tarquini et al., 2012). The 2006 LiDAR acquisition was performed while the eruption was ongoing. Time is not in scale.

## 2.2 Volume calculation from multi-temporal LiDAR-derived DEMs

The pre- and post-eruption LiDAR-derived DEM comparison allows to quantify the topographic changes due to the emplacement of lava flows and pyroclastic deposits in the survey area. Volume change calculations using multi-temporal DEMs are often affected by errors depending on mismatches in  $x$ ,  $y$  and  $z$  between the same areas imaged by the different acquisitions. If necessary, this error can be detected and reduced by measuring and minimizing the DEM differences in areas where the two DEMs are supposed to be equal, i.e. those areas not affected by natural changes.

Systematic errors (artefact  $\Delta z$ , hereafter  $\Delta z_{\text{error}}$ ) can be calculated by subtracting two grids and the results should be visualized in a map, in order to detect the distribution of errors outside the area affected by real changes. If systematic errors are present, we select several representative zones of the error distributions and calculate their mean  $\Delta z_{\text{error}}$  all around the area affected by volcanic activity. An interpolated function representing the mean  $\Delta z_{\text{error}}$  is then reconstructed as TIN, starting from a set of points with coordinates  $x$ ,  $y$  and mean  $\Delta z_{\text{error}}$ . The interpolated function is finally subtracted from the difference between the pre- and post-eruption LiDAR-derived DEMs.

Volume ( $V$ ) emplaced between two acquisitions was calculated from the DEM difference adjusted for the mean  $\Delta z_{\text{error}}$  according to the following equation (see Favalli et al., 2010a):

$$V = \sum_i \Delta x^2 \Delta z_i \quad (2.1)$$

in which  $x$  is the grid step and  $z_i$  is the height variation within grid cell  $i$ , that is, height difference experienced by the grid cell at location  $i$ . These values are then summed up for all the cells in the area in which we want to calculate volume changes.

As reported by Favalli et al., (2010a), generically the error on the volume is linearly dependent on the standard deviation of the height variations ( $\sigma_{\Delta z}$ ). This was calculated from regions where the surface did not change (i.e., control region), located around the investigated area ( $A$ ) and different from the areas used to minimize the DEM discrepancies. Even if the errors of nearby pixels are somewhat correlated in DEMs, they usually become uncorrelated over a certain length scale error. Consequently, such errors are neither fully correlated nor entirely uncorrelated for extended regions (Favalli et al., 2010a). In this work, we assumed the worst possible scenario considering that the errors were completely correlated. Therefore, in agreement with Favalli et al., (2010a), we used the following equation:

$$\text{Err}_{V,\text{high}} = A\sigma_{\Delta z} \quad (2.2)$$

The volume errors, calculated using equation (2.1), were then reasonably overestimated. The areas across which we measured the volume changes were identified and outlined directly on the map of differences obtained by comparing the DEMs.

## **2.3 Mount Etna eruptive activity from 2004 to 2010**

### **2.3.1 2004-05 Mount Etna eruption**

At the time of the 2004 acquisition, Mount Etna was interested by the 2004-05 flank eruption (Figs. 2.5 and 2.6), which had started 9 days before the survey, while at the time of the 2005 acquisition the eruption had ended ~7 months before (Fig. 2.5); it is worth noting that no significant eruptive episode occurred between the end of the eruption and the 2005 survey. The point density of the 2004 and 2005 LiDAR clouds was largely dishomogeneous and wide portions of the southern sector of Valle del Bove (VdB), partially buried by the 2004-05 lava flow, had no data points (see Figs. 2.7 a and b).

The 2004-05 eruption marked the resumption of flank activity at Mount Etna after the 2002-03 eruption (Andronico et al., 2005). It lasted six months, from 7 September 2004 to 8 March 2005, and was characterised by prolonged lava effusion slowly supplied by a fissure system developing downward from the South-East Crater (SEC; Fig. 2.6). The eruptive activity produced a voluminous and compound lava flow field, which filled and significantly modified the morphology of the upper part of the Valle del Bove (VdB) depression in the eastern flank of the volcano (Fig. 2.6).

The 2004-05 activity was characterised by an unusual onset if compared with previous effusive eruptions of Etna. No significant volcanic precursors in the hours immediately before the onset were recorded (Burton et al., 2005). This suggested that the beginning of the eruption consisted of only passive drainage of residual and relatively degassed magma already resident within the SEC conduit, rather than of the arrival of a new volatile-rich batch of magma (Burton et al., 2005; Corsaro and Miraglia 2005).

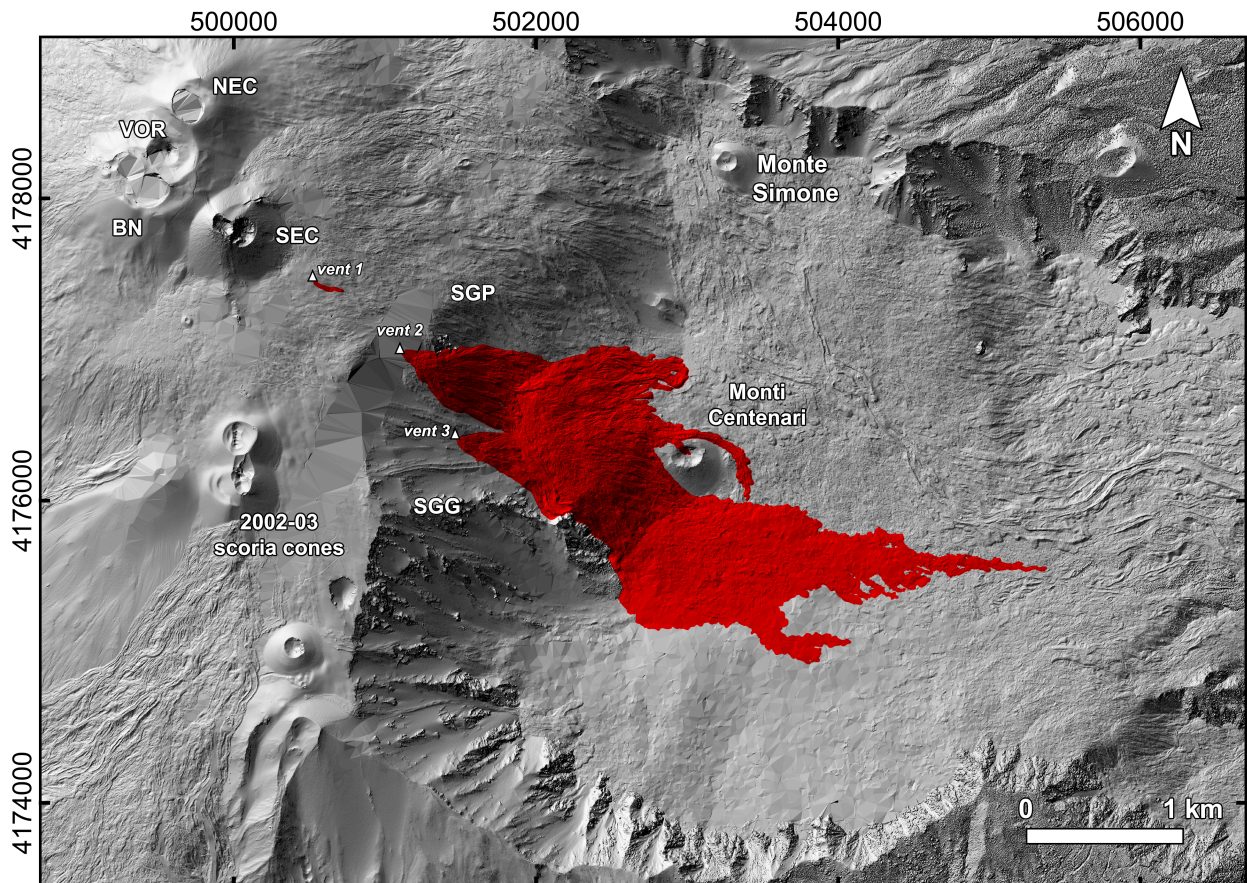


**Fig. 2.6** The 2004-05 lava flow field. NEC = North-East Crater; VOR = Voragine, BN = Bocca Nuova, SEC = South-East Crater (SEC), SGP = Serra Giannicola Piccola, SGG = Serra Giannicola Grande.

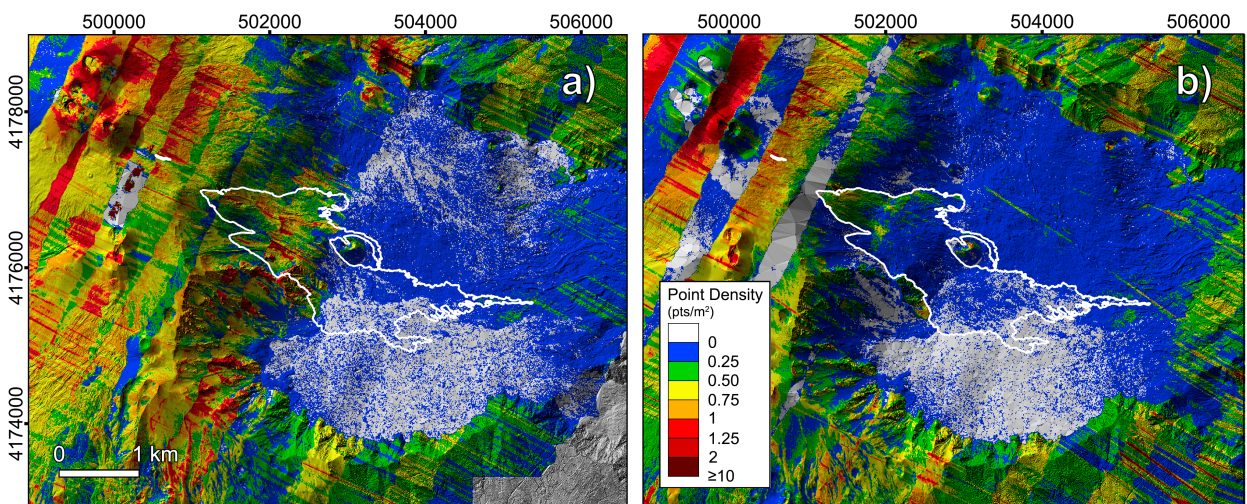


**Fig. 2.7** LiDAR point density map focused on the area involved in the 2004-05 lava field (white line). Frame a) refers to the 2004 acquisition and frame b) to the 2005 acquisition. The legend is the same for both frames. The distal portions of the lava flow field have very low point density in both LiDAR data.

### 2.3.2 2006 Mount Etna eruption

Between the 2005 and 2007 LiDAR Mount Etna surveys, the volcano was involved in the 2006 eruption (Fig. 2.8). Three different LIDAR datasets are available for this eruption: the first (pre-

eruption) of September 2005 (Favalli et al., 2009), the second (syn-eruption) of November 2006 (Favalli et al., 2010a; Favalli et al., 2011), and the third (post-eruption) of June 2007 (Favalli et al., 2011; Behncke et al., 2016). The point densities of the 2005, 2006 and 2007 LiDAR clouds were very different (Fig. 2.9), a cell size of 1 m was used for all those datasets in order to make the DEMs comparable. These differences were related to the different altimeters used (Table 2.1) and to the particular features of the 2006 survey already described.

Resumption of the Mount Etna activity occurred sixteen months after the end of the 2004-05 flank eruption and continued intermittently for five months (Behncke et al., 2008). The activity resumed on 14 July when a short fissure opened on the lower ESE flank of the SEC cone, releasing a lava flow that travelled 3.5 km eastward in the following 10 days. This phase culminated on 20 July with an approximate 1-hour-long episode of lava fountaining before it ended on 24 July (Fig. 2.5). On 31 August, Strombolian eruptions at SEC marked the resumption of the activity that lasted until 14 December (Fig. 2.5). It consisted of 20 eruptive episodes at or near the summit of the SEC cone (following Behncke et al., 2008, named “vent A”, Fig. 2.8), accompanied by several lava overflows and, from 12 October, by the periodic effusive activity of a number of vents located on various flanks of the SEC (Fig. 2.8). Between 12 October and 14 December, persistent lava outflow came out of a vent at 2800 m (“vent B”, Fig. 2.8), about 1 km from the SEC. A further vent, opened at 3050 m (“vent C”, Fig. 2.8) on 26 October, delivered lava to the southwest during a near-continuous activity until 7 November, and erupted sporadically until 24 November, producing very small volumes of lava. A vent (“D”, Fig. 2.8) became active on 9 November at 3150 m on the W flank of the SEC cone and erupted intermittently until 27 November.

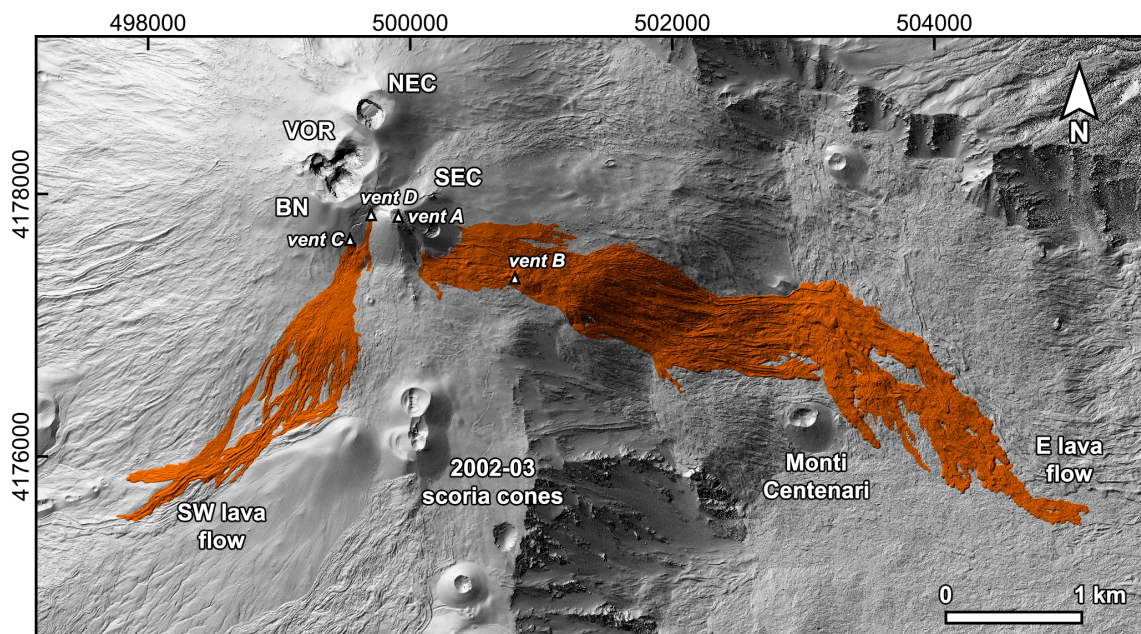


**Figure 2.8.** 2006 lava field with the southwest (SW) and east (E) lava flows highlighted in orange.

NEC = North East Crater, SEC = South East Crater, VOR = Voragine, BN = Bocca Nuova.

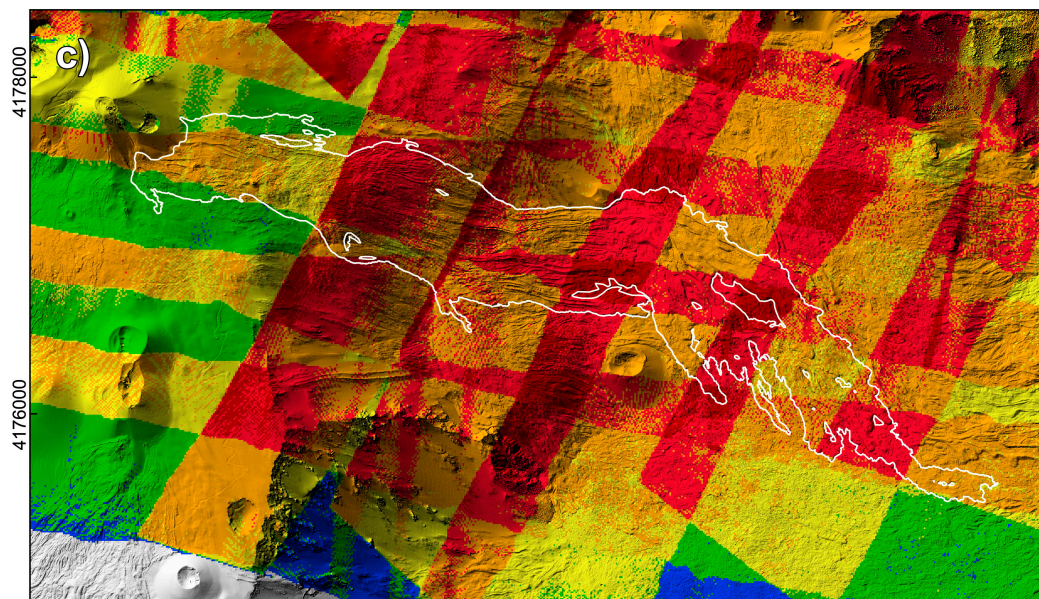
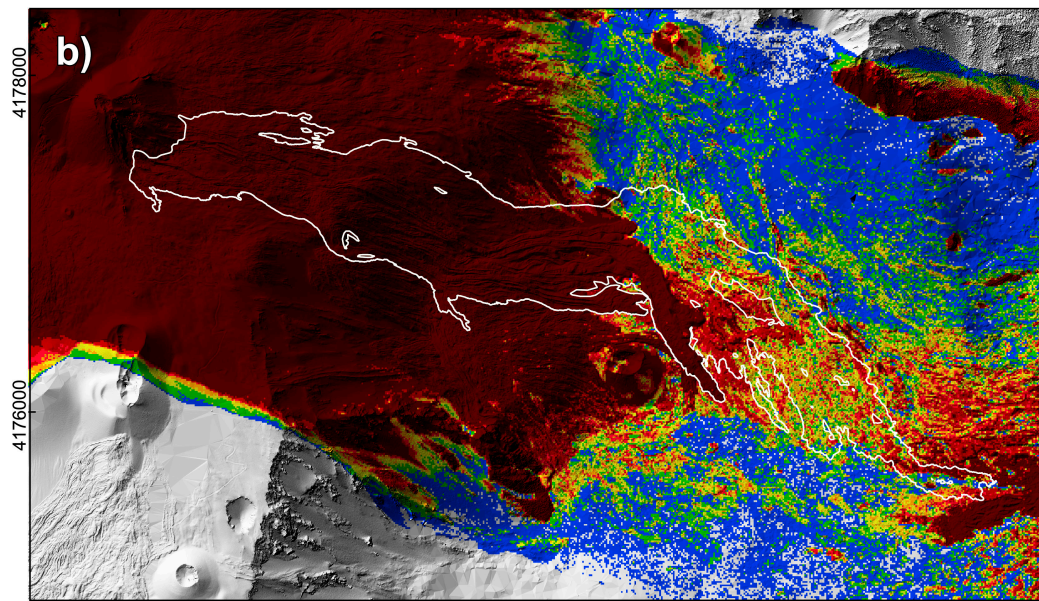
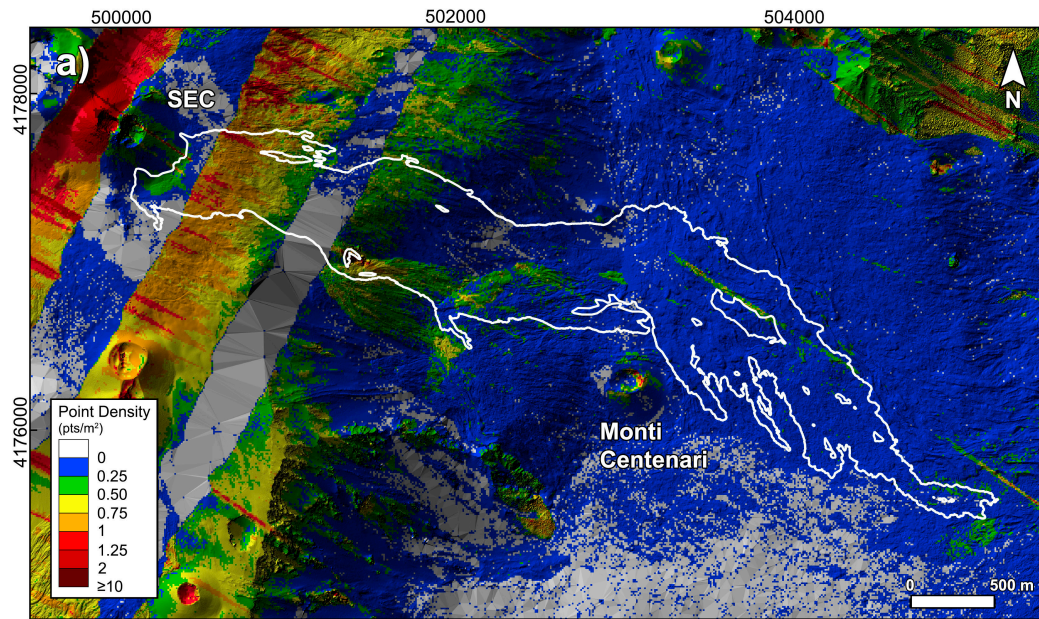


**Fig. 2.9** LiDAR point density map of the east flank of the volcano inundated by the 2006 lava flow. The white line indicates the 2006 east lava flow. a) 2005 LiDAR point density map; b) 2006 LiDAR point density map; c) 2007 LiDAR point density map. The legend is the same for all maps.

At the time of the pre-eruptive acquisition, the 2004-05 Etna eruption ended ~7 months earlier and the first activities of the 2006 eruption began ~10 months later. During the sin-eruptive acquisition, the lava flow of 14-24 July, the products linked to the SEC Strombolian activity and the earlier lava (~10 days) emitted from 12 October to 14 December 2016 were already emplaced. At that time the lava field had extended down the steep W slope of the Valle del Bove north of M. Centenari (Fig. 2.8), with numerous overlapping lobes that showed pronounced flow channels. The post-eruptive LiDAR survey was conducted about 6 months after the 2006 eruption had ceased, but additional eruptive products (tephra and lava) were emplaced during four further paroxysmal eruptive episodes of the SEC, which took place on 29 March, 11 and 29 April, and 6-7 May 2007 (Fig. 2.5).

Since the volume of the 2006 lava flow emplaced on the SW flank has already been calculated by Favalli et al., (2009), in this work we only deal with the products emplaced on the E flank (Fig. 2.9).

### 2.3.3 2007-2010 eruptive events

The eruptive activity between the 2007 and 2010 LiDAR surveys consisted of three powerful episodes of lava fountaining, tephra emission and production of lava flows from the proto-new south east crater (NSEC) on 4-5 September 2007, 23-24 November 2007, and 10 May 2008, followed by an eruption on the upper eastern flank of Etna from 13 May 2008 to 6 July 2009 (Fig. 2.5 and 2.10). The point density of the 2007 and 2010 LiDAR clouds in the eastern sector of the volcano was extremely high and very similar (cfr. Fig. 2.9c and 2.11).

The three paroxysmal episodes at the proto-NSEC were the first eruptive manifestations of this vent after the demise of the old southeast Crater, which last erupted in March-May 2007 (Falsaperla et al., 2014). The 4-5 September 2007 episode was exceptional, because sustained high lava fountaining continued for more than 10 hours, an unprecedented event in the recent eruptive history of Etna (Andronico et al., 2008). Heavy tephra fallout to the east of the proto-NSEC formed an elongated ridge, about 1.5 km long, while a lava flow travelled 4.6 km eastward into the Valle del Bove (Fig. 2.10). The 23-24 November 2007 episode was rather similar, although somewhat shorter (~6h), producing a 4.4 km long lava flow, mostly overriding the 4-5 September 2007 flow. Finally,

the 10 May 2008 episode lasted 4 hours but produced a 6.2-km-long lava flow, one of the longest summit-fed lava flows known for Etna (Behncke et al., 2005; Bonaccorso et al., 2011a).

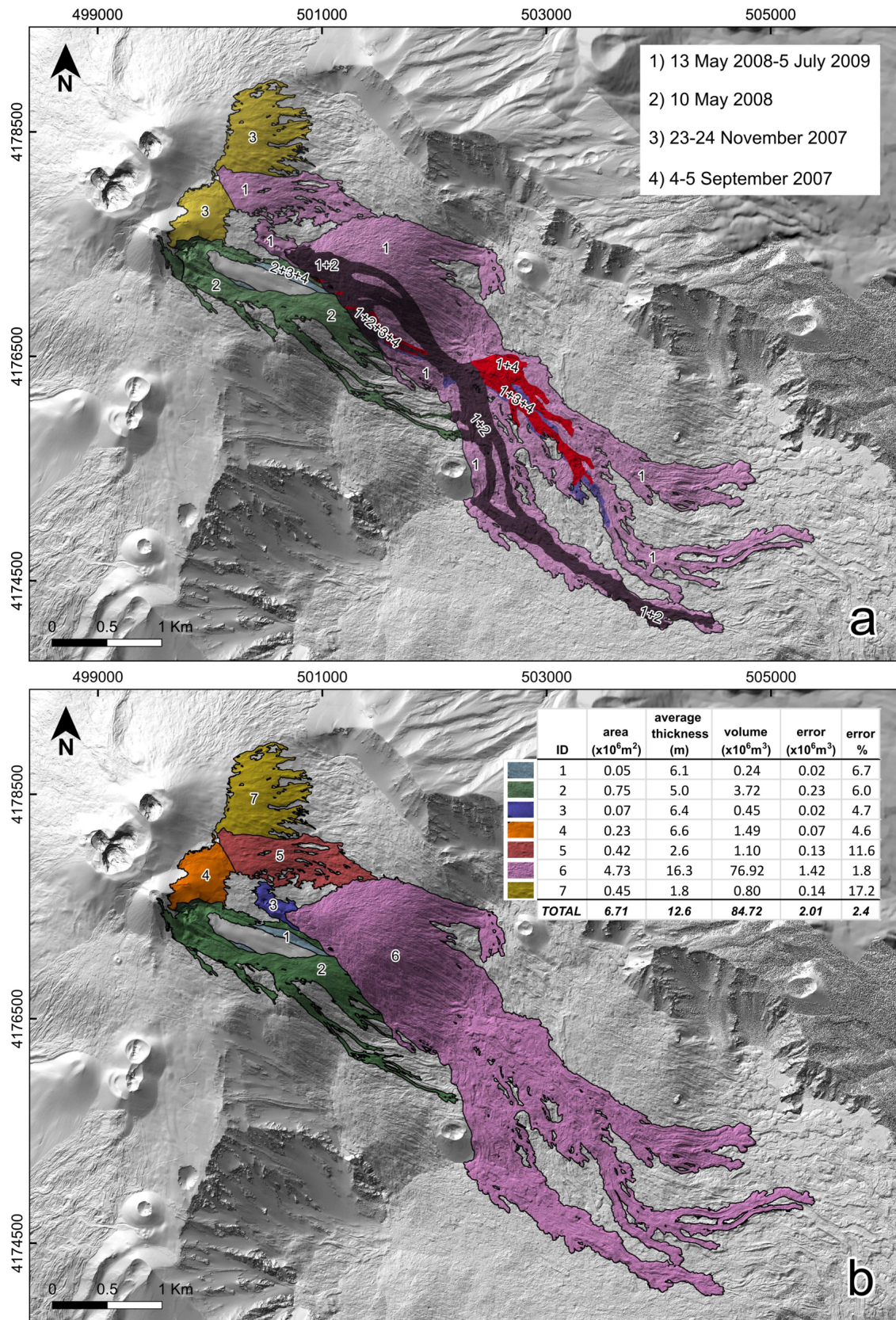


**Fig. 2.10.** Maps of eruptive products emitted from 2007 to 2010. (a) Map of eruptive products in 2007-2009 projected onto the 2010 DEM. (b) 2010 DEM with outline of the areas for which partial thicknesses and volumes were calculated.

Three days after this latest event, a lateral eruption started on the upper eastern flank (Bonaccorso et al., 2011b; Bonforte et al., 2013; Corsaro and Miraglia 2014), where an eruptive fissure opened, and from which high lava fountains and rheomorphic lava flows were erupted for <1h. The fissure then propagated further SE, producing a Strombolian activity and the emission of lava flows from 10 vents. The lava formed two main branches on the Valle del Bove floor, the most southerly of which followed the path of the 10 May lava flow, while the northern branch extended in the northern part of the Valle del Bove. This latter branch reached a length of 6.5 km.

The flank eruption ended on 6 July 2009, after 419 days of lava emission. This makes the 2008-2009 eruption the longest Etnean flank eruption since the voluminous 1991-1993 event, and the second longest since the early 17th century (Behncke et al., 2005; Neri et al., 2011).

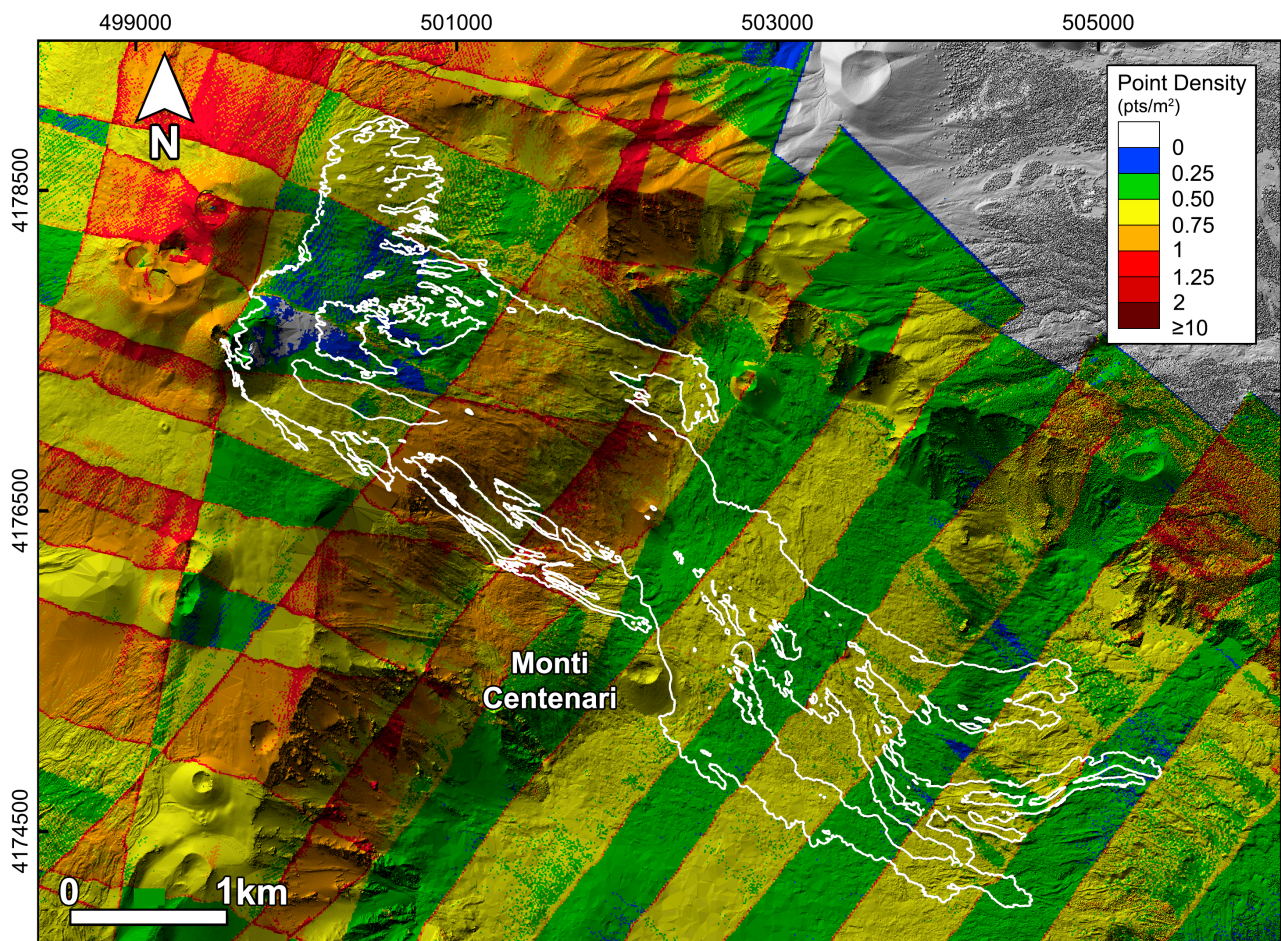


**Fig. 2.11** LiDAR point density map in the area interested by the 2007-2009 activity. The white line indicates the Mount Etna products emitted from 2007 to 2010.

## 2.4 2004-05 lava flow volume

Since the first lava flows of the 2004-05 eruption were emitted before the 2004 acquisition, the volume of these early products was calculated using the 10-m resolution TINITALY DEM as pre-emplacement data (Tarquini et al., 2012a), and the 2004 LiDAR DEM as post-emplacement data. TINITALY DEM derived from the 1998 topographic map at the 1:10,000 numeric scale of the Provincia Regionale di Catania (Sicily), published in 1999. As these DEMs have different resolution and result from two different sources, the expected percentage error will be higher than the one obtained by comparing the LiDAR DEMs. Moreover, the area inundated by these early lava flows was identified by using the difference between very different DEMs acquired five years apart during which Mount Etna was affected by the 1999, 2001 and 2002-03 eruptions. The results of these comparisons are shown in Fig. 2.12.

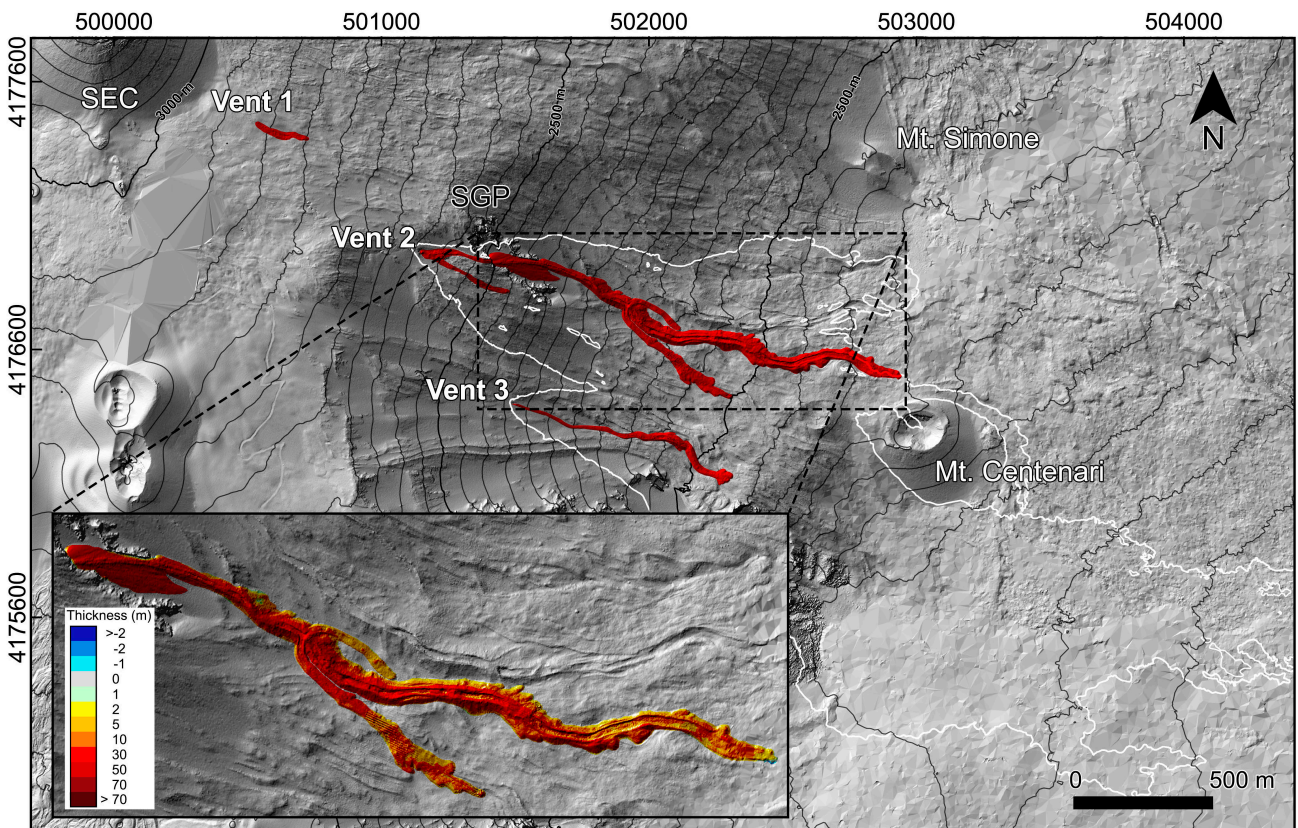


**Fig. 2.12** The 2004-05 lava flow imaged on 16 September 2004 with the inactive lava flow from Vent 1, the development of the early stage of the Vent 2 lava flow field and the narrow lava flow running from Vent 3. The white continuous line represents the final 2004-05 lava flow field. In the inset, the thickness of the lava from Vent 2 derived from the difference between the 2004 LiDAR-DEM and TINITALY DEM.

Topographic changes obtained by subtracting 2005 and 2004 LiDAR-derived DEMs are shown in Fig. 2.13. The calculation of changes in volume by using multi-temporal DEMs is often affected by errors caused by mismatching in  $x$ ,  $y$  and  $z$  between the same areas imaged by the different acquisitions. Fig. 2.13 shows that the distribution of errors outside the area affected by real changes

does not have a systematic behaviour. As a consequence, local mismatching between DEMs was deemed negligible even considering the presence of the wide areas with low-point density in both LiDAR data. The  $\sigma_{\Delta z}$  calculated by using the areas outside the 2004-05 lava flow was 0.44 m. The difference between the 2005 and 2004 LiDAR-DEMs showed a combined volume gain of  $\sim 62.2 \pm 1.2 \times 10^6 \text{ m}^3$  for an identified total area covered by volcanic products of  $\sim 2.8 \times 10^6 \text{ m}^2$ . The average thickness was 22 m, with a maximum thickness reaching 90 m.

For the volcanic products emitted before the 2004 LiDAR survey, we measured the volume changes only for the lava emitted from Vent 2 (Fig. 2.12) in the time interval between 7 and 16 September 2004. The volume of lava emitted from Vent 3 was not calculated because it had been largely affected by the 1999, 2001 and 2002-03 eruptions. Following the same workflow described for the LiDAR-DEM differences, we obtained for the lava from Vent 2 a volume gain of  $\sim 1.1 \pm 0.2 \times 10^6 \text{ m}^3$  for an identified total area covered by volcanic products of  $\sim 0.1 \times 10^6 \text{ m}^2$ , with an average thickness of 8.63 m. The resulting mean eruption rate at the beginning of the activity was  $\sim 1.4 \pm 0.3 \text{ m}^3 \text{ s}^{-1}$ .

In conclusion, the volume assessed by DEM comparison for the 2004-05 lava flow was  $63.3 \pm 1.4 \times 10^6 \text{ m}^3$ . These data were slightly underestimated because they did not take into account the products from Vent 1 (a negligible value with respect to the total estimated volume) and the early products of Vent 3. The resulting mean eruption rate for the 2004-05 eruption was  $\sim 4.1 \pm 0.1 \text{ m}^3 \text{ s}^{-1}$ .

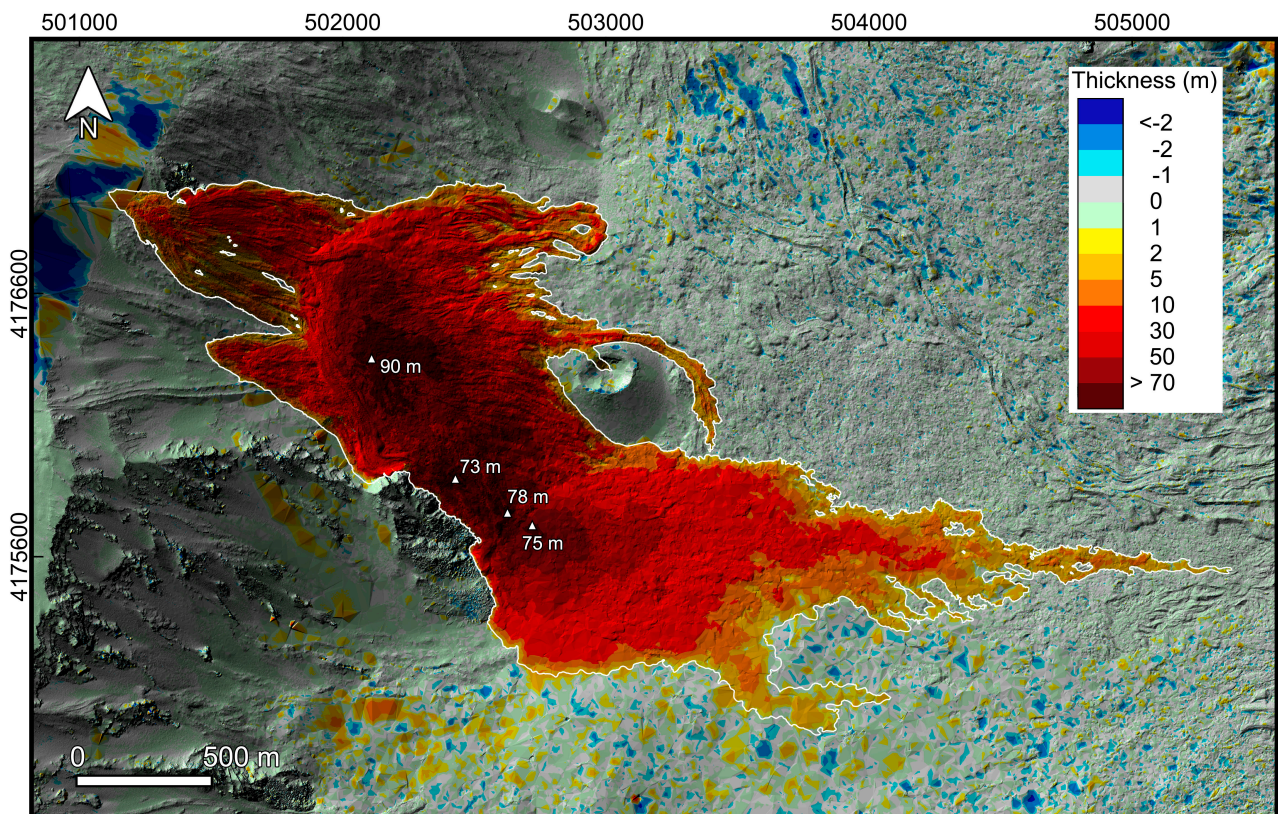


**Fig. 2.13** Thickness map of the 2004-05 lava flow field obtained by subtracting the 2005 and 2004 LiDAR-derived DEMs. Relevant maximum thicknesses are shown.

## 2.5 Volume and dynamics of the 2006 lava flow

The LiDAR data used for the topographic change detection related to the 2006 activity have been partially used in other works. Favalli et al., (2009) mapped and calculated the volume of the 2006 SW lava flow (Fig. 2.8) by subtracting the 2007 from the 2005 data. The volume results being  $4.56 \pm 0.72 \times 10^6 \text{ m}^3$ , Favalli et al., (2011) produced the 2006-2005 DEM difference map in order to show the extent of the eastern lava field of the 2006 eruption at the beginning of the 2006 LIDAR survey, with no further qualitative analyses. In the following we focus on the 2006 eastern lava field, erupted from “vent B”, which was the only active lava field during the 2006 LIDAR survey. We produced three DEM difference maps (Figs. 2.14a, b and c): 2006-2005, 2007-2006 and 2007-2005.

The 2006-2005 DEM difference map (Figs. 2.14a) shows the topographic changes in the eastern sector of Mount Etna from the beginning of the 2006 eruptive period (14 July 2006) to the 2006 LIDAR survey (17 November 2006). The main morphological changes were, of course, due to the emplacement and flow of the eastern 2006 lava flows. At that time, the newly emplaced lava field was already very complex and consisted of a number of long, branched channel-fed flows spilling down into the Valle del Bove. This lava erupted from “vent B” at 2800 m, ~0.5 km east of the base of the SEC cone. The active flow field was about ~500 m wide and extended for ~4.1 km down to an elevation of 1680 m, close to the base of Monte Centenari. To the south of the distal part of the 2006 lava field and west of Monte Centenari appeared an area of conspicuous subsidence, of up to 2 m in one year, of the lava field emplaced during the 2004-2005 eruption (Figs. 2.14a). Furthermore, the DEM clearly showed a scar resulting from the mechanical erosion of active lava flows into this structurally and lithologically weakened sector of the cone (Behncke et al., 2008, 2009; Behncke 2009). Minor subsidence was also evident on the W and SW flanks of the SEC cone, where significant ground deformation occurred as a result of lateral magma intrusion away from the main SEC conduit. Such events led to the activation of vents “C” and “D” on 26 October and 8 November 2006.

The 2007-2006 DEM difference map (Figs. 2.14b) shows the complex morphological evolution of the 2006 lava field following the survey of 17-18 November 2006. The main lava field emplaced before 17 November continued to develop and advance further downslope into the Valle del Bove, reaching a final elevation of 1480 m and a total length of ~5.6 km during the last two weeks of the eruption. Much of this additional lava was emplaced as rather uniform, relatively thin-sheeted flow

units, differently from pronounced flow channel development during the period up to the LiDAR survey. To the south of the eastern 2006 lava field, another large compound lava field developed, which was produced during four paroxysmal eruptive episodes in the spring of 2007. It initially flowed parallel to the 2006 lava field but then fanned out southeast- and southward upon reaching the main bulge of the 2004-05 lava field. Minor lava flows were also emplaced toward south from the southern and southeastern flanks of the SEC. Some of these flows occurred during the late stages of the 2006 eruption, and others during the first two spring 2007 paroxysms. In a sector to the east and northeast of the SEC, a new ash deposition was evident. Some changes in the morphology of the SEC cone are evident, such as the addition of a layer of pyroclastics. Substantial filling of the SEC scar is also visible, as well as the formation of a small graben on the NW side of the cone and of a pit crater on the lower ESE flank of the cone, which occurred on 20 May 2007. Finally, it is evident from the 2007-2006 DEM difference map that subsidence of the 2004-2005 lava field significantly slowed down, with only minor volume loss visible immediately to the eastern margin of the spring 2007 lava field.

The 2007-2005 difference (Fig. 2.14c) shows the overall main volumetric changes produced on the eastern flank by the 2006 eruptions, and by the paroxysms in March-May 2007. Fig. 2.14 shows that the distributions of error outside the area affected by real changes did not have a systematic behaviour. Consequently, local mismatching between DEMs was considered negligible and not further corrected. The displacement in  $z$  between the 2007 and 2005 LIDAR DEMs, calculated outside the region involved in the emplacement of the lava field, was 0.59 m and the area inside which we calculated the volume was  $2.48 \times 10^6 \text{ m}^2$ , giving an error of  $1.5 \times 10^6 \text{ m}^3$ , due to the intrinsic DEM resolution. To this value we added the uncertainties resulting from both ash deposition and 2004-2005 lava flow subsidence, which we estimated to be about  $0.8 \times 10^6 \text{ m}^3$  each. This was added to a total, very conservative error in the emplaced lava volume of  $3.1 \times 10^6 \text{ m}^3$ . The total lava volume emplaced on the eastern flank in the 2005-2007 interval was calculated to be  $\sim 42.0 \pm 3.1 \times 10^6 \text{ m}^3$ . The average thickness of the lava was 17 m, with a maximum thickness reaching 52 m.

The total volume of  $\sim 42.0 \pm 3.1 \times 10^6 \text{ m}^3$  included lavas erupted during three phases of the activity: July 2006, September-December 2006, and March-May 2007. The volume of the July 2006 eruptive phase was estimated at  $\sim 4 \times 10^6 \text{ m}^3$  (Neri et al. 2006; Vicari et al., 2009), and the volume of products erupted during the paroxysms in spring 2007 at  $\sim 4.5 \times 10^6 \text{ m}^3$  (unpublished data). Therefore, the volume of lava emplaced on the eastern flank between September and December 2006 could be inferred to be  $\sim 33.5 \pm 4 \times 10^6 \text{ m}^3$ . Considering also the contribution of the south lava field, the total inferred volume of the 2006 eruption is  $\sim 38 \pm 5 \times 10^6 \text{ m}^3$ .

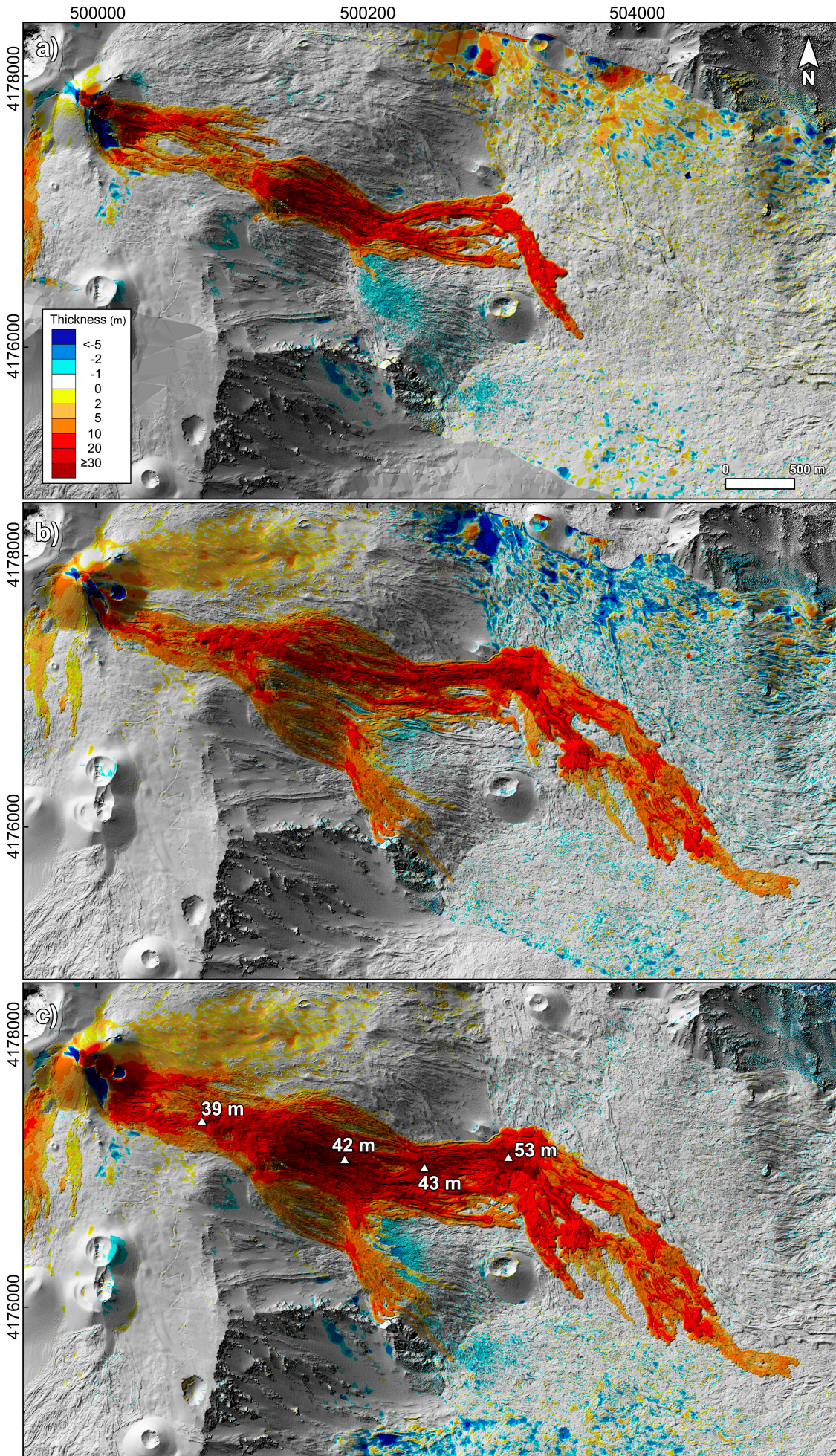


**Fig. 2.14** DEM difference maps calculated from the 2005, 2006 and 2007 LiDAR dataset. a) 2006-2005 DEM difference: the state of the east lava field at the beginning of the 2006 LiDAR survey; b) 2007-2006 DEM difference: the compound growth of the lava field following the days of the 2006 survey; c) 2007-2005 DEM difference: whole eastern lava field of the 2006 Mount Etna effusive eruption. In the last case, the lava field contains the eruptive products emitted during the 2007 activity.

## 2.6 Topographic change detection from 2007 to 2010

The difference between the 2007 and 2010 LiDAR-DEMs shows a combined volume gain of  $86.4 \pm 2.1 \times 10^6 \text{ m}^3$  for an identified total area covered by volcanic products of  $6.86 \text{ km}^2$  (Fig. 2.10). The  $\sigma_{\Delta z}$  calculated by using the areas outside interested by deposition is 0.30 m. Comparison of the 2007 and 2010 DEMs revealed a number of morphological changes that affected the area of the Etna summit craters (Fig. 2.15). The volume loss (blue areas in Fig. 2.15) mainly on the northern and western flanks of the summit area probably reflected a combination of wind erosion of unconsolidated tephra deposits and, to a minor degree, compaction of snow trapped below tephra deposits, where thick snow can survive under tephra for many years. Some loss was also visible on the upper eastern and southern slopes of Mt. Barbagallo (MtB in Fig. 2.15), the large pyroclastic cones formed in 2002-2003. This was the continuation of the degradation processes dominated by wind erosion and gravitational sliding, enhanced by the passage of countless tourists per year, as described by Fornaciai et al., (2010b).

Significant morphological changes occurred at the proto-NSEC, which in 2007 was a simple, sub-circular pit of about 90-100 m in diameter, and in 2010 had evolved into a 160-190 m wide chasm, tens of meters deep and with vertical walls. The proximal pyroclastic products of the three paroxysms in September and November 2007 and on 10 May 2008 accumulated around the proto-NSEC to thicknesses up to  $\sim 40 \text{ m}$ , and with a volume of  $\sim 2.5 \times 10^6 \text{ m}^3$  (areas 1, 4, and 7 in Fig. 2.10).

Lava flows were emplaced exclusively to the east of the summit area, covering the western headwall and the floor of the Valle del Bove (Fig. 2.15). The 2008-2009 lava flow-field, which was emitted from an eruptive fissure at 3050-2620 m elevation on the upper eastern flank (Bonaccorso et al., 2011b) can be easily distinguished for its greater thickness compared to the lavas of the preceding paroxysmal episodes (Fig. 2.15). However, the flank eruption lavas buried a large proportion of the lavas of the preceding paroxysms. To obtain the area and volumes of the buried lavas (subtracted from the total volume obtained from the DEM difference of the 2008-2009 lava

flow area), we referred to maps and volumes obtained from field surveys and aerial photography carried out after each paroxysm. These volume data were generally affected by a maximum error of 20% (Behncke et al., 2006, 2014).

Of the 4-5 September and 23-24 November 2007 lavas, only small portions were not covered by 2008-2009 flank eruption lavas (Fig. 2.10), and thus their lava volumes could not be distinguished from the 2007-2010 DEM differences. The areas and volumes of these lavas, as obtained from field and aerial surveys, were 0.64 km<sup>2</sup> and  $\sim 1.1 \times 10^6$  m<sup>3</sup> respectively for the 4-5 September paroxysm; and 0.72 km<sup>2</sup> and  $\sim 1.6 \times 10^6$  m<sup>3</sup> respectively, for the 23-24 November 2007 paroxysm.

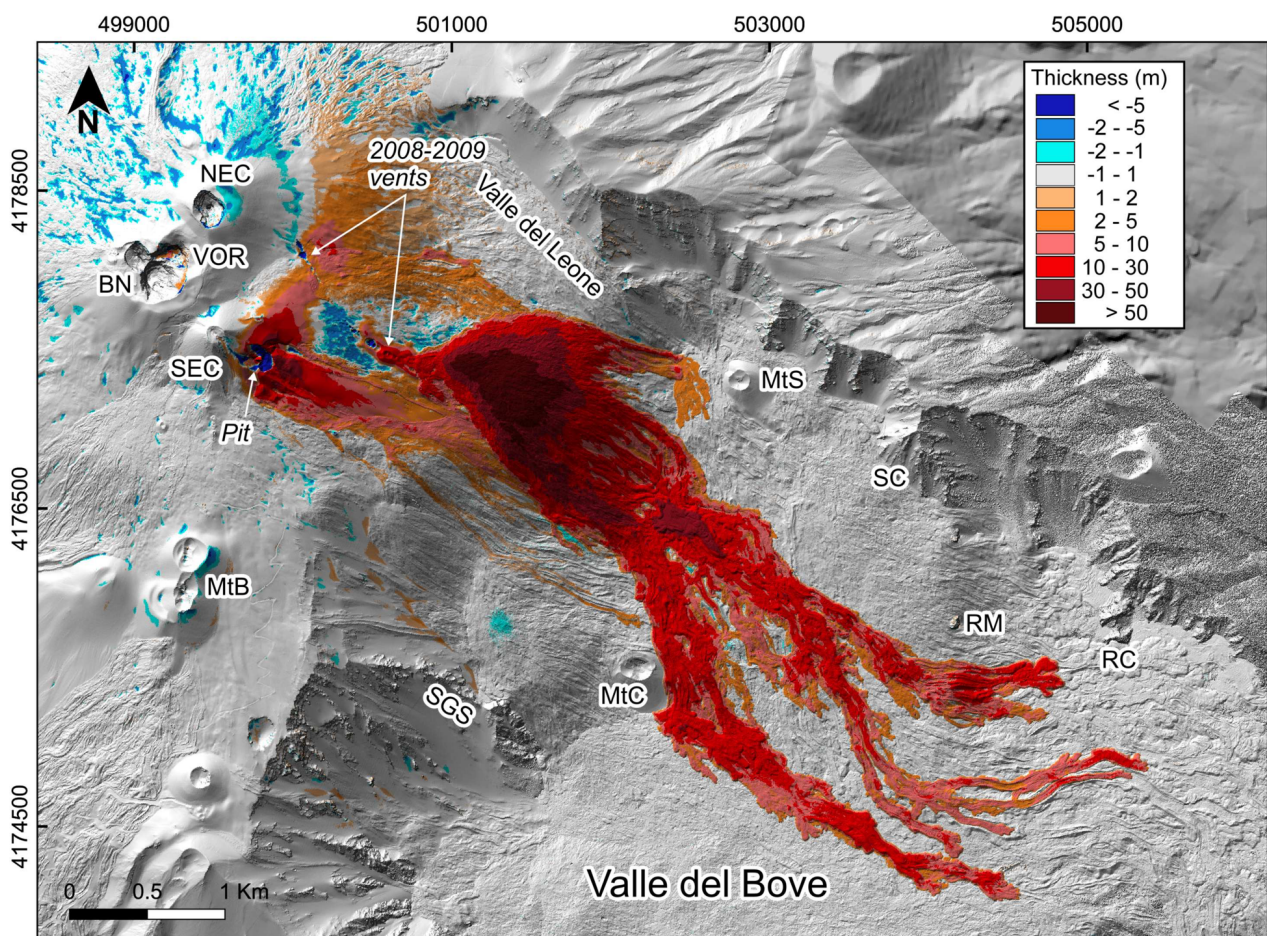


**Fig. 2.15** DEM showing thicknesses of deposits (mostly lava flows) of the eruptive activity between the 2007 and 2010 LiDAR surveys. The thickness changes between ca. -1 and 1m have been left transparent. NEC = Northeast Crater; VOR = Voragine; BN = Bocca Nuova; SEC = Southeast Crater; MtB = Monti Barbagallo; SGS = Serra Giannicola; MtC = Monti Centenari; MtS = Monte Simone; SC = Serracozzo; RM = Rocca Musarra; RC = Rocca Capra.

For the 10 May 2008 paroxysm at the proto-NSEC, Bonaccorso et al. (2011a) estimated a volume of  $1 \times 10^6$  m<sup>3</sup>. However, the 10 May 2008 lavas were partly distinguishable in the 2007-2010 DEM difference map (area 2 in Fig. 2.10), where they constituted an area of 0.72 km<sup>2</sup> with an average thickness of 3 m, yielding a volume of  $\sim 2.2 \times 10^6$  m<sup>3</sup> for this area. The total area of lava

emitted on that day, as mapped from aerial photography obtained on 12 May 2008, was  $1.91 \text{ km}^2$ . By assuming a minimum average thickness of 3 m from field observations and consistent with the LiDAR-derived thickness for the portion of the lava field covered by the 2008-2009 flank eruption, a volume of  $\sim 3.6 \times 10^6 \text{ m}^3$  was obtained for this area, and its total volume was  $2.2 + 3.6 = 5.8 \times 10^6$ . This places the 10 May 2008 paroxysm among the largest events of this type documented on Etna in recent decades. The average effusion rate during this paroxysm was thus close to  $\sim 400 \text{ m}^3 \text{ s}^{-1}$ , comparable to the highest effusion rates of similar but shorter events in recent years (Behncke et al., 2006, 2014; De Beni et al., 2015).

Finally, the volume of the 2008-2009 lavas could be calculated by subtracting the volumes of the buried lavas of 4-5 September, 23-24 November and 10 May 2008 from the total volume obtained for the area of the flow fields (areas 3+5+6 in Fig. 2.4):  $78.47 \times 10^6 \text{ m}^3 - (2.2 + 1.1 + 1.6) \times 10^6 \text{ m}^3 = 73.57 \times 10^6 \text{ m}^3$ . The effusion rate, averaged over the 419 days of the 2008-2009 eruption, was thus  $\sim 2 \text{ m}^3 \text{ s}^{-1}$ . The average thickness of the 2008-2009 lava flow-field was 14 m, but locally the thickness exceeded 50 m, mainly in the area where a huge lava shield grew by the repeated overlapping of relatively short (1-1.5 km long) lava lobes, i.e., south of the Valle del Leone (Fig. 2.15).

---

## Chapter 3

---

### **Visualization and comparison of DEM-derived parameters. Application to lava flows**

Morphometry of lava flow are crucial for investigating the dynamics of its flow and emplacement. Channels fed-lava flow are related to the properties of the lava when the channel was active (e.g. supply rate, rheology and heat loss) and to the local topography over which the flux was flowing. Detailed measurements of channel geometry are also largely used as benchmark and boundary conditions for lava flow modeling. However, delineating and measuring the basic elements of lava flows is not easy also using remote sensing technologies because the complex nature of volcanic terrain, which is made of numerous superimposed flows, even emitted during the same eruption, and often draped by huge fallout of ash. The high detail and spatial extension of the 3D data supplied by the new technologies demand an effort in suitably visualizing this wealth of data. Finding proper techniques to adequately parameterize DEMs and represent maps is required for effective land-surface quantitative analysis and, currently, it is pursued through multidisciplinary approaches (e.g. Buckley et al., 2004; Chiba et al., 2008; Kennelly 2008; Mitasova et al., 2012).

A common, general workflow for land surface DEM-based morphometric analysis requires an initial detailed identification and delineation of surface-specific elements, i.e. pits, peaks, ridge lines, course lines and breaks lines. This is often done through human-made analysis from one or more DEM-derived surface parameters. Olaya (2009) defined surface parameters as measures that can be derived directly from a DEM without further knowledge of the area represented. Common surface parameters are for example DEM-derived slope, aspect and curvature which are generally represented as maps.

In Chapter 3, we review a number of analytical procedures used to parameterize and represent DEMs. For each described parameter, we emphasize which are the specific elements of land surface

that are better highlighted. We first introduce some well-known parameters, such as hill-shaded maps, slope and aspect maps, curvature maps, roughness maps, and then we extend the review to some less common parameters such as Sky View Factor (*SVF*) maps, openness maps, Red Relief Image Maps (RRIM). As a test case, we use a 1200×1200 m LiDAR-derived DEM matrix acquired over the Valle del Bove valley, on Mt. Etna, during the June 2007 airborne LiDAR survey with spatial resolution of 1 m (for details see Favalli et al., 2009). The location and an aerial photo of the test area is shown in Fig. 3.1a, b and c. The test area is characterized by the presence of several lava channels variously superimposed.

Parameters are derived directly from the DEM without additional inputs using a C++ code developed *ad-hoc* that generates all maps in one shot, without assistance. The code and batch file are not designed to be fast for real time elaboration, but to run in background. Since many of the surface parameters reviewed here have the same informative content even if in a slightly different form, it is relevant to evaluate whether or not two maps contain redundant information, before starting time-consuming computer routines. For this reason, the here reviewed surface parameters are cross-compared in order to infer which of them are most uncorrelated. The results are represented as a correlation matrix that can be used for discarding redundant maps. Finally, the highly uncorrelated parameters are used for carrying out the morphometric analysis of a sector of a phonolitic lava flow on Tenerife Island imaged by 10-m resolution DEM (GRAF CAN 2009).

### 3.1 Grid to grayscale image conversion and image enhancement

DEMs and derivative maps are generally in a grid format with values represented by single or double precision numbers. To be displayed, grids must be converted into simple gray-scale or color-map images (8-bit images) in order to associate proper shades of colors to grid data values.

The first way to represent a grid is simply to convert it into a grayscale image where the gray tones correspond to grid values. This can be done using a linear map function, which converts the minimum-maximum (min-max) range values of the grid into the 0–255 standard range of a normal 8-bit grayscale image. However, this will have a very low visual impact if the grid values are not “almost uniformly” distributed in the range (min, max) as can be seen in Fig. 3.1d.

An image can be visually enhanced by stretching its histogram using various techniques. An image histogram is a graphical representation of the number of pixels in an image as a function of their intensity. The greater the histogram stretch, the greater the contrast of the image. Although histogram stretching may produce unrealistic effects, they turn out to be useful for scientific purposes since false-color images are often able to better highlight specific features. However,

histogram stretching can also produce undesirable effects (i.e. visible image gradient) when applied to 8-bit or lower color images. For this reason, it is recommended to apply the histogram stretching on the single or double precision numeric values of the original grid and afterwards convert it into an image.

Area equalization is another commonly used technique for image enhancement in which each intensity class is represented by the same number of pixels (that is by the same area). This produces a histogram which is as flat as possible (Fig. 3.1e). As a consequence, each gray-scale tone is “almost” equally represented and the resulting images appear well contrasted (Fig. 3.1e). However, the gray tone range is no longer directly proportional to the range of values of the original input data. This raises problems when attaching quantity values to the legend of the output image map.

On the contrary, by cutting-off the histogram at upper and lower threshold values, the overall histogram shape and a direct proportionality between grayscale tones and original data values can be maintained (Fig. 3.1f). Upper and lower cut-offs can be either external meaningful values or calculated from the statistical distribution of the values in the original grid. For example, clipping the grid values between  $\mu - 2.5\sigma$  and  $\mu + 2.5\sigma$  (where  $\mu$  is the average pixel value and  $\sigma$  is the standard deviation) usually provide well-contrasted images (e.g. Fig. 3.1f). However different areas have different statistics and therefore the maps of different regions derived using the  $2.5\sigma$  stretching have different legends and are not directly comparable. On the contrary, the same histogram cut-offs produce comparable maps though the resulting image contrast and map readability might not be optimal.

Broadly speaking, a definitive optimal way to convert grids into gray-scale images cannot be recommended. Based on our experience, linearly stretching grid values to the 0–255 grayscale values provides unusable maps in many cases, because of the low contrast in the resulting image. Area equalization works in many occasions but sometimes produces maps that appear too saturated. The  $2.5\sigma$  clipping gives acceptable results in most cases and often provides better results than the equal area equalization. These grayscale images can be considered as a first mandatory step to produce building blocks for more elaborated colored maps. Indeed, they can be composed as a simple HSV (Hue–Saturation–Value) image in order to create a great variety of maps. In the following, all the maps, other than hillshaded and aspect maps, will be represented with  $2.5\sigma$  clipping, which in our opinion gives the best visual enhancement in general, while keeping the shape of histogram.

### 3.2 DEM-derived surface parameters

In simple terms, a land surface can be described as  $z=f(x,y)$ , which means that elevation  $z$  depends solely on planar coordinates  $x$  and  $y$  (Cayley 1859). In computer science, land surfaces are commonly presented as Digital Elevation Models (DEMs), a gridded set of points in Cartesian space attributed with elevation values that describe the Earth's ground surface (see Chapter 1). This means that heights are available at each point in the area of interest (Hengl and Evans 2009) with the exclusion of no data cells.

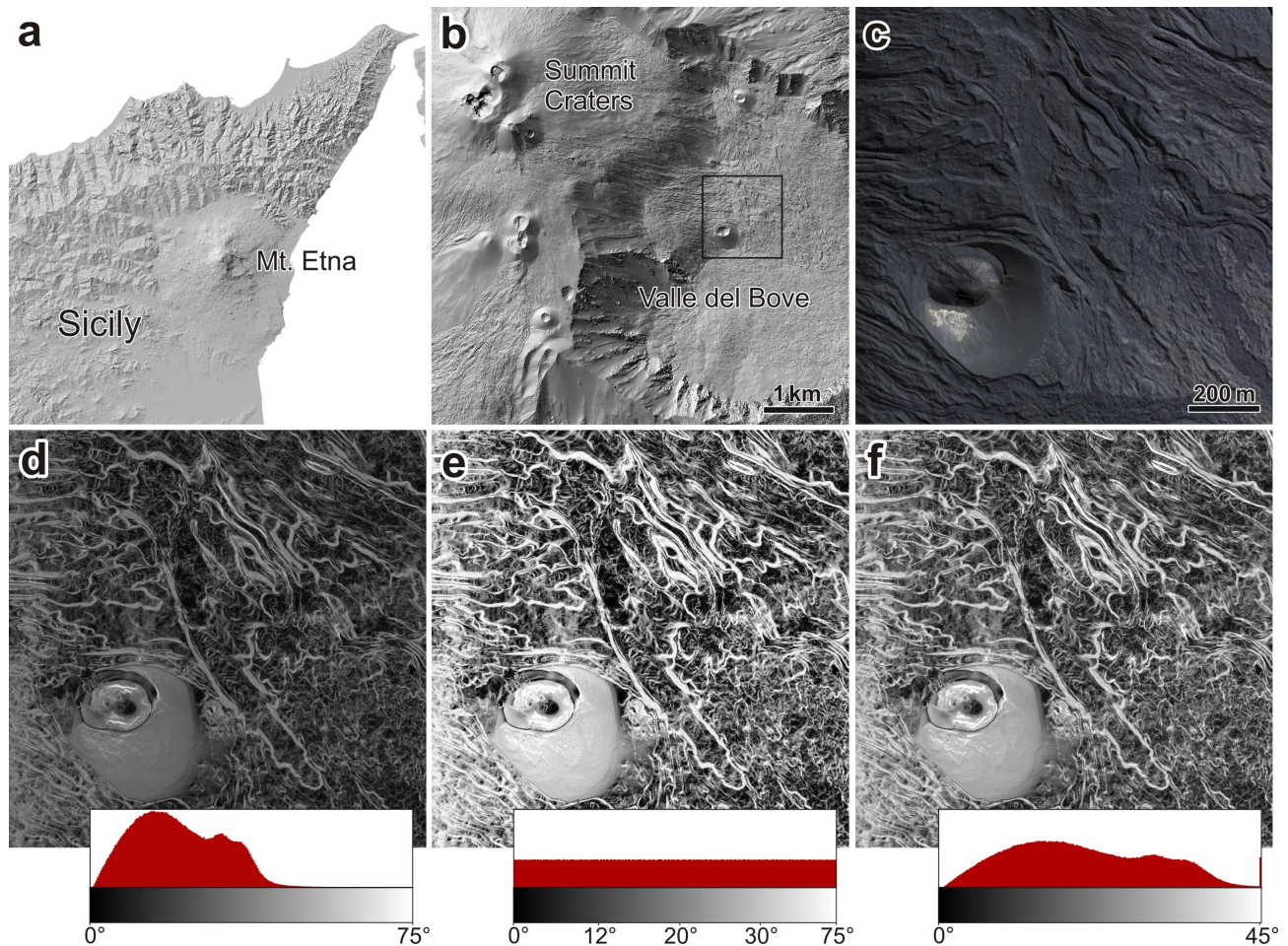


**Fig. 3.1** Mount Etna test area. a) Hillshaded relief of northeast of Sicily Island with the location of Mt. Etna (Tarquini et al., 2012a). b) Hillshaded relief of east flank of Mt. Etna; black contour shows the location of the test area. c) Aerial photo (downloaded from [sif.regione.sicilia.it](http://sif.regione.sicilia.it)) of the test area with dimension of 1200 m  $\times$  1200 m. Frames d, e and f show grayscale image representations of the slope calculated from a high resolution DEM; insets display the histograms and legends of the slope maps (in degrees). d) Linear mapping of the (min, max) values of slope onto the (0, 255) intensity range of the gray tones: all slope values are faithfully represented but the image is poorly contrasted. e) Histogram equalization: the image has an optimal contrast but the form of the original histogram is completely lost and a correct display of the legend is very problematic. f)  $2.5 \sigma$  histogram stretching: the image is well contrasted and the original shape of the most populated part of the histogram is maintained.

To derive some basic DEM parameters such as hill-shade, slope and aspect, the derivatives of the DEM in each point must be calculated. Since the DEM is a discrete square mesh, DEM gradients can be calculated by applying some filter masks to the DEM matrix. The simplest approach is to use central differences so that the approximated  $x$  and  $y$  derivatives of the DEM matrix  $L$  at a point identified by the integer indexes  $(i, j)$  are:

$$L_x(i, j) = (L(i+1, j) - L(i-1, j))/(2\Delta x) \text{ and } L_y(i, j) = (L(i, j+1) - L(i, j-1))/(2\Delta y) \quad (3.1)$$

These expressions correspond to the application of the following filter masks:

$$L_x = \frac{1}{2\Delta x} \begin{bmatrix} 1 & 0 & -1 \end{bmatrix} \cdot L \quad \text{and} \quad L_y = \frac{1}{2\Delta y} \begin{bmatrix} 1 \\ 0 \\ -1 \end{bmatrix} \cdot L \quad (3.2)$$

where the square brackets identify the two kernels which are convolved with the matrix  $L$  to calculate approximations of the derivatives. Since the derivatives have usually higher noise levels than the primitive, the following Sobel kernels (Sobel and Feldman 1973), which compute the gradient with a degree of smoothing, are preferred:

$$L_x = \frac{1}{8\Delta x} \begin{bmatrix} 1 & 0 & -1 \\ 2 & 0 & -2 \\ 1 & 0 & -1 \end{bmatrix} \cdot L \quad \text{and} \quad L_y = \frac{1}{8\Delta y} \begin{bmatrix} 1 & 2 & 1 \\ 0 & 0 & 0 \\ -1 & -2 & -1 \end{bmatrix} \cdot L \quad (3.3)$$

### 3.2.1 Shaded relief maps

Shaded relief maps are the most common way to represent DEMs, since they show the detail of topographic features in an intuitive manner (e.g. Horn 1981). Various algorithms are used to calculate hill-shaded maps, most of them depend on the type and number of light sources and on the reflectivity associated with the DEM surface. Users usually find that an oblique illumination from the northwest with a light source shining from a moderate angle between the horizon and zenith, provides the most intuitive images of the shape of the terrain (Kennelly 2008)

Generally, the hill-shading implemented in GIS software is based on two assumptions: i) the illuminated surface is Lambertian (i.e. it is an ideal diffusely reflecting surface and therefore the apparent brightness of the surface is the same regardless of the observer angle of view); ii) only one light source (usually referred as the sun) is present, at an infinite distance. Hill-shading simulates

the diffusion of an artificial light arriving from a single point source at a given altitude (inclination) and azimuth (declination). Terrain features, irrespective of the angle at which are viewed, have an apparent brightness which is proportional to the cosine of the angle between the normal to the surface and the light-direction vector pointing from the surface to the light source. Supposing the surface to be uniformly white, then the hill-shading gives a typical grayscale image. In the examples of Fig. 3.2 no active shadow is used. Using an active shadow, even if more realistic, would cast shadow on some areas of the DEM preventing the visualization of any detail in such zones.

As reported by Smith and Clark (2005), shaded relief visualizations are subject to azimuth biasing, altering the position of breaks in slope. As a consequence several features may change shape, appear or disappear (Smith 2011). In the shaded relief map, the perception of convexity and concavity surfaces depends on the relative location between the viewer and the light source. Changing the direction of illumination to the opposite side, the concavities appear to turn into convexities and vice versa. For example, the lava channels 1 and 2 in Fig. 3.2b appear to have opposite elevation in Fig. 3.2c.

The major drawback of shaded relief maps is that linear features (as lava channels), or otherwise features with a certain orientation, may be displayed in a different manner depending on the direction of illumination. This is because ridges and valleys that are oriented perpendicularly to the direction of illumination are much more enhanced than those that are parallel. For example, the terminal part of lava flow 1 is well visible in Fig. 3.2b and 3.2e while it is poorly visible in Fig. 3.2a and 3.2c. Moreover, the direction of illumination affects the visual perception of the surface roughness in general (Ho et al., 2006).

To avoid a preferential azimuth direction in the lighting some tricks can be used, such as: i) using a single light point source at an elevation angle of  $90^\circ$  (i.e. vertical illumination, see Fig. 3.2f), in this case for a Lambertian surface the brightness will be proportional to the cosine of the local slope; ii) producing multiple shaded relief images with illumination from multiple directions (Smith and Clark 2005); iii) producing a single hill-shaded image with more than one light source; and iv) using a non-point source illumination that has no preferential azimuth orientation, such as a uniformly illuminating sky.

In general, after reviewing several visualizations methods, Smith and Clark (2005) and Hillier and Smith (2008) concluded that there is no single visualization techniques that is ideally suited to geomorphological mapping, but the interpreter should prefer techniques that do not introduce azimuth biasing.

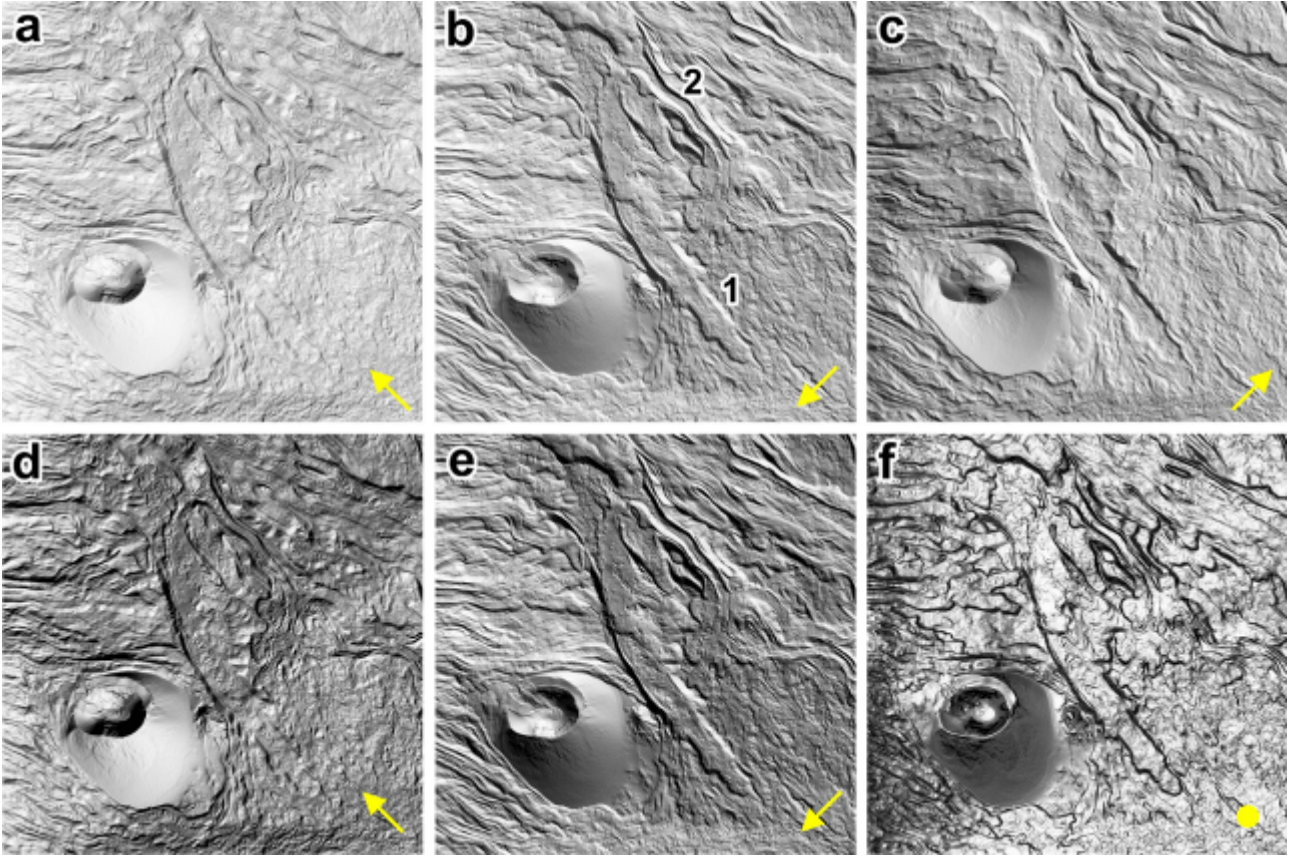


**Fig. 3.2** Shaded relief maps of an area of 1200 m × 1200 m on Mt. Etna. Yellow arrows indicate the direction of illumination. a) Sun azimuth = 135°, sun elevation angle = 45°. b) Sun azimuth = 45°, sun elevation angle = 45°; label 1 identifies the terminal section of a lava flow and label 2 identifies a lava channel. c) Sun azimuth = 225°, sun elevation angle = 45°. d) Sun azimuth = 135°, sun elevation angle = 45°, 2.5  $\sigma$  histogram stretching applied. e) Sun azimuth = 45°, sun elevation angle = 45°, 2.5  $\sigma$  histogram stretching applied. f) Sun elevation angle = 90°, 2.5  $\sigma$  histogram stretching applied. The angle of illumination, or azimuth, clearly affects the way features appear on shaded relief maps.

### 3.2.2 Slope, aspect and curvature maps

Slope, aspect and curvature are here derived directly from the first and the second derivatives of the elevation matrix (e.g. Zevenbergen and Thorne 1987), calculated by applying Sobel filters (Eq. 3.3). The maximum slope ( $S$ ) is given by definition by:

$$S = \arctan \left[ \sqrt{\left( \frac{\partial z}{\partial x} \right)^2 + \left( \frac{\partial z}{\partial y} \right)^2} \right] \quad (3.4)$$

In the slope map of Fig. 3.3a, the brightness of each pixel is inversely related to slope angle so that flat areas are bright and steep areas are dark. The resulting image has similar appearance to relief-shaded terrain, without the illumination bias (Smith 2011). Peaks, pits and passes have zero local slopes. With opportune contrast enhancements (such as applying an area equalization to both

of them), slope maps and vertically illuminated hill-shaded models are identical, and both eliminate the azimuth biases typical of obliquely illuminated single-point-source hill-shading (cf. Fig.3.2f and 3.3a).

The aspect angle ( $\theta$ ) is defined as the azimuth direction at which the maximum slope is achieved:

$$\theta = \arctan\left[\left(-\frac{\partial z}{\partial y}\right) / \left(-\frac{\partial z}{\partial x}\right)\right] \quad (3.5)$$

Fig. 3.3d represents the aspect map. Since the aspect corresponds to the azimuthal direction of the gravity force component tangential to the surface, it is said that aspect indicates the flow line direction (Olaya 2009). Even if the aspect is a circular variable, for sake of simplicity we treat it as a normal variable in the range  $-180^\circ, +180^\circ$ .

The overall (local) curvature ( $C$ ) is defined as the two-dimensional Laplacian  $C = \nabla^2 z(x,y)$ :

$$C = \frac{\partial^2 z}{\partial x^2} + \frac{\partial^2 z}{\partial y^2} \quad (3.6)$$

$C$  is positive when the surface is locally concave and negative when the surface is convex. A value of zero indicates that the surface is locally flat. Peaks have negative values of curvature. Pits have positive values of curvature. A curvature map can be used for identifying lineaments on a DEM because it highlights rapid changes at the base and the top of a slope: concave at the base and convex at the summit (Smith and Clark 2005). When this is calculated across a region, breaks of slope and ridges are well identifiable. For example, the curvature map in Fig. 3.3b allows easy identification of the scoria cone crater rim and base as well lava channel levees and beds. Fig. 3.3e shows an example of the multi-curvature ( $MC$ ) parameter calculated as the average curvature at various scales.  $MC$  retains the same informative content as  $C$ , but enhances details and the readability of the general topography.

### 3.2.3 Topographic position index (TPI) and deviation from mean elevation (DEV) index

Among the various algorithms used to classify landforms (see Hengl and Reuter 2008 for details), the topographic position index ( $TPI$ ) has become very popular, partly due to its implementation in widespread GIS software.  $TPI$  is defined as the difference between the elevation  $z$  at a certain point

and the average elevation  $\bar{z}_R$  around it within a predetermined radius  $R$  (Wilson and Gallant 2000; Reu et al., 2013):

$$TPI = z - \bar{z}_R \quad (3.7)$$

$TPI$  (Fig. 3.3c) is a scale-dependent parameter and is used to highlight landscape units such as ridges and valleys on the scale defined by the radius  $R$ . Positive  $TPI$  values represent locations that are higher than the average of their surroundings, as defined by the neighborhood (e.g. ridges and peaks, etc.). Negative  $TPI$  values represent locations that are lower than their surroundings (e.g. valleys and pits). For planar areas, either horizontal or sloping,  $TPI$  is zero.

Deviation from mean elevation ( $DEV$ ) index is derived by dividing  $TPI$  by the standard deviation  $SD_R$  of the elevations within the radius  $R$  (Wilson and Gallant 2000; Reu et al., 2013):

$$DEV = \frac{z - \bar{z}_R}{SD_R} \quad (8)$$

$DEV$  (Fig. 3f) index measures the local deviation from the mean elevation and, like  $TPI$ , is positive when a point is situated higher than its neighborhood and negative when it is situated lower, but it is mostly restricted to values between  $-1$  and  $+1$  because of its normalization. Values outside this range often indicate anomalies in the DEM.  $TPI$  and  $DEV$  are widely used for automatic and semi-automatic landform classification.

### 3.2.4 Roughness maps

Surface roughness is an important morphological variable that measures the variability in elevation of a topographic surface at a given scale. The scale of analysis is determined by the size of the landforms of interest. Several different parameters can be used to quantitatively model surface topographic roughness. One of the most commonly used parameters is the root mean square ( $RMS$ ) height around the mean i.e. the standard deviation of height (e.g. Shepard et al., 2001).

In this work,  $RMS$  roughness is calculated not around the mean value but as the  $RMS$  deviation around the interpolating plane (Mazzarini et al., 2008). For each pixel, we consider the local surface defined by a set of DEM points within a predetermined distance  $R$ . Then we de-trend this surface by subtracting the interpolating plane. Finally, we compute the  $RMS$  height. By subtracting the interpolating plane the resulting roughness does not depend on the average local slope. This means

that the roughness of a plane is always zero, regardless of its inclination. Fig. 3.4a shows the *RMS* deviation roughness map for the test area.

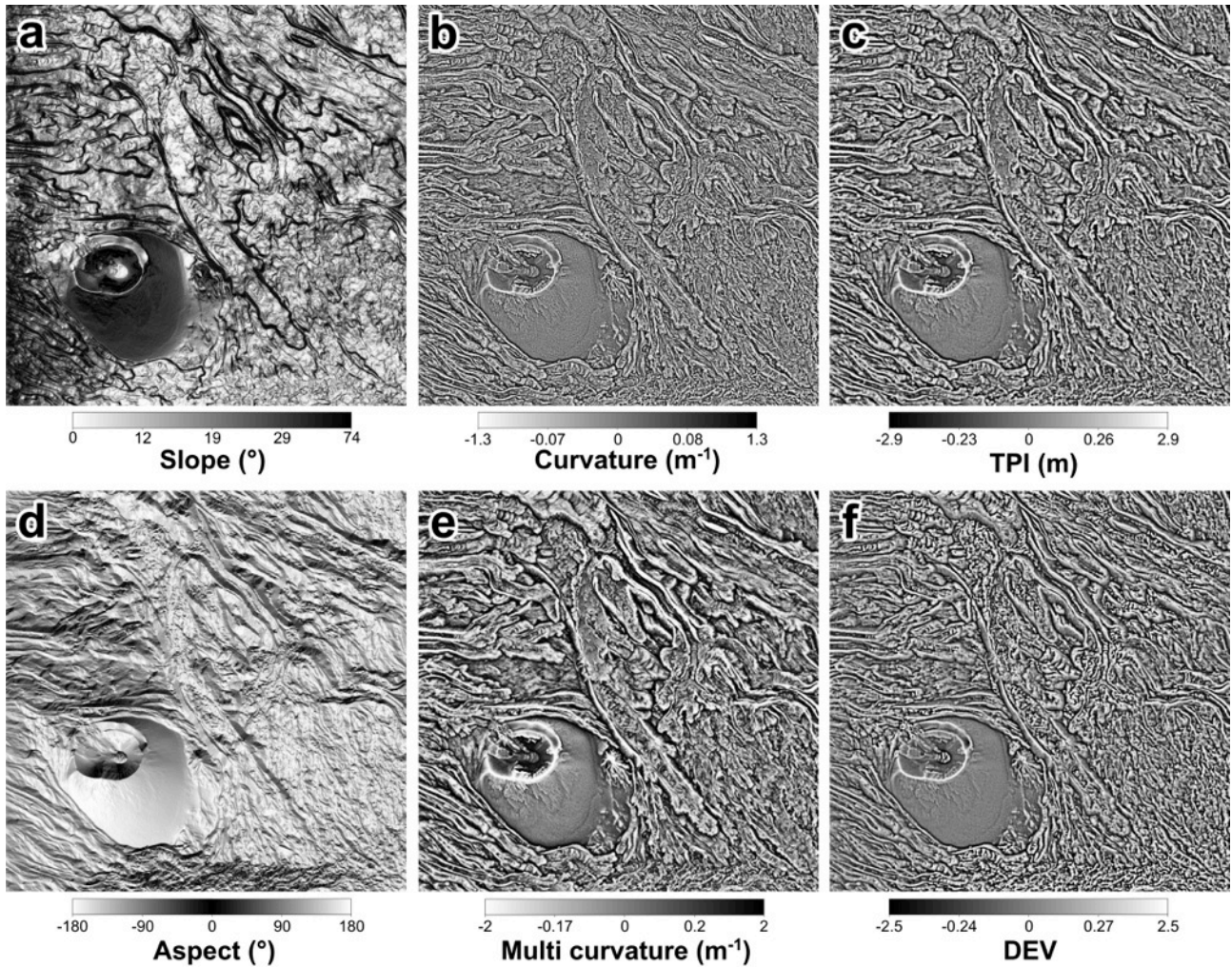


**Fig. 3.3** Slope, aspect, curvature, *TPI* and *DEV* maps of an area of 1200 m × 1200 m on Mt. Etna. The simple curvature map is calculated at a length scale of 3 m, i.e. with a moving window of 3 × 3 pixels = 3 m × 3 m. The multi curvature example was obtained as the arithmetic average of the curvatures calculated at length scales of 3, 6, 12, 25, 50, and 100 m. *TPI* and *DEV* were calculated within a radius of 5 m.

An alternative approach for computing surface roughness utilizes a different way of measuring the variability in slope and aspect of local patches of a DEM (e.g. Hobson 1972; Woodcock 1977; McKean and Roering 2004). Let's take the surface-normal unit vectors in an  $n \times n$  cells sampling window (Fig. 3.4c). For smooth topography these vectors have coherent orientations while for rough topography their orientations are characterized by a large degree of dispersion. The sums of the cross products of the direction cosines of the surface-normal unit vectors can be organized in a 3 × 3 orientation matrix  $T$  (Fara and Scheidegger 1963; Woodcock 1977):

$$T = \begin{pmatrix} \sum x_i^2 & \sum x_i y_i & \sum x_i z_i \\ \sum x_i y_i & \sum y_i^2 & \sum y_i z_i \\ \sum x_i z_i & \sum y_i z_i & \sum z_i^2 \end{pmatrix} \quad (3.9)$$

where  $(x_i, y_i, z_i)$  are the components of the  $N$  unit vectors. After calculating the three eigenvalues of this matrix they are ordered from the largest to the smallest,  $\lambda_1 \geq \lambda_2 \geq \lambda_3$ . Since the sum of the eigenvalues is equal to  $N$ , the normalized quantities  $S_i = \lambda_i/N$ , so that  $S_1+S_2+S_3 = 1$ , can be defined. Because of the normalization, there are only two independent quantities  $S_i$ .  $S_i$  describes the amount and nature of clustering of the vector orientations: the ratio  $S_1/S_2$  is defined as flatness and the ratio  $S_2/S_3$  is called organization (Coblentz and Karlstrom 2011). These ratio values are often not normally distributed, hence it is more convenient to use their logarithms (Fig. 3.4c, d). The ratio of  $\ln(S_1/S_2)$  to  $\ln(S_2/S_3)$  was defined as the  $K$ -value by Woodcock (1977) and can be used to evaluate the clustering of the normal vector distribution.

Hobson (1972) measured the surface roughness as  $1/N$  times the length of the vector sum of all the unit vectors in the moving window of Fig. 3.4c:

$$R = \frac{1}{N} \sqrt{\left(\sum x_i\right)^2 + \left(\sum y_i\right)^2 + \left(\sum z_i\right)^2} \quad (3.10)$$

where  $(x_i, y_i, z_i)$  are again the components of the  $N$  unit vectors. If the surface is perfectly flat the vector sum is a vector with a length equal to  $N$  so that  $R = 1$ . The rougher the surface, the lower the length of the vector sum (Fig. 3.4d). The unconsolidated deposits of a scoria cone, most of which are cinder-sized, have low roughness, while lava channels have high roughness (Fig. 3.4).

### 3.2.5 Sky view factor

Preferential directions due to the lighting in hill-shading (see Fig. 3.2) can be also avoided by using uniform diffuse illumination instead of point light sources. Supposing that the entire celestial hemisphere is equally bright, the illumination of a given point on a DEM is proportional to the portion of the sky that is visible from the point itself. The portion of visible sky is a measurable physical quantity (Fig. 3.5) and is called Sky View Factor ( $SVF$ ; Steyn 1980).  $SVF$  is given by the ratio of the solid angle of the visible sky ( $\Omega_{\text{sky}}$ ) to the solid angle of the illuminating hemisphere ( $= 2\pi$ ):

$$SVF = \frac{\Omega_{\text{sky}}}{2\pi} \quad (3.11)$$

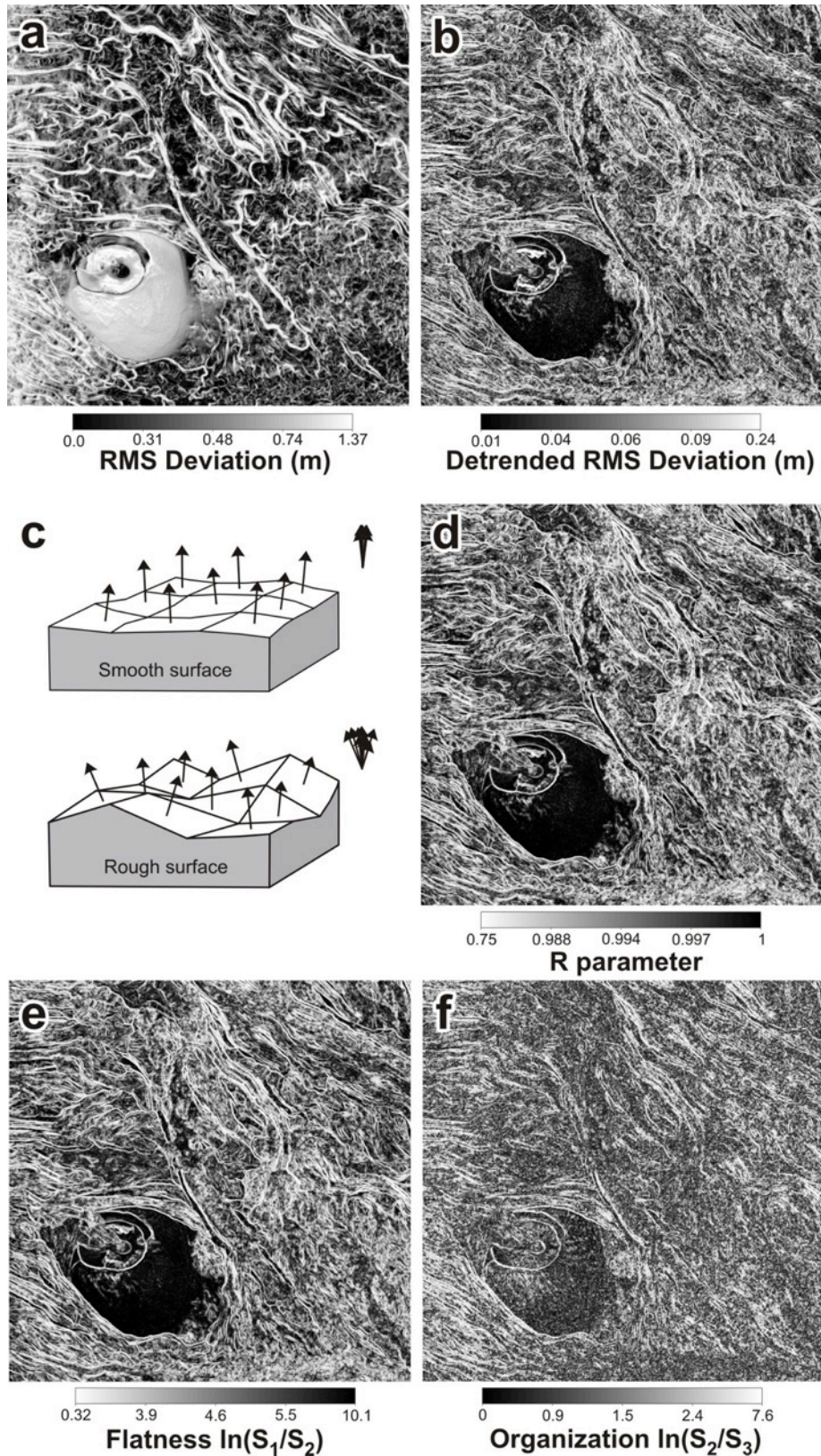


**Fig. 3.4** Roughness maps for an area of 1200 m  $\times$  1200 m on Mt. Etna. a and b) The *RMS* Deviation (detrended and not) was calculated as explained in the main text with a radius of 2 m. c) Topographic surface roughness evidenced by unit normal vectors: smooth surfaces have coherent orientations, whereas rough surfaces have a large degree of dispersion (modified from Coblenz and Karlstrom, 2011). d) *R* parameter, e) flatness  $\ln(S_1/S_2)$  and f) organization  $\ln(S_2/S_3)$  were calculated as explained in the main text with a sampling window of  $5 \times 5$  cells = 5 m  $\times$  5 m.

The end members  $SVF = 0$  and  $SVF = 1$  mean that no portion of the hemisphere and the entire hemisphere are visible from the taken point, respectively. Calculating  $SVF$  at each point of a DEM is very CPU consuming. Therefore the first step to speed up calculations is to introduce a maximum search radius  $R$  within which possible obstacles that may mask portions of the sky are considered. Then,  $SVF$  is usually approximated by considering the “openness” to the sky along a number of directions ( $n$ ) instead of doing the complete calculation (Fig. 3.5 and Zakšek et al., 2011):

$$SVF = 1 - \frac{1}{n} \sum_{i=1}^n \sin \gamma_i \quad (3.12)$$

where  $\gamma_i$  is the elevation angle of the visible horizon. In Eq. 3.12  $\gamma_i$  cannot be negative to limit the estimation of each elevation angle by the mathematical horizon (Zakšek et al., 2011). If we allow  $\gamma_i$  to take negative values in Eq. 3.12, we obtain a new quantity that can reach a maximum possible value of 2 (here called  $SVF2$ ).

Uniform diffuse sky illumination of  $SVF$  and  $SVF2$  not only solves the problems of feature orientation but also enhances the perception of the relative height of surface elements (Fig. 3.6a, b). In general  $SVF$  and  $SVF2$  display very similar behavior, although they have significantly different values along sloping planes. This difference can be appreciated by comparing the flanks of the scoria cone in Fig. 3.6a and 3.6b.

$SVF$  only deals with the ridges of the topography. To introduce a similar quantity that deals with the depressions, first we mirror our surface  $z=f(x,y)$  across a horizontal plane obtaining a new surface  $z=g(x,y)$  with  $g(x,y) = -f(x,y)$ . Then we calculate the  $SVF$  of this inverted surface  $z=g(x,y)$  and we call this new quantity “mirrored  $SVF$ ” (Fig. 3.6c).  $SVF$  takes high values on crests and ridges while the “mirrored  $SVF$ ” takes high values inside valleys, gullies and craters (Fig. 3.6a, c).

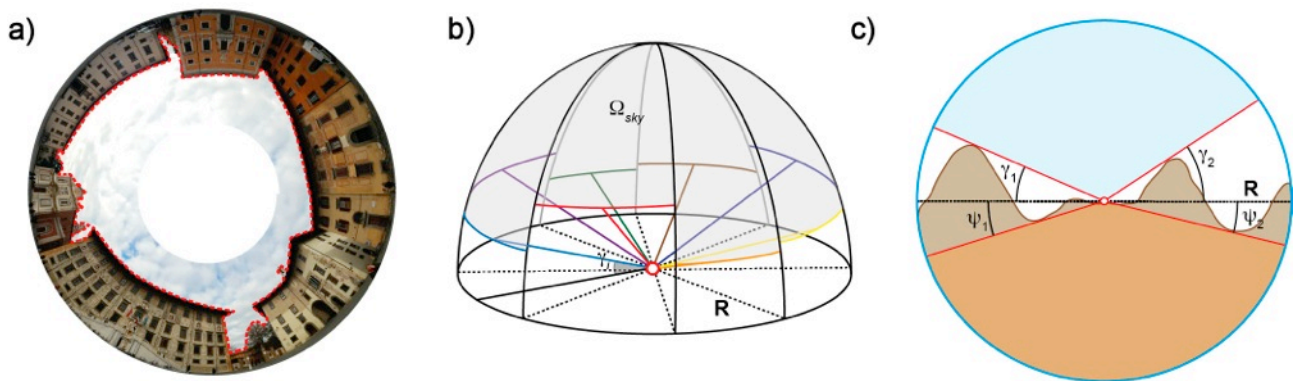


**Fig. 3.5** The  $SVF$  is defined by the ratio of the solid angle ( $\Omega_{sky}$ ) of the visible sky above a certain observation point (dotted line in frame a). In frame a, the observation point is the middle of Piazza dei Cavalieri (Pisa, Italy) and the

dotted line defines the border of the visible sky. In order to minimize the computing resources required, the *SVF* is calculated by computing the vertical elevation angle of the horizon  $\gamma_i$  in  $n$  directions ( $n=8$  in frame b), limited to a specified radius  $R$ . In frame c, we show, for a given transversal section of the sphere, the definition of the  $\gamma_i$  and  $\psi_i$  angles used for the calculation of *SVF*, *SFV2*, mirrored *SVF*, openness, and openness up and down (after Zakšek et al., 2011).

### 3.2.6 Openness maps

Yokoyama et al., (2002) introduced two parameters called positive and negative openness. The positive openness is defined as:

$$\Phi_R = \frac{1}{n} \sum_{i=1}^n \phi_i = 90^\circ - \frac{1}{n} \sum_{i=1}^n \gamma_i \quad (3.13)$$

where  $\phi_i$  is the zenith angle along the  $i$ -th direction and  $\gamma_i$  are defined as in Eq. 3.12 but here are not limited to be positive (Fig. 3.5). The subscript  $R$  refers to the maximum horizontal search radius considered. Similarly the negative openness is defined as:

$$\Psi_R = 90^\circ - \frac{1}{n} \sum_{i=1}^n \psi_i \quad (14)$$

where  $\psi_i$  is defined in Fig. 3.5c. Both positive (or openness up) and negative (or openness down) openness always take positive values. The former measures the “openness of the terrain to the sky” while the latter is the “below-ground” openness (Yokoyama et al., 2002). The positive openness takes high values on crests and ridges; the negative openness takes high values inside valleys, gullies and craters (Fig. 3.6e, f).

Later Chiba et al., (2008) introduced a new parameter, generically called mere “openness”, combined from the positive and negative openness as:

$$Openness = \frac{1}{2} (\Phi_R - \Psi_R) \quad (15)$$

The openness is dependent on the chosen search radius  $R$  and is positive when the surface, at the scale  $R$ , is upwardly convex (i.e. crests and ridges) and negative when the surface is upwardly concave (i.e. in valleys, gullies and craters; Fig. 3.6d).

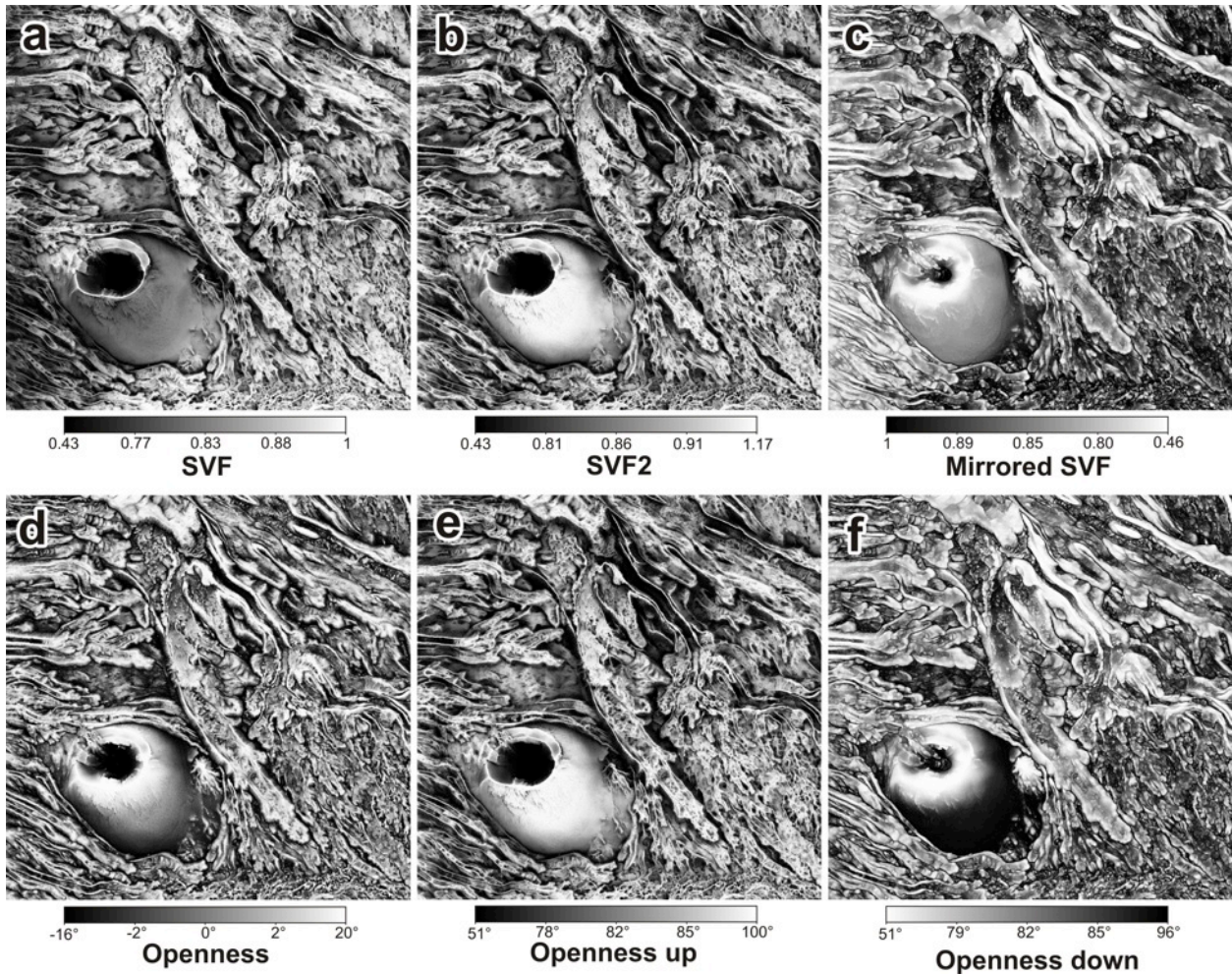


**Fig. 3.6** Sky view factor (*SVF*) and openness maps for an area of 1200 m × 1200 m on Mt. Etna. *SVF*, *SVF2* and mirrored *SVF* were computed using Eq. 3.12 (see main text for details). Mirrored *SVF* refers to the *SVF* of the DEM with opposite elevations values; openness up, openness down and openness were computed using Eqs. 3.13, 3.14 and 3.15, respectively. All calculations were performed along 8 search directions with a search radius of 100 m.

### 3.3 Image combination

Image combination may be defined as the combination of two or more images representing different parameters. The aim is to obtain a new colored hybrid image containing and representing more information than the individual original images (Fig. 3.7). Generically, image composition improves the image quality by enhancing the investigated details during the visual analysis. Image composition can be obtained following various techniques.

Widespread and useful maps derived using image composition are, for example, colored layer draped on hill-shaded images, which are often created with geographic information systems (GIS) using the Hue–Saturation–Value (HSV) color model. HSV is a common cylindrical-coordinate representation of points in an RGB color mode where *H* is hue, *S* is saturation, and *V* is value. The

hue of a generic point in the color space is its pure color; for example, all tints, tones and shades of red have the same hue. The saturation defines how pure a color is by giving its degree of degradation into gray tones: a pure color has a 100% saturation, and 0% saturation means that the color has completely lost its “color” and is only a shade of gray. The value, also called lightness, defines how dark a color is: a pure color has a 100% value and a value of 0 is black.

The most basic image composition for enhancing topographic details is overlaying a colored thematic map (the hue dimension in the HSV space) to a hill-shaded map (that is the SV color space dimensions). For example, a map color-coded according to pixels’ elevations or color-coded according to the thickness of a new emplaced lava flow can be overlaid to a hill-shaded map as shown in [Fig. 3.7a](#).

Using HSV color fusion technique, Chiba et al., (2008) developed the “Red Relief Image Map” (RRIM). They fix the hue to be red, thus producing a red image by adjusting the saturation value of red based on the topographic slope and its lightness (or value) based on the openness ([Fig. 3.7b](#) and [7c](#)). It accentuates the three-dimensional topography on a single image, where the openness value virtually performs an illumination role, and saturation of red color describes the steepness of topography. Karátson et al., (2016) used the RRIM for visualizing at the same time slope, concavity and convexity from the DEM of Gran Canaria Island. The authors chose RRIM because it effectively represents fine geomorphic features even on a largely flat surface and used it for successfully extracting planèzes and quasi-planar surfaces.

The reason for the use of red color in the RRIM is that it proved empirically to have the richest tone for human eyes, although other colors can also be applied (Chiba et al., 2008). A generic map can also be used to assign different hues to every pixel according to the thematic map values. [Fig. 3.7d](#) shows an example of RRIM in which hues are assigned as a function of the thickness of lava flows emplaced between 2005 and 2007.

“RRIM style” maps (that is more generic HSV compositions) can be produced by changing the starting maps used by Chiba et al. (2008). In order to best exploit the potential of RRIM it would be wise to use starting maps bearing completely different information. For example, in [Fig. 3.7e](#) the *S/F2* and slope are used as saturation and value respectively. Although *S/F2* and openness maps are very similar (compare [Fig. 3.6b](#) with [Fig. 3.6d](#)), swapping *S/F2* with the slope in the “RRIM style” image completely changes the visual effect of the composition.

Beside manipulations in the HSV color space, other image compositions can be used. For example, in [Fig. 3.7f](#) we enhanced the slope by adding the roughness (a de-trended *RMS* deviation in this case). In this new map the areas with rapid changes in slope (which have high roughness) are very bright and very accurately delimit areas with similar values of slope. As a result, this map emphasizes, for example, the external levee walls of lava flows.

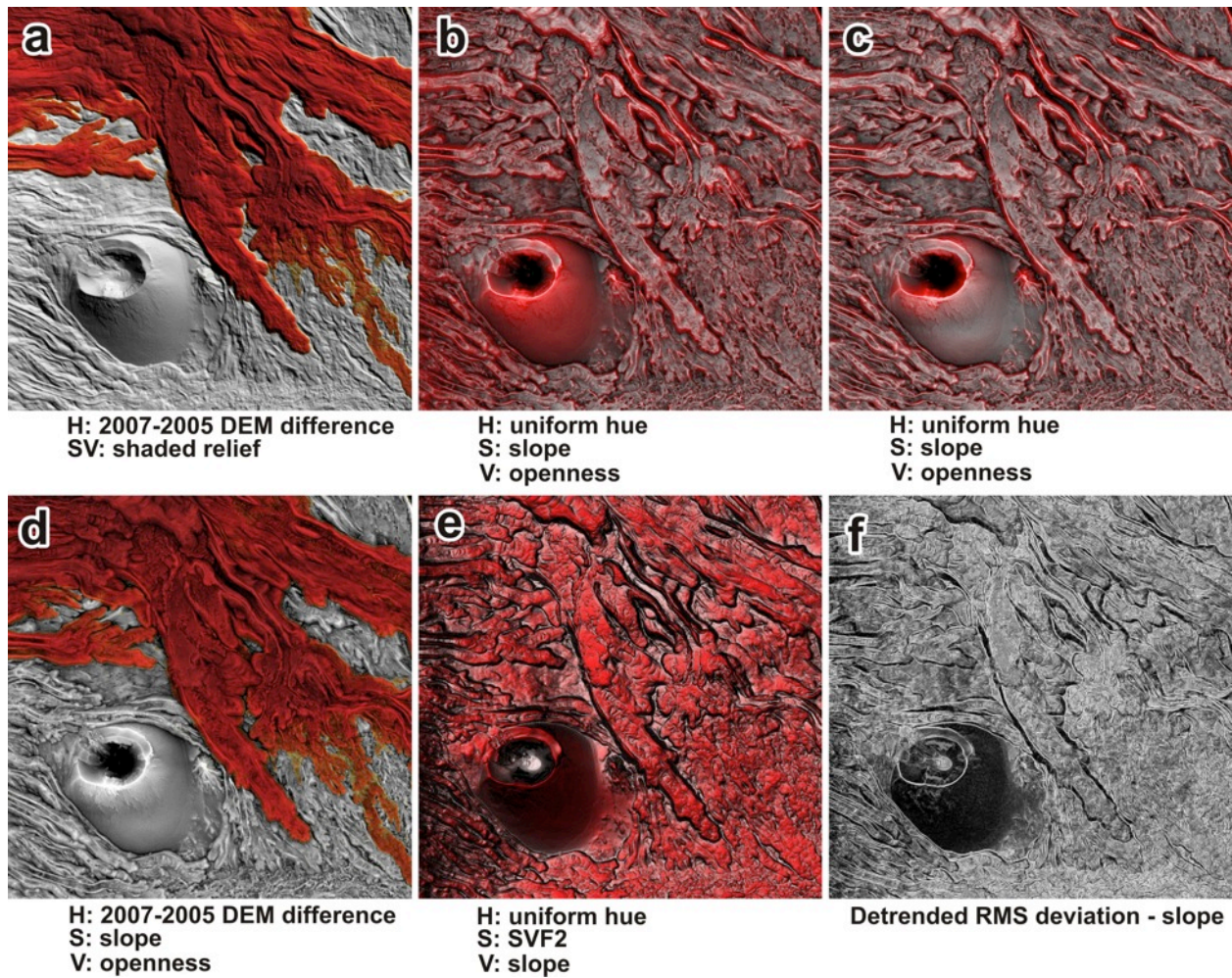


**Fig. 3.7** Examples of map composition for an area of 1200 m  $\times$  1200 m on Mt. Etna. When applicable the map layers used for each channel of the HSV space is specified under the image. a) Standard colored thickness map overlaid onto a hill-shaded map. b) RRIM c) RRIM of *TPI* calculated within a radius of 120 m. d) RRIM with hues assigned according to the thickness of the lava flow emplaced in the period 2005-2007. e) HSV composition with *SVF2* as saturation and slope as value. f) Image composition obtained applying a  $2.5 \sigma$  histogram stretching to the difference between the detrended *RMS* deviation and the slope grids. For maps b) to e) the HSV composition is done using as input image layers with a  $2.5 \sigma$  histogram stretching.

### 3.4 Surface parameter comparison

Surface parameters are, in many cases, correlated with one another. For example, a hill-shaded map with  $90^\circ$  of sun elevation angle and a slope map are very similar (cf. Figs. 3.2f and 3.3a), as well as curvature maps and *TPI* and *DEV* maps (cf. Fig. 3.3b, c and f), and *SVF* maps and openness up maps (cf. Fig. 3.6b and e). Taking into account that the amount of data can be very large, knowing *a priori* how to use the computing resources is very useful for minimizing computing time.

Distinguishing between correlated and uncorrelated parameters allows the operator to choose which maps should be produced from a DEM and which are instead unnecessary.

In this section, we compare surface parameters with one another by creating a correlation matrix.

Given two grids,  $A$  and  $B$ , we use the covariance between them to measure how similarly the two grids vary in space:

$$COV(A, B) = \frac{1}{n-1} \sum_{i,j} (a_{ij} - \bar{a})(b_{ij} - \bar{b}) \quad (3.16)$$

where  $a_{ij}$  and  $b_{ij}$  are the grid values of  $A$  and  $B$ , respectively, in the cell of position  $i,j$ . The sum on  $i,j$  spans all  $n$  cells of the grids. A positive value of the covariance means that the two grids tend to have a similar behavior: greater values of the first grid mainly correspond to greater values of the second, etc. On the other hand, a negative value of the covariance means that the two grids tend to have opposite behavior: greater values of the first grid mainly correspond to smaller values of the second grid and *vice versa*.

The magnitude of the covariance depends on the variability of both grids. For this reason we prefer to normalize the covariance by dividing it by the product of the corrected standard deviations of the two grids,  $S_A$  and  $S_B$ :

$$S_A = \sqrt{\frac{1}{n-1} \sum_{i,j} (a_{ij} - \bar{a})^2} \quad \text{and} \quad S_B = \sqrt{\frac{1}{n-1} \sum_{i,j} (b_{ij} - \bar{b})^2} \quad (3.17)$$

to obtain a normalized version of the covariance better known as the correlation coefficient:

$$COR(A, B) = \frac{COV(A, B)}{S_A S_B} = \frac{\sum_{i,j} (a_{ij} - \bar{a})(b_{ij} - \bar{b})}{\sqrt{\sum_{i,j} (a_{ij} - \bar{a})^2 \sum_{i,j} (b_{ij} - \bar{b})^2}} \quad (3.18)$$

The correlation coefficient ranges between -1 and +1. A correlation of +1 means that there is a perfect direct linear relationship between the two grids and a correlation of -1 means that there is a perfect negative linear relationship between the two grids. In any case, for both +1 or -1 correlations, the two quantities are in a perfect linear relationship.

Since for practical comparison we are more interested in the magnitude of correlation rather than the sign, we prefer to consider squared correlation values, so a value of 1 means that the two grids are perfectly correlated either directly or inversely. As the squared correlation approaches 0 (from

1), the two quantities are less and less correlated up to the point that for a value of 0 there is no correlation between the spatial trends of the values of the two grids.

Fig. 3.8 shows the squared correlation matrix among the reviewed parameters in the test case area described above. Fig. 3.9 shows the square correlation matrix among the reviewed parameters calculated for four different DEMs of four areas with heterogeneous topography: i) the 1-m LIDAR DEM test area of this work; ii) the 10-m resolution 2005 DEM of Etna region (Italy) produced by merging of a 1-m LIDAR DEM (Favalli et al., 2009) and TINITALY DEM (Tarquini et al., 2012a); iii) the 10-m resolution DEM of Tenerife Island (Canary Islands, Spain) produced by GRAFCAN (2009); and vi) the SRTM DEM (<http://www2.jpl.nasa.gov/srtm>), resampled to 120 m, of a region of the Blue Nile river basin (Ethiopia).

Figs. 3.8 and 3.9 show that the chosen DEMs provide very similar results that can be summarized as follows. Hill-shaded maps are not or poorly correlated with the other parameters. Only hill-shaded maps computed with a sun elevation angle of  $90^\circ$  are well correlated with slope maps and variously correlated with *SVF* maps. Hill-shaded maps computed from opposite azimuths contain very similar information. Slope is largely uncorrelated except for certain correlation with *SVF*. The curvature parameters are generally somewhat correlated with *SVF* and openness parameters. Roughness is uncorrelated with the curvature parameters and very poorly correlated with the hill-shading. Openness up is well correlated with *SVF* parameters, while openness down is not.

On the whole, in order to have the most uncorrelated content the following maps should be produced: various hillshading, slope, a curvature map, a *TPI* map with high R, 3 roughness maps, openness down, openness and one of a choice between *SVF*, *SVF2* and openness up. Uncorrelated parameters can be combined in order to obtain a more informative map.

In the following case studies, the surface parameters and their representations were chosen after taking into account the features we want to detect and avoiding redundant information.

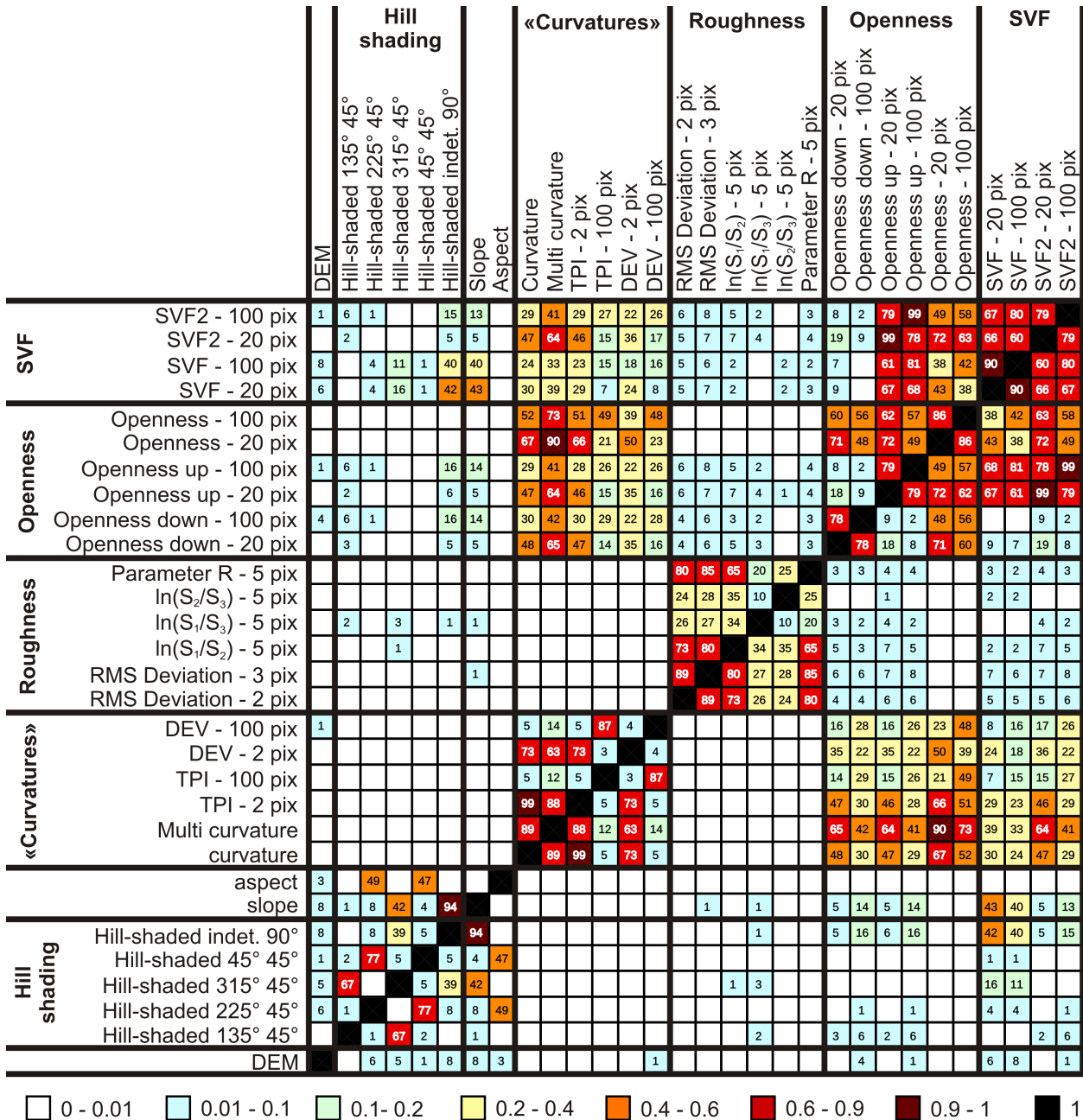
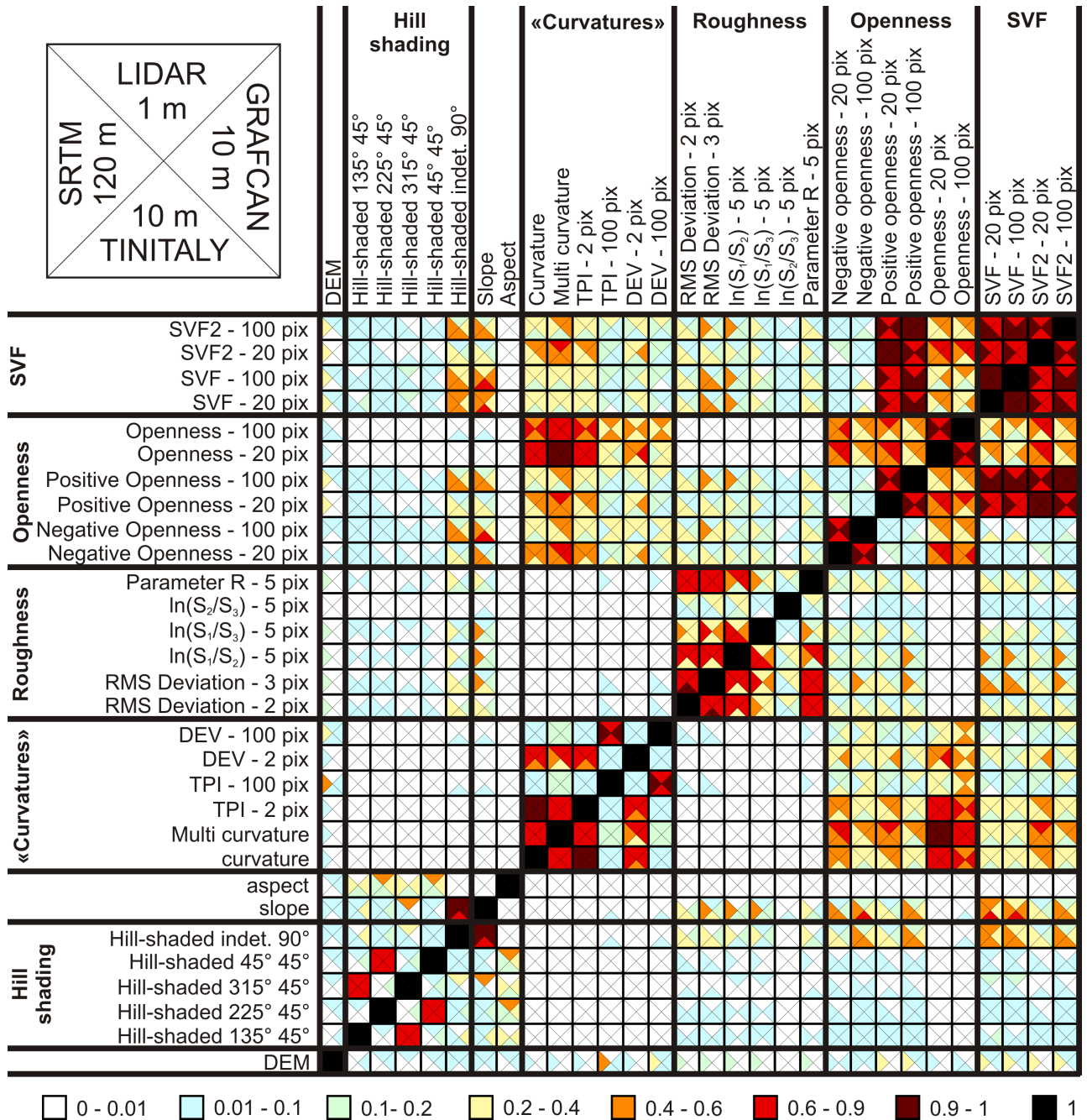


Fig. 3.8 Matrix of the squared correlations between the quantities illustrated in Figs. 3.2, 3.3, 3.4, and 3.6. The numbers inside the cells is the square correlation expressed as percentage. Length scale, when necessary, follows the quantity name and is reported in pixel units (pix; in this case 1 pix = 1 m). For the openness and SVF quantities the searching radius is reported. For the RMS deviations the radius of the neighborhood is reported and for the other roughness parameters the moving window linear dimension is reported: e.g. “parameter R – 5 pix” means that the parameter R has been calculated with a moving window 5x5 pixels.



**Fig. 3.9** Matrix of the squared correlations among the quantities considered in this paper. Each matrix element is split in four triangular sub-elements corresponding to different areas and DEMs. The upper sub-element refers to 1-m resolution LiDAR DEM of a portion of Mt. Etna. The lower sub-element refers to a 10-m resolution 2005 DEM of Etna region (Italy) produced by the merge of a 1-m LIDAR DEM (Favalli et al. 2009) and TINITALY DEM (Tarquini et al., 2012). The right sub-element refers to the 10-m resolution DEM of Tenerife Island (Canary Islands, Spain) produced by GRAFCAN (2009). The left sub-element refers to the SRTM DEM, resampled to 120 m, of a region of Ethiopia. Length scale, when necessary, follows the quantity name and is reported in pixel units. For the openness and SVF quantities the searching radius is reported. For the RMS deviations the radius of the neighborhood is reported and for the other roughness parameters the moving window linear dimension is reported: e.g. “parameter R – 5 pix” means that the parameter R has been calculated with a moving window 5×5 pixels.

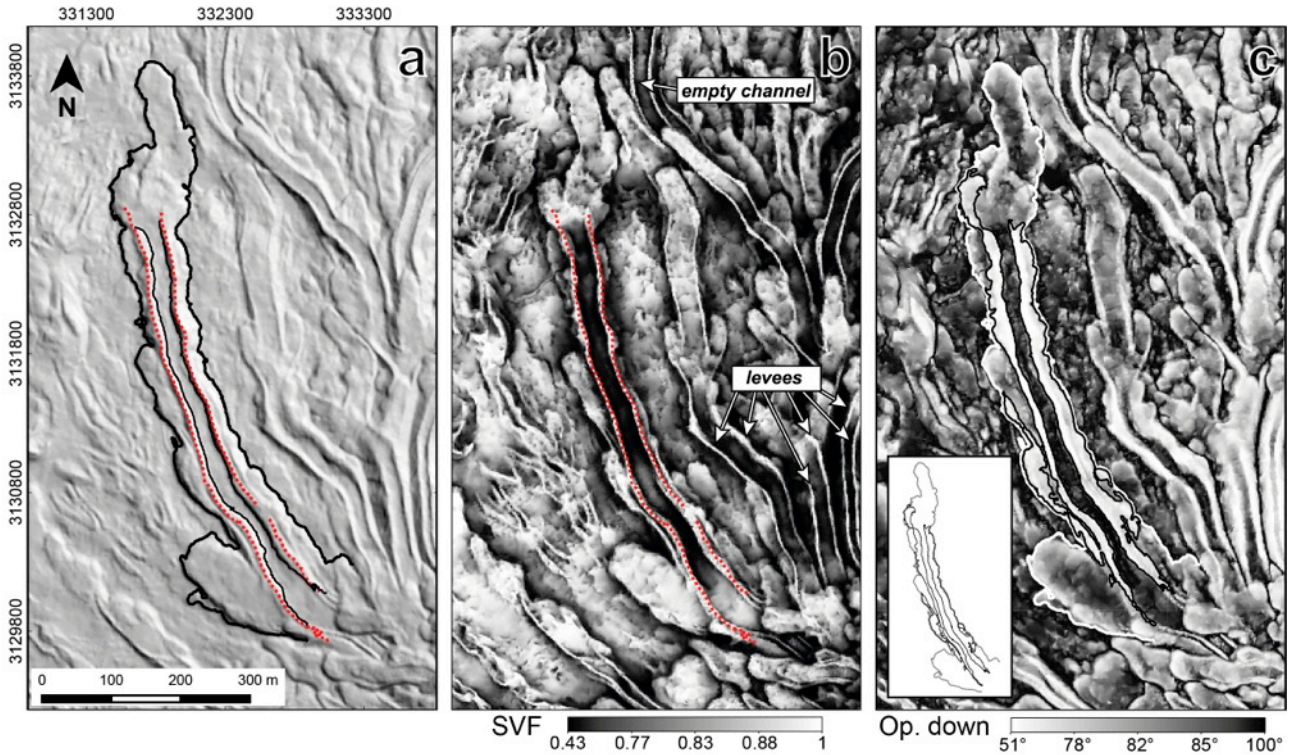
### 3.5 Case studies. Roques Blancos phonolitic lava flow

Fig. 3.10 shows hill-shaded, openness and *SVF* maps of a Roques Blancos phonolitic lava flow field, NW of the Pico Viejo stratocone (Tenerife Island). The Roques Blancos lava flow was erupted about 1714 BP from a dome located at an elevation of 2700 m a.s.l. (Carracedo et al., 2007).

The shaded relief (Fig 3.10a) shows a general topography composed of a complex system of ramified channels characterized by thick flows, steep fronts and conspicuous levees. However, channels running from NW to SE are not well visible because they are aligned with the illumination direction. Already Smith and Clark (2005) made analyst aware that the use of a directional light source introduce bias especially in case of linear landforms. It is quite obvious that this problem is particular relevant in mapping lava flow. All linear features are instead clearly visible in both *SVF* and openness down images (Fig 3.10b and c), which allow untangling this complex system of channels. The *SVF* map depicts the empty channel in distinct dark tones, which makes them easily identifiable and the levee ridges are outlined as bright lines and can therefore be easily mapped (Fig. 3.10a, b, dashed lines). The openness down map reveals additional important information: while the rims of levees are less pronounced, their deepest parts are clearly marked. Also, the lobate forms of the lava front, composed by curved superimposed layers, are properly visualized. Finally, the openness down map gives a clear idea of the considerable thickness of these phonolitic lavas.

These maps can be used for extracting the interesting features in a semi-automatic way. From a practical point of view, even if the *SVF* fruitfully identifies the levee rims, their automatic extraction using this map is troublesome and indeed it is much more simply performed by extracting these lines as portions of contour lines of the hill-shaded map of Fig. 3.10a. In fact the levee rims identify the points where the shading changes from low to high values (opposite sides of the levee). Similarly, by choosing the proper value of openness down, the contour line of the lava flow can be extracted and used for calculating the lava extension, length and volume. The same procedure can be done for extracting the edge of the channel bed. In the example of Fig. 3.10c, the values of  $86^\circ$  and  $81.5^\circ$  for the openness down map can be used for automatically delineating the isolines that best delimit the base of the lava and the bed of the channel, respectively.

After very minor editing operations, consisting mainly of cutting out unwanted part of the isolines, the shapefiles of the base and the bed of the lava channel are extracted (Fig. 3.10).



**Fig. 3.10** Extraction of the main features from a lava channel belonging to the Roques Blancos lava flow (Tenerife Island). a) Hillshaded map with lines defining the base of the lava (external continuous line), the levees (dotted lines) and the base of the channel (internal continuous lines) extracted in a semi-automatic way from the openness down and hillshaded maps. b) *SVF* map which allows identification, with great accuracy, of the channel levees and the features inside them. c) Openness down map which can be used to distinguish among different lava flows because it highlights the particular slope breaks occurring between a lava flow and the substrate. For the same reason it highlights the contacts between internal levees and the base of the channel. Also in this case, with appropriate values used, the base of the lava (white line in the figure and gray in the inset) and the internal channel (black lines in the figure and inset) can be semi-automatically extracted.

### 3.6. Discussion

The growth of new remote sensing technologies capable of producing topographic data with high accuracy at reasonable costs, and the availability of web-shared DEMs, offer great opportunities to better map and quantify features in volcanic areas. In order to make the best use of the great availability of these large amounts of data it is necessary to know what information can be extracted from a DEM and how to effectively use the computing resources.

The most used DEM representation for mapping and measuring volcanic features is the shaded relief map. It is very informative and provides an immediate picture of the 3D distribution of landforms. Hill-shading maps generated using an oblique illumination with a light source shining from a moderate angle between the horizon and zenith, and from the northwest, provide the most

intuitive images of the shape of the terrain. An active shadow would give a more realistic representation of the terrain, but at the same time would cast shadow on some areas of the DEM preventing the visualization of any detail in such zones. The major drawback of using hill-shaded map the is done by the fact that the angle of illumination, or azimuth, strongly affects the way features appear. In other words in the hill-shaded map the perception of the convexity and concavity of surfaces depends on the relative position of the light source (Fig. 3.2). As a consequence, features with a certain orientation may be displayed in a different manner depending on the direction of illumination or, even worse, they can be in the shadow and not visible at all. In addition linear features, or otherwise features with a certain orientation, may be displayed in a different manner depending on the direction of illumination. For these reason, if only hill-shading maps are available, it is recommended to compare maps produced with different directions of illumination. For a Lambertian surface, hill-shading with an elevation angle of  $90^\circ$  yields a brightness proportional to the cosine of the local slope thus it is just a reclassification of a slope map (cf. Figs. 3.2f and Fig 3.3a).

Besides hill-shaded maps, the slope (Fig. 3.3a), the aspect (Fig 3.3d), the *SVF* (Fig 3.6a-c) and the openness (Fig 3.6d-f) as well as RRIM maps (Fig. 3.8) are enough to present and describe, by themselves, the topography and morphological characteristics. They all act like hill-shading so they can be used to visualize a DEM, although each of them highlights particular aspects of the relief. Slope maps and vertically illuminated hill-shaded models are, by properly adjusting the contrast, very similar or identical. Both of them eliminate the azimuth biases typical of obliquely illuminated single-point-source hill-shading. It follows that slope maps can be used instead of hill-shaded maps to overcome some drawbacks. The aspect map, with appropriate gray scale color legend, is very similar to a hill-shaded map (e.g. Fig. 3.3d); the legend can be easily changed in order to mimic a different azimuthal direction of illumination. The *SVF* maps are actually just a different kind of hill-shading with a uniform diffuse illumination (Fig. 3.5) and the openness up maps are very similar in construction to the *SVF* maps and then by definition very similar to *SVF*, that is in the limit of small angles. In particular, it is evident that openness up and *SVF2* produce very similar maps when we convert the grids into images (cfr. Figs. 3.6b and 3.6e). This is because in the approximation of small angles results in  $\sin(\gamma_i) = \gamma_i$  (with angles expressed in radians). As a consequence the openness up and *SVF2* maps only differ in areas where we have big angles  $\gamma_i$ . For example, the test area in Fig. 3.6, which contains several steep structures and has a very high roughness (see Fig. 3.4), has an average openness up angle of  $81^\circ$  so that the average  $\gamma_i$  value is  $9^\circ$ , that is 0.1571 in radians, while its sine is 0.1564 and so, on average,  $\gamma_i$  and  $\sin \gamma_i$  differ only by 0.4 %. *SVF* differs from *SVF2* (and thus also from openness up) mainly on ridges and on slopes with horizontal dimensions greater than the search radius  $R$  (e.g. the slopes of the scoria cone in Fig. 3.6a, b and e). Analogously the

mirrored *SVF* and the openness down mainly differ in the pits and valleys and again on slopes with horizontal dimensions greater than  $R$  (cfr. Fig. 3.6c and 3.6f).

The curvature (Fig. 3.3b) looks like an edge detection filter (as it actually is). The multi-curvature map (Fig. 3.3f), collecting contributions of curvatures at very different length scales, provides an alternative way to put in evidence the various shapes; it looks more like a morphological filter and is very well correlated with openness. *TPI* and *DEV* are very similar and not visually very expressive (Fig. 3.3c, f). They are generally used for automatic classification of land features. The roughness map describes how complex the terrain is and so, it is a standalone and crucial parameter.

Color images are important because human eyes are sensitive to thousands of color shades which helps us in object identification. In addition, a color image can be composed by different grey-tone images, with each of them retaining different information. In the authors' opinion the best single image technique that is devoid of azimuth-bias and yet portrays the landscape optimally is, so far, the Red Relief Image map introduced by Chiba et al., (2008). It does not have a preferential direction (unlike classical hillshading) and, moreover, it is more readable if compared to images composed using *SVF* or openness up, where local depressions are in the dark and much data is missing. On the other hand, ridges are much better defined and identified using *SVF* or openness up, and valleys and depressions by using openness down or inverted *SVF*.

By simply analyzing the visual representation of parameters described above, it is clear that many of them contain almost the same information or that they are practically the same map. The correlation matrices (Fig. 3.8 and 3.9) produced in this work were obtained by calculating the correlation coefficient among each couple of analyzed parameters for four DEMs with various sources and resolutions. These matrices are a useful starting point for defining which parameter combinations can provide key information of the terrain and which of them are instead redundant. In the same way, the correlation matrix can be used to aid in the choice of map combinations for possible HSV colored maps. It is indeed obvious that to create an HSV map starting from images containing the same information is pointless.

Some of the relevant information that can be extracted from the correlation matrix is described in the following. First, we should note that in general the correlation between parameters shows slightly to no changes when using DEMs from different sources and with different resolution. Sometimes these differences can be more relevant. This can be due to the difference in DEM resolution or to differences in the terrain characteristics. A DEM is the most uncorrelated map, but, of course, it cannot be visually analyzed without further elaborations. Hill-shading maps are widely uncorrelated with all the other parameters. Only hill-shaded maps calculated using a vertical illumination are correlated with the slope and, somehow, with *SVF* maps. It should be noticed that inside the "hill-shaded" group the correlation depends on the illumination angles; in particular hill-

shaded maps with opposite azimuthal angles of illumination are strongly correlated. Also, the aspect is basically uncorrelated with all the examined parameters, except for some correlation with the hill-shaded maps. This is consistent with the results obtained by Evans and Cox (1999) who inter-compared zero, first and second derivatives of elevation. In addition to the vertical illuminated hill-shading, the slope has some correlation only with the *SVF* maps, but this seems to be dependent on the DEM source. In agreement with Evans and Cox (1999), slope is poorly correlated with DEM and curvature. The “curvatures” group contains heterogeneous parameters. They have almost no correlation with any type of hillshading and with slope and aspect, as also showed by Evans and Cox (1999). In general, they have some correlation with the openness group (especially with multi-curvature) maps and, to a minor extent, with the *SVF* group. Curvature and multi-curvature are correlated with both openness up and down but there are some differences depending on the DEM source. As expected, *TPI* 2pix and curvature are highly correlated since they are calculated in almost the same way; on the contrary, *TPI* 100 pix and curvature are not correlated. *TPI* and *DEV* maps are correlated only if they are calculated over windows with the same size. Overall roughness parameters are only correlated with other roughness parameters. Openness up is well correlated with *SVF* maps, however, openness down is not. Openness 20 pix and multi-curvature are highly correlated. Inside the “openness” maps we notice that openness down is uncorrelated to openness up. Openness parameters are uncorrelated with hill-shading and roughness. *SVF* is somehow correlated with the slope. *SVF2* is independent on the slope but it is correlated with the curvature. In particular, *SVF2* with a searching radius of 20 pix is highly correlated with the multi-curvature.

The increasing availability of various DEMs at different resolutions and coverage has been giving new research opportunities for volcano geomorphology studies. Detecting and delineating features in volcanic areas can be everything but easy because of their extreme complexities: volcanic areas are characterized, for example, by the superimposing of lava flows, coalescent cones and volcanoes, huge ash fallout and, last but not least, if active, they are often dramatically changed by new eruptions. For this reason, it can be very useful to have informative maps which enhance specific volcanic landforms such as lava flow. For example, *SVF* and openness down images allow the complex system of channels of the Roques Blancos phonolitic lava flow to be untangled, enabling detection of levees, the base and the bed of the channels. These parameters can be used for performing a semi-automatic extraction of the main landform elements, helping to make the job of the analyst quick and precise.

---

## Chapter 4

---

### **LiDAR-derived morphometry of Etna's channel-fed lava flows**

The physical understanding of lava flow processes and emplacement dynamics is still largely studied and debated because it has relevant implications for hazard and risk management. Measurements of the geometry and morphology of lava features are crucial in understanding emplacement processes operating during effusive eruptions, since channel shape is assumed to be reminiscent of the process acting in the channel when it was active. Channel-fed lava flow morphometry is an expression of lava supply rate, rheology, heat loss, ground slope, plus a number of other parameters such as local topography. Of these, rheology is in turn affected by lava composition, temperature, crystallinity and vesicularity, all factors that are highly variable in space and time. Thus, temporal variations in lava supply rate or down-flow changes in cooling and rheology cause modifications in the resulting dimension and morphology of the channel and of the flow units that it feeds. Hence, channel morphometry allows us to explore the relationships between factors such as effusion rate, cooling rate, slope, flow emplacement dynamics and channel shape. Understanding these relationships is also essential for modeling and interpreting the dynamics of past effusive eruptions and for assessing the likely dynamics of future eruptions.

Accurate and precise measurements of lava-channel shape are not easy to perform. Firstly, a precision of tens of centimeters is required as part of a spatially detailed survey. Secondly, areas of several square kilometers need to be covered, with most lava channels that are difficult-to-impossible to access when active. The inefficiency of ground-based approaches can be solved by means of remote sensing technologies able to provide accurate and high-spatial resolution topographic data (Mazzarini et al., 2005; Harris et al., 2009; Favalli et al., 2010b; Tarquini et al., 2012b; Dietterich and Cashman 2014).

Insights into the dynamics of lava flow emplacement and determination of the main relations between volume flux, rheology, channel geometry and ensuing fluid dynamics have been gained through numerical and empirical modeling. The length of lava flows has been related to viscosity (Nichols 1939), eruption rate (Walker 1973), heat loss (Danes 1972) and erupted volume (Malin 1980). Lava flows have also been modeled as Bingham fluids (Park and Iversen 1984; Dragoni et al., 1986; Miyamoto and Sasaki 1997; Harris and Rowland 2001; Vicari et al., 2009). A number of interrelated factors are pivotal for determining the relations used in these models. Such factors include the erupted volume flux of lava (effusion rate), magma type, rheology, heat loss, cooling rate (and degree of thermal insulation), flow velocity, emplacement duration, slope and topography. However, the morphometric parameters of actual lava flows to be used as benchmark and/or initial and boundary conditions for lava flow modeling are still lacking in number and accuracy (Tarquini et al, 2012b; Lev and James, 2014). In particular, high spatial resolution pre-emplacement topography data, which allow accurate assessment of the role of underlying topography in the dynamics of lava flow and emplacement, are almost absent.

In Chapter 4 we use the high-resolution LiDAR-DEM of Mount Etna available at the INGV, Pisa Department, to extract a large number of very accurate morphometric parameters from eleven channel-fed lava flows. Morphometric analysis takes advantage of the actual high-resolution topography above which the lava flows, builds its shape and emplaces. Here, for the first time, we are providing large amounts of data about pre-emplacement slope without interpolating the pre-existing topography under the flow. The morphometric analysis of selected lava flows is conducted through a semi-automatic procedure that measures the parameters over DEMs and that implies the tracking of surface-specific elements such as flow axes and base, levee ridges and edges of the channel bed. Tracking is supported by the automatic detection of surface-specific points and is performed over the sky view factor maps and openness maps for a most effective DEM visualization. The morphometric parameters extracted include pre-emplacement slope, widths of flow, channel and channel base, as well as levee thickness and slope. Finally, these parameters are plotted together in order to investigate their mutual relationship.

#### **4.1 Channel-fed lava flow morphometry. An introduction**

From a morphological point of view, Lipman and Banks (1987) distinguished the following four down-flow segments (from the flow toe to the vent) along a channel-fed lava flow: (i) flow front, (ii) zone of dispersed flow, (iii) transitional channel zone, and (iv) stable channel (Fig. 4.1).

Although based on Mauna Loa's 1984 lava flow, this classification also appears to fit well for the Mount Etna lava flows (e.g., Kilburn and Guest 1993; Bailey et al. 2006). The lava front is the down flow limit of the flow. Immediately behind the flow front there is a zone of dispersed flow across which the movement is widespread and where a channel and static levee are lacking. Further up-flow, the transitional channel is marked by a distinct channel bounded by blocky or clinkery lava still capable of deforming and moving slowly (Lipman and Banks 1987). The boundary between the channel and the bounding lava is marked by shear ridges, so that shear-zone bounds marginal zones of stagnant lava, or levees began to form (Lipman and Banks 1987). Behind this, there is no marginal flow zone, and all the flow forming the levees is concentrated in a well-defined, stable, central channel, bound by broad zones of stationary lava (Lipman and Banks 1987).



**Figure 4.1** Orthophoto of a sector of Mount Etna's 1974 lava flow field overlaid on the shade relief derived from high resolution DEMs. The four down-flow segments described by Lipman and Banks (1987) are mapped.

From a morphometric point of view, any landform can be presented by universal elements or features (in GIS terms: polygons, lines and points), which can be recognised regardless of scale or type of terrain (Hengl and Evans 2009). A landform can be described in terms of surface-specific points and lines. Surface-specific points are local extreme points (local maxima and minima) on the terrain surface, such as peaks, pits, and passes. They may not only present their own elevation values but also provide more topographic information on their surroundings. The lines connecting certain surface-specific type points are referred to as feature-specific lines, for example ridge lines, course lines, break lines, and so on (Li et al., 2004). Surface-specific elements can be recognized on a lava flow and used to quantify its shape (Fig. 4.2).

The morphology of channel-fed lava flow can be quantified by extracting, from a DEM, several discrete 2D lava flow profiles normal to the flow direction (Mazzarini et al., 2005; Tarquini et al, 2012b; Deardorff and Cashman 2012; Chevrel et al., 2013; Dieterich and Cashman 2014). Properly spaced, these profiles allow the measurement of relevant morphometric parameters along the flow. Following Tarquini et al., (2012b), the morphometric parameters that are needed to quantitatively describe the lava flow morphology are: the widths of flow ( $W_{\text{flow}}$ ), channel ( $W_{\text{channel}}$ ) and channel bed ( $W_{\text{bed}}$ ); the heights of levees ( $H_{\text{DX}}$  and  $H_{\text{SX}}$ ); the local slope angle of the levees ( $\theta_{\text{levee}}$ ); and the pre-existing topography ( $\theta_{\text{pre}}$ ). Each of these parameters is recorded as function of the distance along the axis from the vent towards the front.

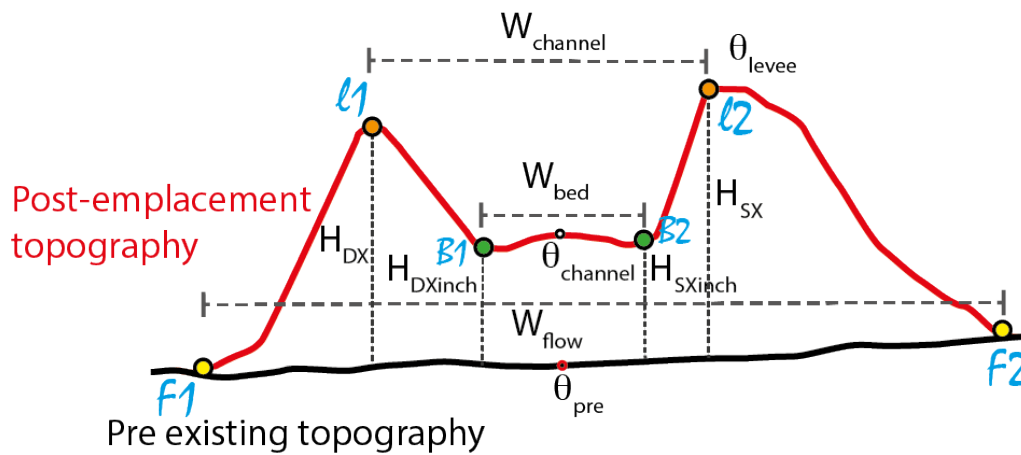


**Fig. 4.2** Conceptual scheme of the flow unit morphological elements and morphometric parameters measured by the morphometric tool:  $W_{\text{channel}}$  = channel width;  $W_{\text{bed}}$  = channel bed width;  $W_{\text{flow}}$  = flow width;  $\theta_{\text{pre}}$  = pre-existing local slope;  $\theta_{\text{channel}}$  = channel bed local slope;  $\theta_{\text{levee}}$  = average levee slope;  $H_{\text{DX}}$  = right levee thickness;  $H_{\text{SX}}$  left levee thickness. Left and right are identified with respect to flow direction.  $l_1$ ,  $l_2$ ,  $B_1$ ,  $B_2$ ,  $F_1$  and  $F_2$  are surface-specific points. Surface-specific lines connecting surface specific points, levee ridges, channel-base edges and flow base, respectively.

Table 4.1 shows the morphometric parameters measured in this work for the profile of each selected channel-fed lava flow. In an attempt to achieve the maximum amount of information from the analysed channels, we developed a morphometric tool to automatically extract the parameters listed in Table 4.1. This tool allows to process a large number of 2D profiles for each channel within the frame of a semi-automatic procedure described in the next section.

## 4.2 Method for extracting morphometric parameters from DEM

Morphometric analysis of selected channel-fed lava flows is performed using a C++ code developed *ad-hoc* for measuring, in one shot, and without assistance, all the parameters described in Table 4.1 over a DEM. The code required as mandatory inputs the post emplacement DEMs in regular gridded form, the line of the flow axis and the polygon delimiting the flow base. Optional inputs are the lines tracking levee crest and the lines delimiting the channel-bed and the pre-emplacement DEM. It should be noted that the availability of topography before the onset of an eruption does not guarantee *per se* the availability of pre-emplacement topography for every single channel of the lava field. Indeed, a given single channel could emplace on the previous flow emitted during the same eruption.

<b>L</b>	Distance along axis	$\theta_3$	Averaged $\theta$ (7 profiles)
<b>W<sub>flow</sub></b>	Total flow width	$\theta_4$	Averaged $\theta$ (9 profiles)
<b>W<sub>channel</sub></b>	Channel width	<b>Z<sub>f1</sub></b>	Right flow edge elevation
<b>W<sub>bed</sub></b>	Channel bed width	<b>Z<sub>f2</sub></b>	Left flow edge elevation
<b><math>\theta_{DX}</math></b>	Right levee slope	<b>Z<sub>l1</sub></b>	Right levee elevation
<b><math>\theta_{SX}</math></b>	Left levee slope	<b>Z<sub>l2</sub></b>	Left levee elevation
<b><math>\theta_{levee}</math></b>	Average levee slope	<b>Z<sub>B1</sub></b>	Right bed channel edge elevation
<b>H<sub>DX</sub></b>	Right levee thickness	<b>Z<sub>B2</sub></b>	Left bed channel edge elevation
<b>H<sub>SX</sub></b>	Left levee thickness	<b>X<sub>f1</sub></b>	Right edge axis distance
<b>H<sub>DXint</sub></b>	Interpolated right levee thickness	<b>X<sub>f2</sub></b>	Left edge axis distance
<b>H<sub>SXint</sub></b>	Interpolated left levee thickness	<b>X<sub>l1</sub></b>	Right flow levee axis distance
<b>H<sub>DXinch</sub></b>	Right bed thickness	<b>X<sub>l2</sub></b>	Left flow levee axis distance
<b>H<sub>SXinch</sub></b>	Left bed thickness	<b>X<sub>B1</sub></b>	Right channel bed edge axis distance
<b><math>\theta_1</math></b>	Averaged $\theta$ (3 profiles)	<b>X<sub>B2</sub></b>	Left channel bed edge axis distance
<b><math>\theta_2</math></b>	Averaged $\theta$ (5 profiles)		

**Table 4.1** Notation of all parameters. These parameters are represented in Fig. 4.2

In this work, the detailed identification and delineation of lava surface-specific elements (i.e. the lines passing through points  $l_i$ ,  $b_i$  and  $f_i$  for  $i=1 \dots n$  of Fig. 4.2) are performed by combining a visual analysis over proper DEM-derived surface parameters, as identified in Chapter 3, with an automatic tool able to detect feature-specific points on the 2D lava flow profiles (points  $l_i$ ,  $b_i$  and  $f_i$  for  $i=1 \dots n$  in Fig. 4.2). The preliminary step of this procedure was the identification of the suitable channels (Fig. 4.3a). The selection criteria include: i) detection of the lava flows imaged by a high-density cloud; ii) detection of the flow with well-defined levee channel; iii) detection of the flow easily distinguishable from the surrounding ground surface by an abrupt change in slope. Lava flows with

pre-existing DEMs were privileged, i.e. we first focussed on channels having a pre-eruption DEM and not emplaced above the lava emitted during the same eruption.

Having selected the flow, the next step consisted in manually tracing the axis of the flow unit. Once the axis had been traced, the base of the flow, the levees and the edges of the channel bed had to be traced. Since the subjective interpretation of morphological features is a significant source of uncertainty (Tarquini et al., 2012b), a semi-automatic tool aimed at helping the analyst detect the target features was created and used together with the *SVF* and openness down maps (see Chapter 3) to minimize the uncertainties.

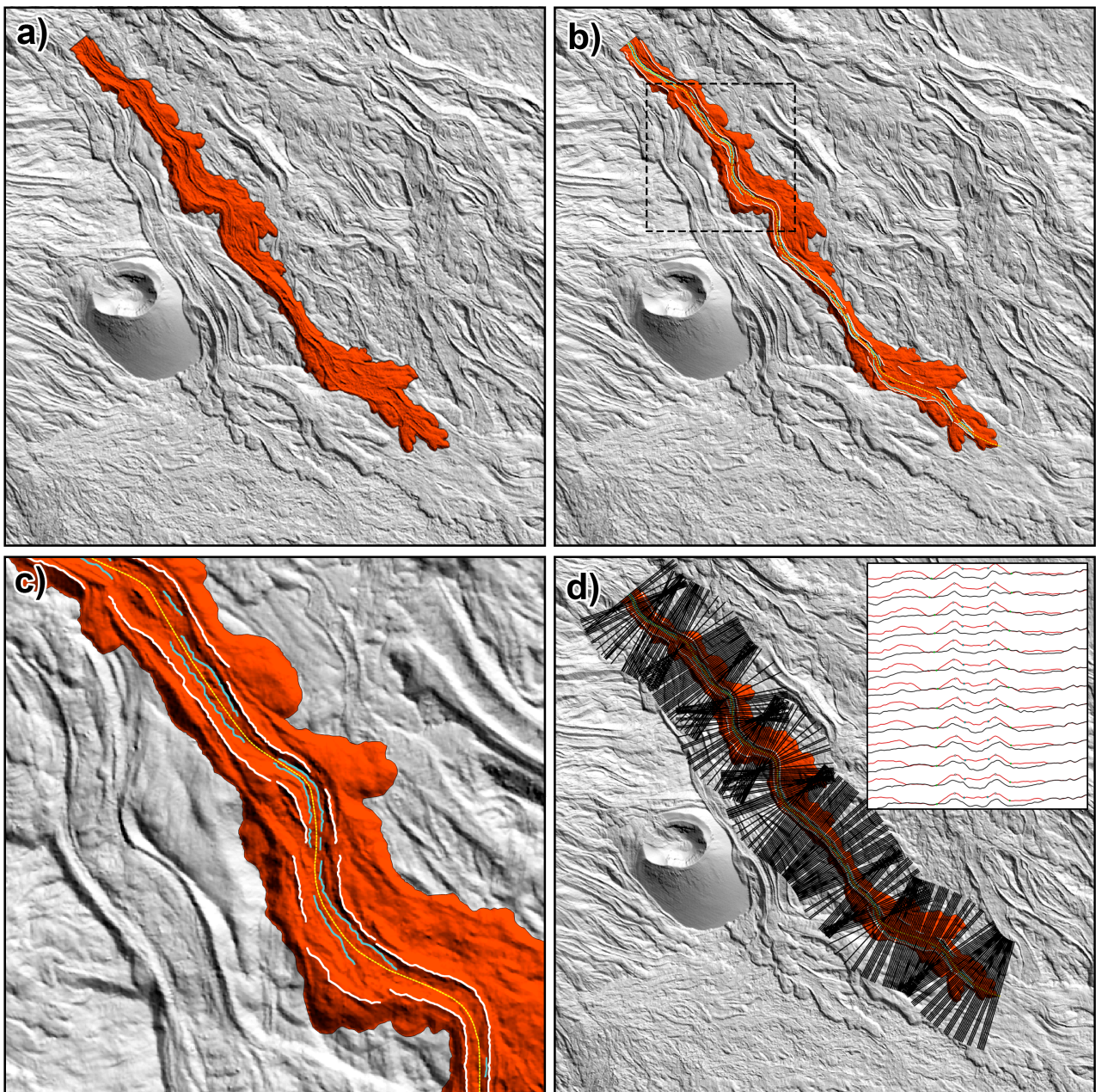


**Fig 4.3** Main steps of the morphometric analysis procedure. a) Identification of a proper lava flow (channel 202 in this example). The flow is highlighted in orange even if the base has not yet been traced in this step; b) Tracing of axes (yellow line), the polygon delimiting the lava flow base (in orange), the lines of levees (white lines), and the lines of the edges between the levees and the channel beds (charming lines). The square dotted line indicates the location of frame

c; c) Zoom inside a section of the selected channel showing the surface-specific elements detected. While axes and base polygons must be present and continue for running the code, levees and edge lines can be absent or locally interrupted; d) The 2D profiles traced normal to the axes for morphometric measurement. In the inset the profiles returned as input: the pre-emplacement profile is plotted in black, the post emplacement profile in red. The emplacement of another flow closer to the analyzed one is also visible.

The automatic helping tool is similar to that of the procedure described by Tarquini et al., (2012b). Firstly, the tool traces automatically sections with chosen length (depending on the flow width) to be provided as input. These sections are orthogonal to the flow unit axis with a given sampling interval provided as input (in our case every 2 m). A profile is derived from each section, and is considered as a function in the form  $z = f(x)$ , where  $z$  is the elevation and  $x$  is the coordinate along the section. The first derivatives of  $z$  and the Topographic Position Index  $TPI$  (see Chapter 3 for details) are then calculated over the profiles to identify surface-specific points on the original profile, namely the points of relative minima and maxima and the points of  $TPI$  maxima and minima. Maxima and  $TPI$  maxima points are expected to be along the crest of the levees, the minima and the  $TPI$  minima points along the base of the flow and on the channel-bed edges. Secondly, the tool automatically traces lines connecting surface-specific points for a given searching ratio  $R$ . Finally, surface-specific points and lines are visualized in GIS overlaid to hillshading,  $SVF$  and openness maps and specific morphological elements (i.e. flow base, levees and channel-bed edges) are traced manually (Fig. 4.3b and c). In particular, maxima and  $TPI$  maxima points and lines were overlaid to  $SVF$  maps to identify the levee ridges, while the minima and  $TPI$  minima were overlaid to the openness map to identify the flow-base and the channel-bed edges (see Chapter 3; and Favalli and Fornaciai, 2017).

Once all the input has been made available, the morphometric tool is run. The mandatory inputs for running the code were: i) a DEM; ii) the line of flow axes; and iii) the polygon of the flow base. The lines of the levees and base edges can be present, absent or locally interrupted. Where the optional inputs are absent, the code does not return any output. Elevation profiles normal to the axes are created and the intersection points among the profiles and the flow base polygon, and the levee and channel-bed edge lines are detected (Fig. 4.3d). The morphometric tool returns as outputs the successive 2D profiles aligned one below the other and centred along the axis of the flow (Fig. 4.3d, inset) and a text file reporting the parameters listed in Table 4.1.

Although the morphometric tool requires as input both the pre- and post-emplacement DEMs, it also works with the post-emplacement DEM only. In this case the pre-existing profile is interpolated following the Tarquini et al. (2012) method. The morphometric parameters are described in Table 4.1 and visualized in Fig. 4.2.

### 4.3 Morphometric analysis of selected channel-fed lava flows

Eleven channel-fed lava flows (Table 4.2) have been selected on the basis of the criteria described above. Nine flows were emitted during the 2008-09 Etna eruption (see Chapter 2) and belong to the same lava field (Fig. 4.4a). They are imaged by the 2010 LiDAR survey. For three of these flows the pre-emplacement 2007 LiDAR DEM is available. For two of these flows we cannot assume that the flow did not emplace on the lava emitted during the same eruption. Four flows were certainly emplaced over the flow emitted during the same eruption. Two flows were emitted during the 2006 Etna eruption (see Chapter 2) and imaged by the 2007 LiDAR DEM (Fig. 4.4b). The eastern flow has uncertain pre-existing topography; the southern flow has the 2005 LiDAR DEM as pre-existing topography (Table 4.1).

N	ID <sub>ch.</sub>	Eruption	DEM <sub>post</sub>	DEM <sub>pre</sub>
1	101	2008-09	2010	2007
2	102	2008-09	2010	2007
3	111	2008-09	2010	2007
4	201	2008-09	2010	2007(?)
5	202	2008-09	2010	2007(?)
6	203	2008-09	2010	/
7	301	2008-09	2010	/
8	302	2008-09	2010	/
9	303	2008-09	2010	/
10	501	2006	2007	2005(?)
11	602	2006	2007	2005

**Table 4.2.** Selected lava channels with the eruption and the year of post- and pre-emplacement of DEMs.

Figs 4.5a, b c and d show the evolution of morphology along the flow for the selected channel-fed lava flows. For each channel seven parameters were plotted as function of the distance ( $L$  in meters) along the axis from the vent towards the lava front. The parameters are the following: the slope of levees ( $\theta_{\text{levee}}$ , calculated as average between the right and left levees), the slope of pre-existing topography ( $\theta_{\text{pre}}$ , averaged for three profiles; we used the actual value when the pre-existing topography was available and the interpolated value when it was not), widths of the flow ( $W_{\text{flow}}$ ), channel ( $W_{\text{channel}}$ ) and bed ( $W_{\text{bed}}$ ) and thickness of right ( $H_{DX}$ ) and left ( $H_{SX}$ ) levees. Left and

right are identified with respect to the flow direction. We used the principal axes ( $D$  in meters) for the metric measurements and the secondary axes ( $\theta$  in degrees) for the angle measurements.

Figs 4.5a, b c and d show that local variations in the slope angle are strong enough to significantly scatter the data. Channels where the pre-existing topography was available (i.e. channels 101, 111, 102, 201, 202, 501 and 601; Figs 4.5 a, b and d) show a certain consistence between the pre-existing slope and the levee slope. This is relevant because  $\theta_{pre}$  is hardly ever measurable, while  $\theta_{levee}$  can always be measured by topography.

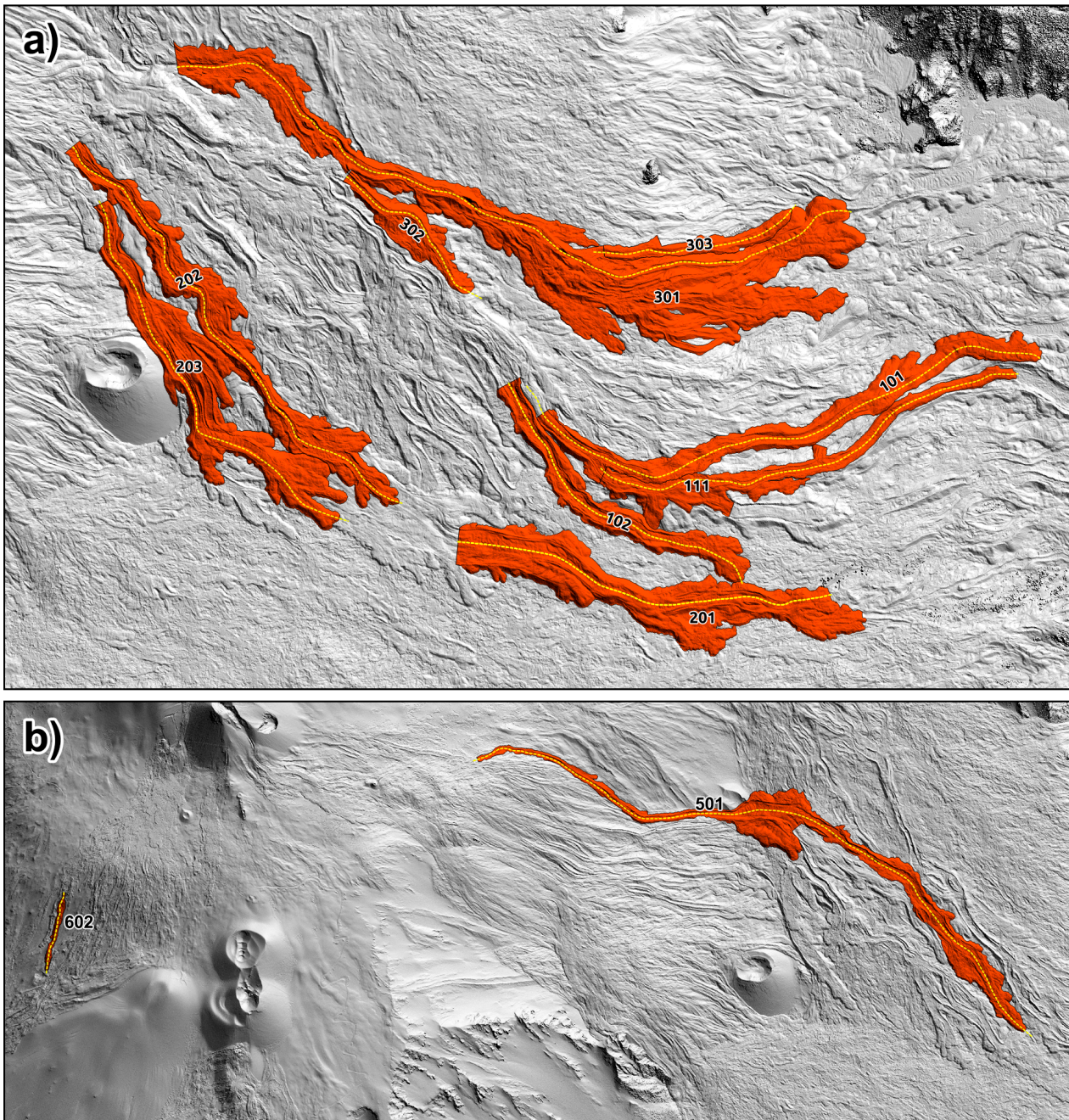


**Fig. 4.4** Selected lava flow. a) Selected lava flows emitted during the 2008-09 DEMs, properly labelled. The yellow lines indicate the channel axes. The hill-shaded DEM derives from the 2010 LiDAR data. b) Selected lava flows

emitted during the 2006 DEMs, properly labelled. The yellow lines indicate the channel axes. The hill-shaded DEM derives from the 2007 LiDAR data.

The plots show that the average downhill increase of the channel width described in Mazzarini et al. (2005) and Tarquini et al (2012a) is not a general rule for the Etna channels. The  $W_{channel}$  of the 111, 102, 201, 202, 203 and 301 channels shows different trends for various segments inside the same channel, often related to an appreciable or relevant  $W_{channel}$  decreasing downhill. The general negative correlation between pre-emplacement slope and channel width (Tarquini et al 2012b) is largely confirmed with some exceptions: channel 201 shows a strong reduction of  $W_{channel}$  up to  $L = \sim 750$  m downhill without significant variation in the slope value. At  $L = \sim 750$  the slope increases roughly and the  $W_{channel}$  stops decreasing (Figs 4.5b); the  $W_{channel}$  of channel 203 increases up to  $L = \sim 700$  m downhill and then decreases. From that point downhill, the slope and  $W_{channel}$ , surprisingly, seem to be directly correlated (Figs 4.5b). Channel 601 shows a relevant slope decrease at about 1600 m along the axes, which can be correlated with strong increase of the channel width (Figs 4.5d).  $W_{channel}$  of the 111, 203 and 301 channels decreases downhill without a significant slope increase (Figs 4.5a, b and c).

$W_{channel}$  and  $W_{bed}$  have almost the same trend along the flow (local maxima and minima are generally aligned) and they usually converge towards the dispersed flows where the levees gradually reduce their thickness and width. The general negative correlation between pre-emplacement slope and channel-bed width is confirmed. Channel 203 is no exception, while the data are lacking for channel 201.

Levee thickness measurements generally show that the channels have a symmetric shape. The only relevant exception is again channel 203, where we can appreciate a consistent difference between  $H_{DX}$  and  $H_{SX}$  in the first half part of the plot (Figs 4.5b). Also worth noting is the strong asymmetry generated by the abrupt slope change in channel 501, asymmetry that rapidly disappears soon after the break in the slope (Figs 4.5d). Trends of  $H_{DX}$  and  $H_{SX}$  are somehow inversely correlated to those of  $W_{channel}$  and  $W_{bed}$ .  $H_{DX}$  and  $H_{SX}$  are generally much lower than the  $W_{channel}$ . Channel 302, where  $H_{DX}$  and  $H_{SX}$  have almost the same value of  $W_{channel}$ , is an exception (Figs 4.5c). Channels 202 and 301 show a variation in channel width and levee thickness ratio along the flow (Figs 4.5b and c). The relationship between channel-bed width and levee thickness does not follow a general rule, with  $H_{DX}$  and  $H_{SX}$  that can be lower than the  $W_{bed}$  (channels 101, 111 and 102, Figs 4.5a), almost equal (channel 303, Figs 4.5c) or higher (channel 302, Figs 4.5c). In many channels their ratios change along the flow (channels 201, 202, 203, 301, 501 and 601, Figs 4.5b, c and d).

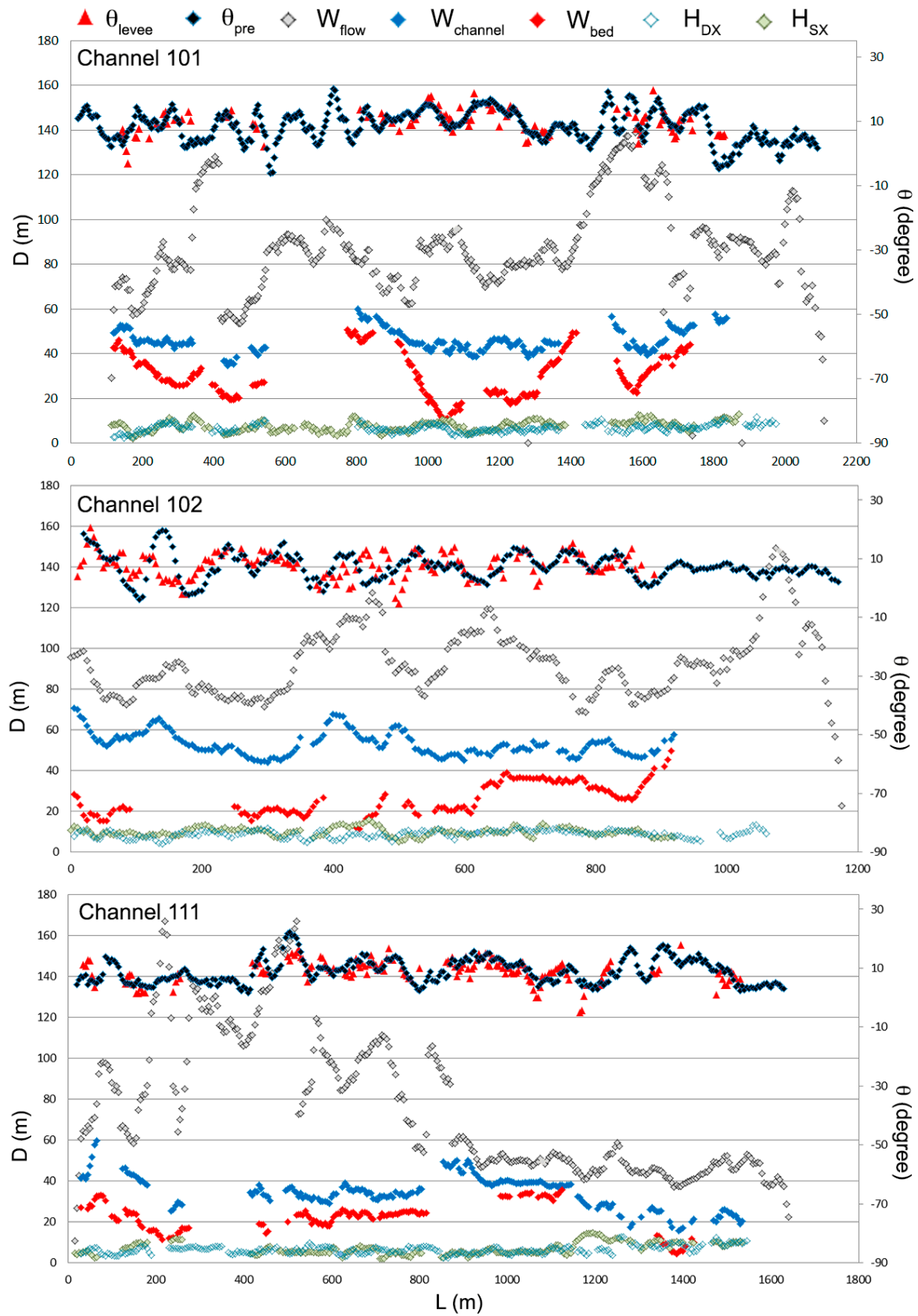


**Fig 4.5a** Summary of plot of selected morphometric data calculated from channels 101, 102 and 111. For all these channels the pre-existing slope is calculated directly on the pre-emplacment DEMs. On the principal axis,  $D$  is the metric dimension of channel, channel-bed and flow widths and levee heights. On the secondary axis,  $\theta$  is the angle dimension of the levees and pre-existing slopes.

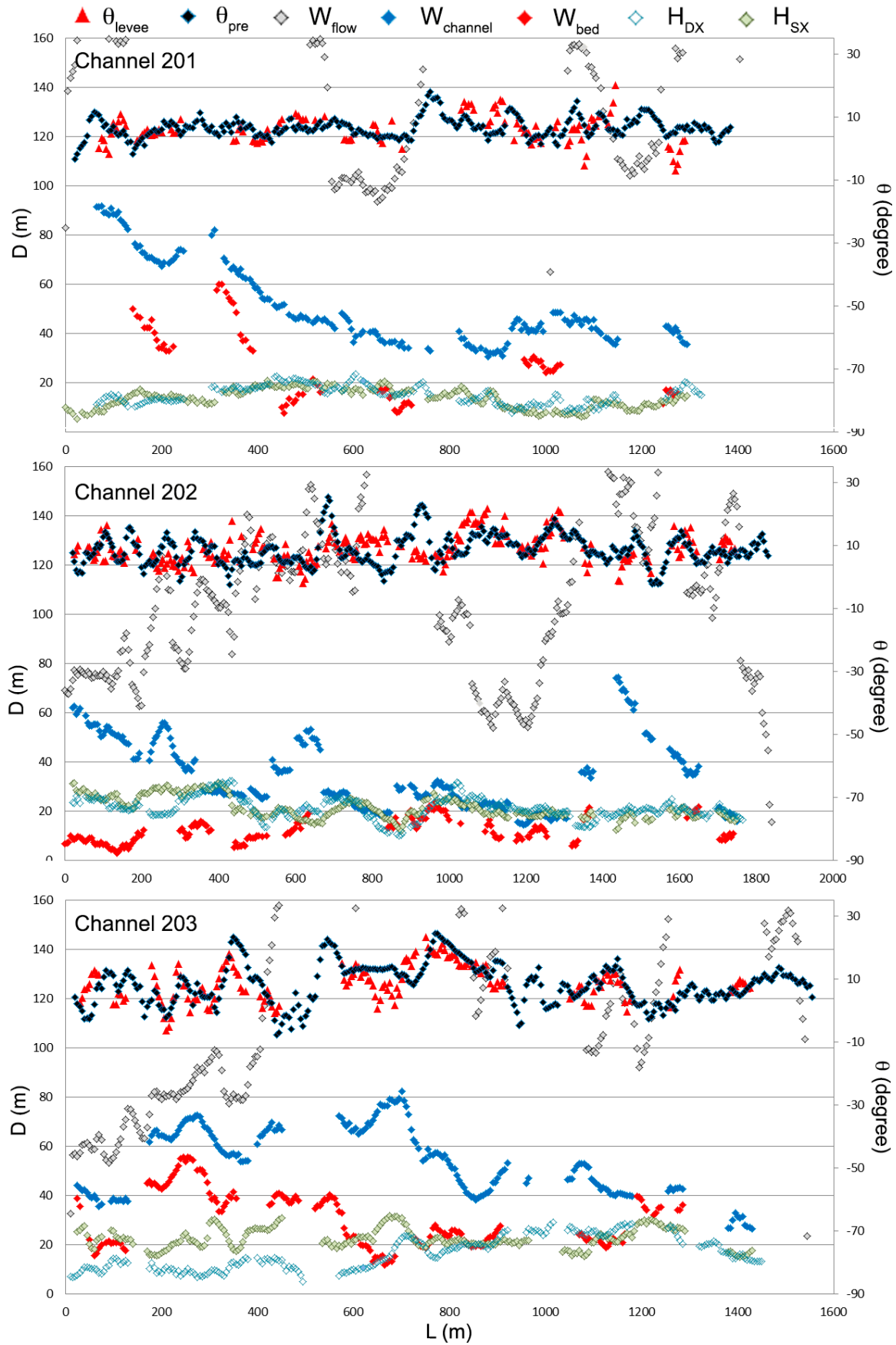


**Fig 4.5b** Summary of plot of selected morphometric data calculated from channels 201, 202 and 203. For channels 201 and 202 the pre-existing slope is calculated directly on the pre-emplacement DEMs, while for 203 it is interpolated. On the principal axis,  $D$  is the metric dimension of channel, channel bed and flow widths and levee heights. On the secondary axis,  $\theta$  is the angle dimension of the levees and pre-existing slopes.

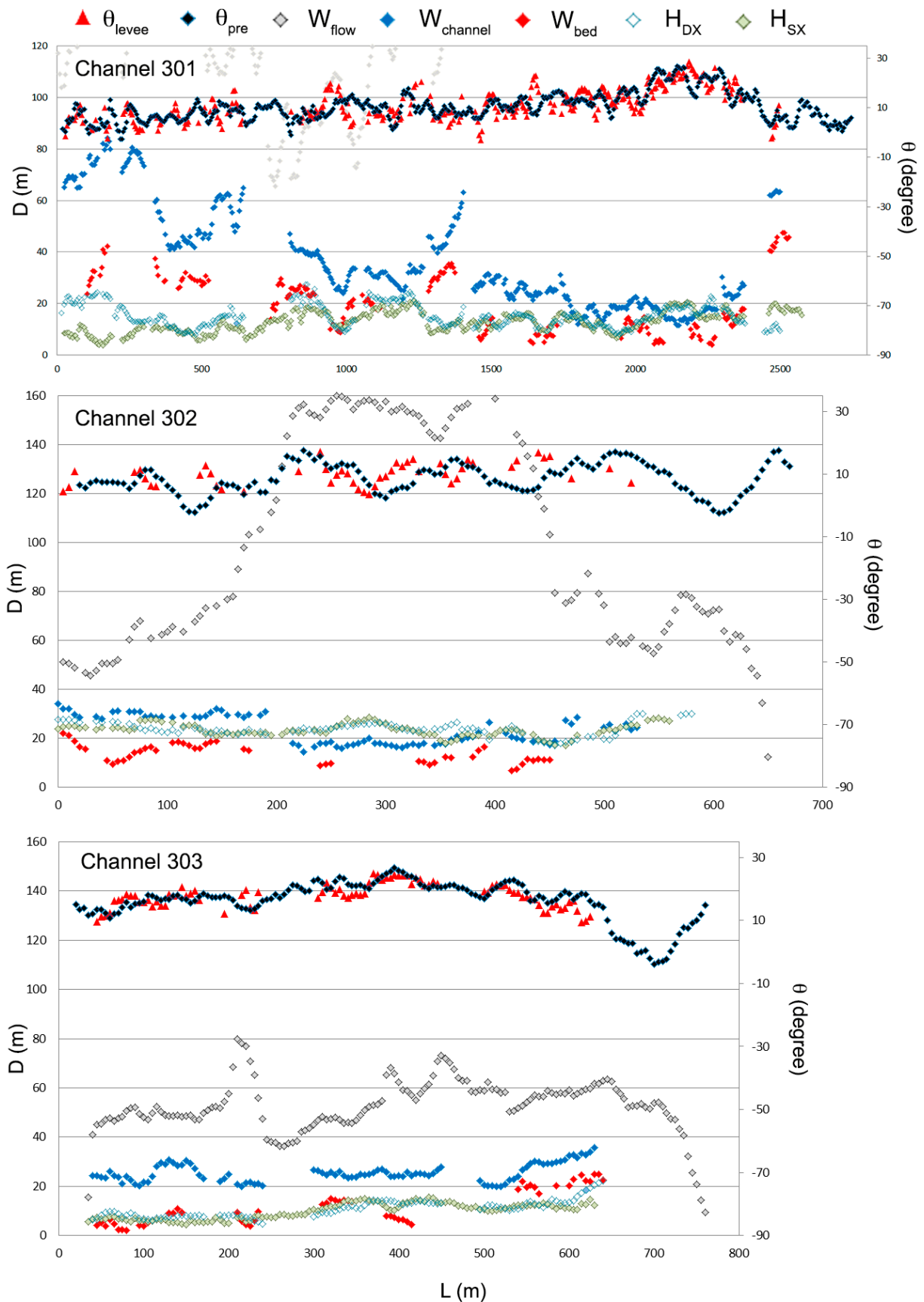


**Fig 4.5c** Summary of plot of selected morphometric data calculated from channels 301, 302 and 302. The pre-existing slope is interpolated for all these channels. On the principal axis,  $D$  is the metric dimension of channel, channel-bed and flow widths and levee heights. On the secondary axis,  $\theta$  is the angle dimension of the levees and pre-existing slopes.

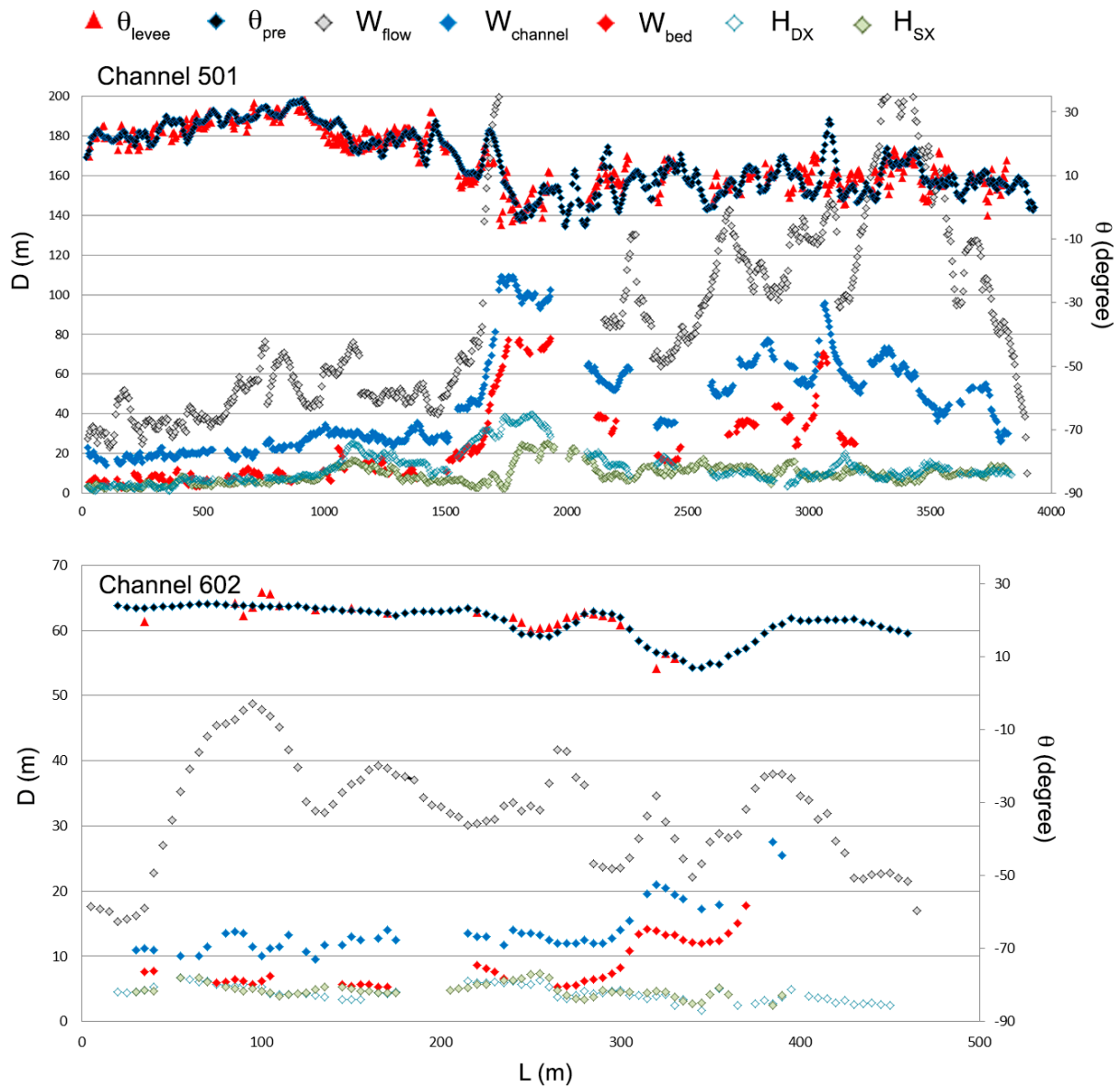


**Fig 4.5d** Summary of plot of selected morphometric data calculated from channels 501 and 602. For all these channels the pre-existing slope is calculated directly on the pre-emplacment DEMs. On the principal axis,  $D$  is the metric dimension of channel, channel-bed and flow widths and levee heights. On the secondary axis,  $\theta$  is the angle dimension of the levees and pre-existing slopes.

Overall, our data support an inverse relation between slope and channel width, at least for large-scale observation, even if there may be some exceptions. This relation stresses the importance of topography for predicting the path of the flow and for investigating the emplacement dynamics. The average slope of levees is consistent with the pre-existing slope, namely it can be used when the slope of topography cannot be measured, which occurs most of the time. Channel and channel-bed widths have to some extent the same trends since the local minima and maxima are generally aligned. Channel widths are usually much wider than the levees, while the channel-bed width can be greater, smaller or equal to the height of the levees. The channels tend to be largely symmetrical.

The mutual relationships among  $W_{channel}$ ,  $W_{bed}$ ,  $H_{DX}$  and  $H_{SX}$  allow to describe the geometry of the channel to be used for lava flow modeling.

The relevant influence of cross-sectional channel geometry for inferring lava rheology and effusion rate of active lava flows was described by Lev and James (2014), who conclude as follows: *“the demonstrated importance of knowing the shape of lava channels implies further research should be done to characterize the statistical distribution of channel cross-section shapes and the representation of various end-member geometries in different environments.”*

The systematic collection of detailed morphometric parameters along and across lava flow units provided in this work offer the opportunity to improve significantly the calibration and validation of computational models.

---

## Chapter 5

---

### **UAV-based remote sensing surveys and Structure from Motion technique for generating a very-high-resolution DEM of 1974 Mount Etna Lava flow**

Chapters 2 and 4 describe the relevance of the lava flow morphometric analysis for defining the flow system and the associated flow dynamics. In quantifying lava flow field morphologies, generation of DEMs and acquisition of imagery is a first mandatory step. Active volcanoes need for a constant DEM updating, otherwise, in case of eruption, the models called to predict the path of lava are run over false topography and then reasonably they will return erroneous scenarios. This calls for a frequent DEMs updating, at least after the main eruptive events. Airborne LIDAR system is able to provide topographic data with proper coverage and spatial resolution, but mission deployment is sufficiently costly to prevent a frequent employment of this technology. For this reason, it is essential in lava flow studies to find new solutions that are able to acquire high-resolution topographic data over large area and with reasonable costs.

The development of the Structure-from-Motion (SfM) computer vision technique has provided a low-cost and user-friendly tool for generating high-spatial resolution digital topography using images acquired by consumer-grade digital camera images. The SfM method solves for camera position and scene geometry simultaneously and automatically, using a highly-redundant bundle adjustment based on matching features in multiple overlapping images (Favalli et al., 2012b; James and Robson, 2012; Westoby et al., 2012; Nouwakpo et al., 2014). The SfM method, as well as, improvements in quality of consumer-grade digital cameras and methods for camera calibration has thus encouraged the use of digital photogrammetric techniques for 3D modeling of volcanic

features over recent years (James and Varley 2012; Tuffen et al., 2013; James and Robson 2014; Farquharson et al., 2015; Kolzenburg et al., 2016; Richter et al., 2016; Neri et al., 2017).

The recent proliferation of Unmanned Aerial Vehicle (UAV), often known as “drone”, technology has presented a new, flexible, low-cost platform option for volcano remote sensing. UAV represents an ideal platform to make the best use of the SfM method. Capable of overflying large areas in a short period of time and of operating below cloud decks that block satellite views, the flexibility of operation, the possibility of high temporal resolution and spatial resolutions, as well as the array of cheap sensor pay-load options, make the UAV-camera system an outstanding new option for the volcano remote sensor. The extreme spatial and temporal resolutions possible from the UAV-based perspective allow extension and combination of existing methodologies and development of new methodologies to allow a fully integrated-analysis of topographies at a variety of spatial scales. The result is a significant advance in our power to analyze, track and understand dynamic Earth surface morphologies, allowing improved monitoring, surveillance and science. In addition, when carried out during an ongoing eruption, UAV-based mapping promises prompt detection and ease-of-measurement for developing lava flow features; timely measurement of which are of paramount importance for hazard assessment. For example, initially lava tends to spread from the eruptive source as sheet flow, which extends as a thin layer that cool and stop quickly (Hon et al., 1994; Umino et al., 2006). With time and distance, though, initial levees form to define lava channels (Sparks et al., 1976; Hon et al., 1994; Harris et al., 2005a). These pathways are able to carry lava more efficiently, thus allowing greater final flow lengths (Kilburn 2004), but rates of heat loss and hence also cooling are still relatively high (Cashman et al., 1999; Robert et al., 2014). Potential flow length increases further if lava tubes develop (Harris and Rowland 2009), where lava flowing in tubes undergoes very low rates of heat loss, and hence cooling (Keszthelyi 1995), so that lava can extend much greater distances from the vent than when flowing within channels (Calvari and Pinkerton 1998, 1999; Kauahikaua et al., 1998). While sheet flow and channels are easy to detect and map using remote sensing (e.g., Wright et al., 2001), continued lava supply to a flow front through systems of lava tubes can be tracked from the distribution of breakouts and ephemeral vents developing around the stationary margins of an apparently stalled, inflating lava flow fronts (Mattox et al., 1993; Calvari and Pinkerton 1998, 1999; Kauahikaua et al., 1998). Thus, the ability to map the changing morphology (sheet-to-channel-to-tubed flow) of channels and tubes and the lava flow units they feed, as well as their distribution within an active lava flow field, is of paramount importance for hazard assessment.

In Chapter 5, we review an integrated methodology that combines the UAV-based remote sensing capability with the SfM method to allow application of systems-related science at a lava flow field. We generate a very-high-spatial resolution (20 cm) DEM and derive maps, as well as a 3 cm spatial resolution orthomosaic, for the lava flow field of Etna’s 1974 eruption (Fig. 5.1). To do

this we use photogrammetric data collected with a consumer grade camera during UAV-based over flights in May and September 2015. The SfM-derived DEM is compared with the one-meter LIDAR-derived DEM, where we qualitatively and quantitatively describe the advantages of increasing the DEM resolution up to decimeter when completing morphometric analyses.

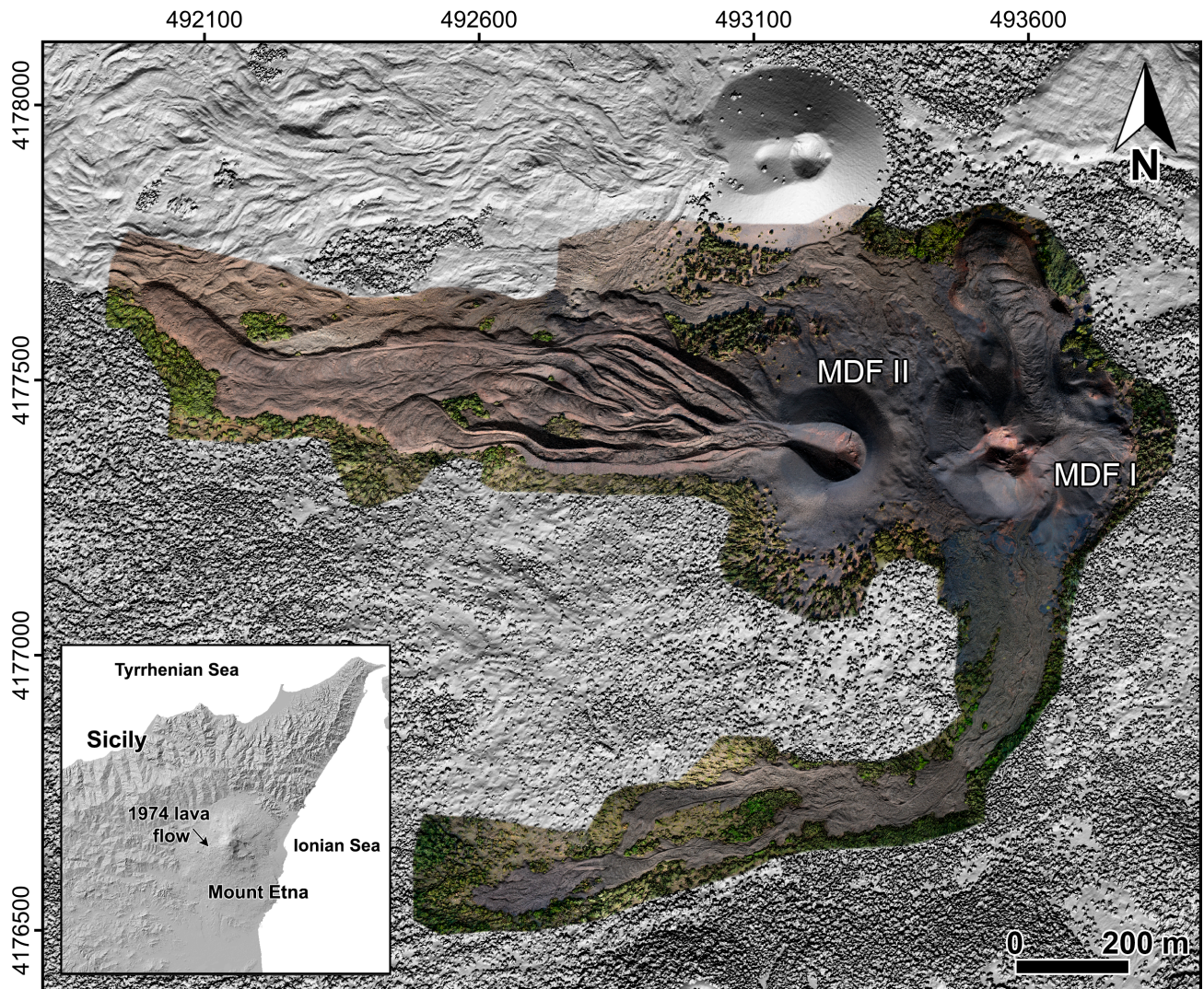


**Fig. 5.1** UAV-data-derived orthophoto mosaic of Mt. Etna’s 1974 lava flow and cone system overlaid on the shaded relief derived from a merge of the 1-m and 20-cm DEMs. The RGB area indicates the area imaged during the UAV surveys and where the DEM was reconstructed starting from the photos. MDF I and MDF II stand for Mount De Fiore I and II, respectively. The inset shows the location of the 1974 lava flow.

## 5.1 The 1974 Mount Etna flank eruption

The 1974 eruption of Mount Etna occurred at a relatively low elevation (~1660 m a.s.l.) on the west flank, a location approximately 6 km from the Summit Craters, and 6 km from the nearest villages

(Fig. 5.1). It consisted of two phases activity separated by 22 days of quiescence (Bottari et al., 1975). Effusive and explosive activity built up two compound lava flow fields and two scoria cones, named the Mount De Fiore I and II (Fig. 5.1). The first eruptive phase began on 30 January and produced the cinder cone of Mount De Fiore I (MDF I), which reached a height of about 70 m and a width of 300 m in just a few days (e.g., Tazieff 1974; Corsaro et al., 2009). The first phase involved ten discrete lava fountaining and effusive episodes that produced ten individual lava flow units (Tanguy and Kieffer 1977). The first phase of activity stopped on 16 February. A new highly explosive activity began on 11 March and rapidly built the 50-m-high cinder cone of Mount De Fiore II (MDF II), from which lava flows advanced westward. The eruption ended on 29 March.

## 5.2 UAV field survey of the 1974 lava flow

Photogrammetric campaigns were carried out using a Dà-Jiāng Innovations Science and Technology Co., Ltd (DJI) hexacopter (model F550), with onboard GPS system and internal gyroscope (Fig. 5.2). The hexacopter has a payload capacity of around 2.4 kg. The 10,900 mAh battery allows about 20 minutes of flight time.

The Ground Station Software v4.0.11 allows the flight plan (including platform velocity, altitude and direction) to be defined and uploaded to the onboard autopilot. The autopilot also ensures platform stability by controlling the craft pitch, roll and yaw using the real-time information feed from the gyroscope. There is also an option of radio control, which includes a return-direct-to-base (mission abort) button. Further details about the UAV system used in this work are described in Nannipieri et al. (2016).

Italian law requires two independent radio control systems to be deployed so that a back up is always on site. The second system cuts power to the drone if contact with the first system is lost, thereby terminating the flight. The UAV was equipped with a consumer grade Sony NEX-5T, a 16 megapixel camera which is 111 mm × 59 mm × 38 mm in size and can provide 4912 × 3264 pixel images. The E 16-50 mm zoom lens has a 24 – 75 mm focal length, an 83 – 32° field of view and a minimum aperture of f/22 – f/36. The Sony NEX-5T weights 0.39 kg.

Camera calibration was completed by using the Lens tool function of PhotoScan Pro 1.2, which uses a standard black and white chessboard grid to calculate the lens focal length and distortion properties so as to provide a lens-distortion correction.

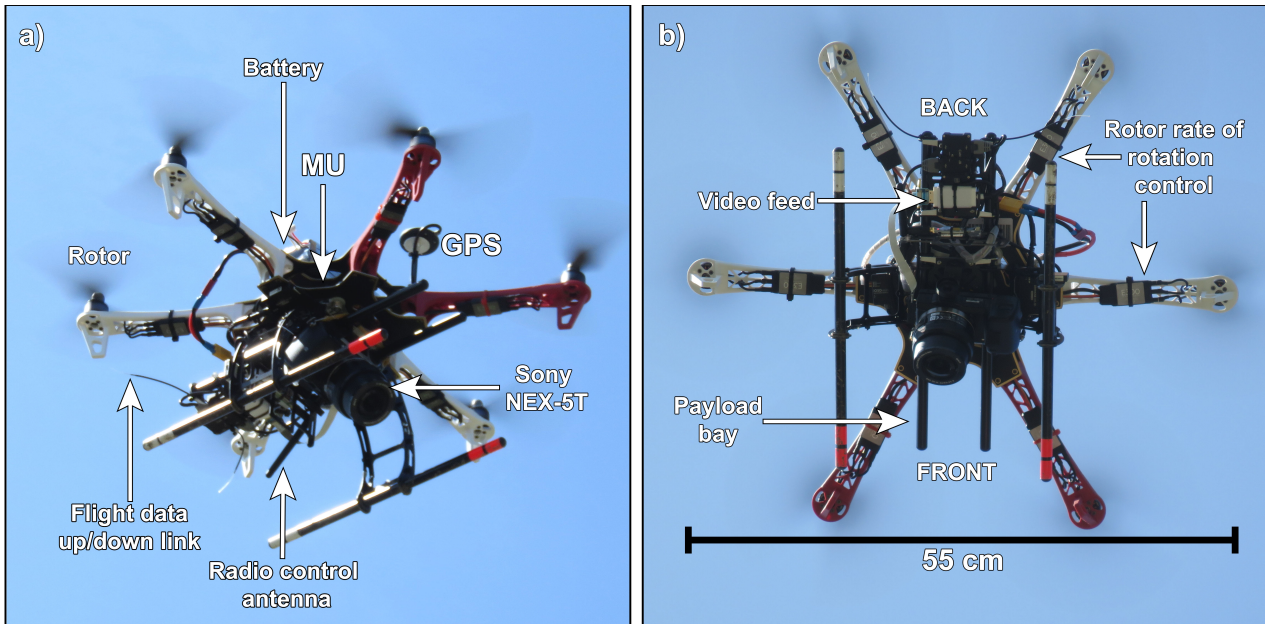


**Fig. 5.2** The platform and sensor system used during the survey operation.

Flight planning needs to be set up so as to ensure a flight altitude, craft velocity and imaging frequency that allow sufficient overlap between images to allow SfM photogrammetry reconstruction. All acquisitions were fixed at a zoom of 16 mm, and images were acquired at an oblique angle of  $24^\circ$ . As a result, pixel viewing angles range from  $0^\circ$  (for the pixel immediately below the drone) to  $48^\circ$  at the image edge. This ensures that each pixel is viewed at sufficiently high angles so as to reduce overall geometric errors when compared with a vertical view. If we set flight altitude to 70 m above ground level (AGL) then, for an angular field of view of  $83^\circ$ , the image area will be trapezoidal with a width of 78 m and a length of 104 m for its short edge and 157 m for its long edge, giving an image area of 10,179 m<sup>2</sup>. This gives a nominal pixel size of 2.5 cm. If we image once every two seconds at a craft velocity of 10 m/s we will thus image every 20 m of flight; meaning that each point is imaged in the flight path direction four times from four different angles. Given overlapping flight paths in the cross-track direction, each point is imaged 21 times. This flight plan was entered into the Ground Station Software v4.0.11.

The result is displayed on Google Earth™ for checking, and the flight plan can then be uploaded to the autopilot. Flight time is taken into account when setting up the flight plan and cannot exceed the battery lifetime of 20 minutes.

Flight planning also needs to take into account national flight law. For the 1974 lava survey, we need to follow the regulations of ENAC (Ente Nazionale per l'Aviazione Civile) that covers UAV (SAPR – Sistema Aeromobile a Pilotaggio Remoto – in Italian) operations over Italian sovereign airspace. At the same time, the camera is programmed to image once every two seconds, with images stored in raw format on the camera internal memory card. Raw image size is 48 Mb, so for 12 minutes of acquisition at a 2 second frame rate, card capacity needs to be 28.8 Gb. This capacity

can be reduced to around 5 Gb if images are collected in JPEG format, but use of the JPEG format reduces the final accuracy of the model.

We carried out 11 flights (Fig. 5.3) during two different campaigns, acquiring 2781 photographs over a total flight distance of about 40 km, which was completed during a total flight time of 124 minutes. From this, we built six topographic models, which covered six overlapping areas across the target zone. These, when merged, allowed complete flow field coverage (Fig. 5.3).

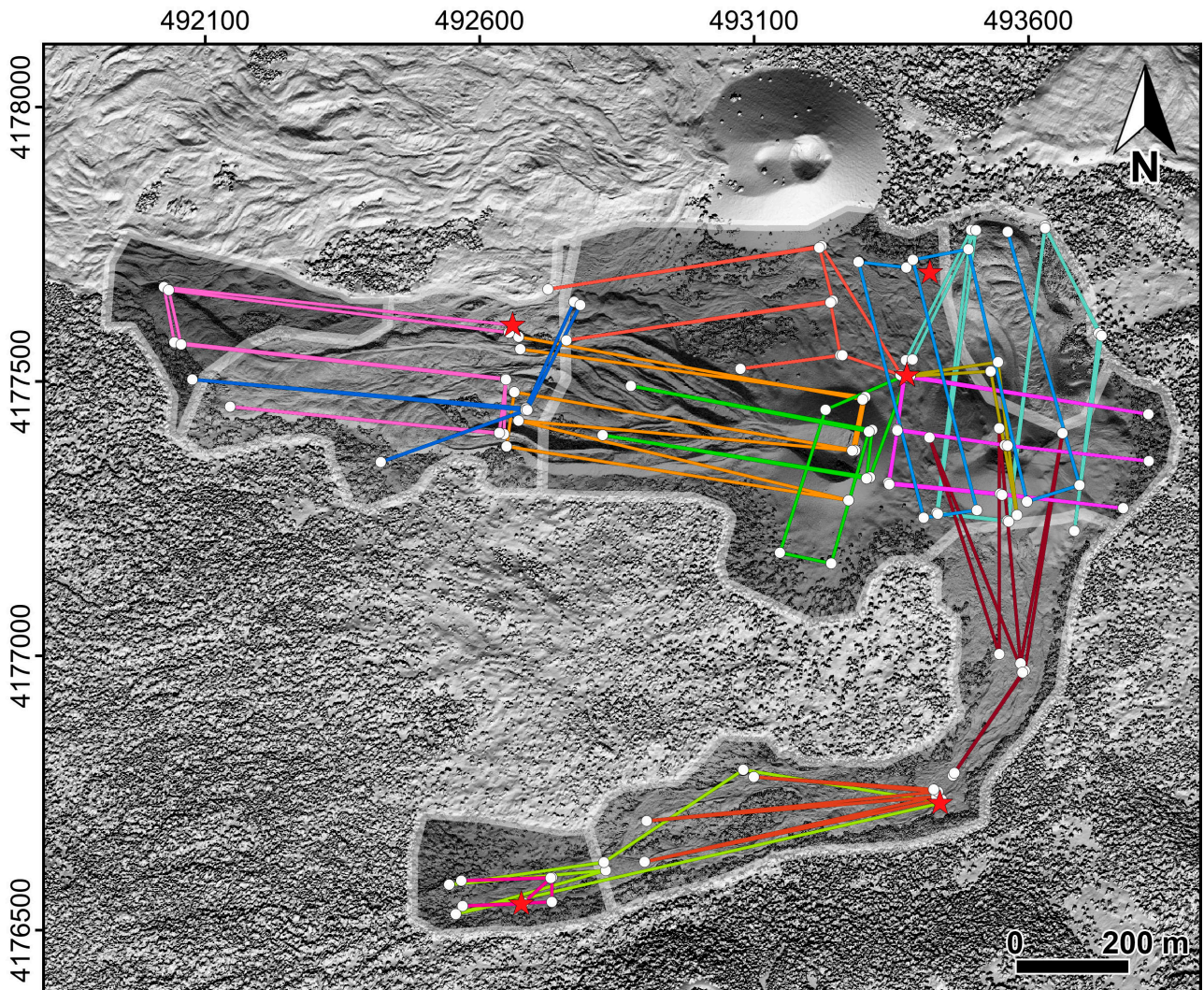


**Fig. 5.3** Flight plan for the survey of the 1974 lava flow field with the six sub-areas imaged during each flight. Solid lines mark UAV flight paths, dots the change of direction and the stars the launch-landing locations.

### 5.3. DEM and orthomosaic generation

#### 5.3.1 SfM DEM generation

The 3D model was generated using the Structure from Motion (SfM) module as implemented by Agisoft PhotoScan Professional version 1.2. As a preliminary step, we organized the acquired photos into six different photo sets. This was necessary because the data set was particularly large and because the photographs were collected on different days and/or under variable lighting conditions. To build the 3D model we input the images and camera calibration parameters into PhotoScan Pro 1.2. As a first step the images were loaded into PhotoScan and an automated image feature identification routine was run. All the pictures were processed in loop by a pattern recognition algorithm and matched to each other to find corresponding features in different images. In this way a series of key points was obtained. This process was carried out using the scale invariant feature transform (SIFT) algorithm (Lowe 2004). In step 2, matching features identified in multiple images are used to resolve the camera positions and scene geometry using a highly redundant bundle adjustment. This output an initial, sparse, point cloud. Step 3 thus involved creation of a dense cloud, which was derived directly using the, now known, camera position relative to each image. All pixels in all images were used, so that the dense model has a resolution a few times lower than that of the raw photographs. This step is termed multiview stereo matching (MSV). This workflow allowed derivation of  $270 \times 10^6$  points, from the 2781 photographs input, over a total area of  $1.35 \text{ km}^2$ , for a point density of 200 points per square meter (Fig. 5.4a).

The point clouds must be now positioned, oriented and scaled. To do this, three points at different spatial positions in the cloud were tied to ground control points to allow initial, rough, georeferencing of the slave (the point cloud) to the master (which in this case was a 2005 LIDAR-derived DEM of Mt. Etna as generated by Favalli et al., 2009).

To more precisely match the point-cloud to the surface, we minimized the root mean square (RMS) error between the master and the slave by iteratively varying the three angles of rotation, the translation and the magnification or reduction factor of the slave using a custom-made algorithm based on the MINUIT minimization library (James and Roos, 1977) as described by Kolzenburg et al. (2016). Best fit was obtained with an RMS error of 0.24 m.

Six DEMs (Fig. 5.3) were created from the six georeferenced point clouds. Given the point density, we could quantize the data into a 20 cm pixel grid, meaning that we had eight points per pixel. These six DEMs were merged to create a single very-high spatial resolution DEM of the 1974 lava flow field. The orthomosaic (Fig. 5.5) was then created automatically using the “build automosaic” tool of PhotoScan Pro. In setting up this tool, we were careful to maintain the spatial resolution of the original images by entering 3 centimeters at the “output resolution” prompt. PhotoScan Pro then autorectified each pixel and built the orthomosaic. The output image was  $66,000 \times 44,000$  pixels, or almost 9 Gb in size and covered an area of  $1.98 \times 1.32 \text{ km}^2$ . Finally, the 3-cm resolution orthomosaic was georeferenced to the 20-cm DEM.

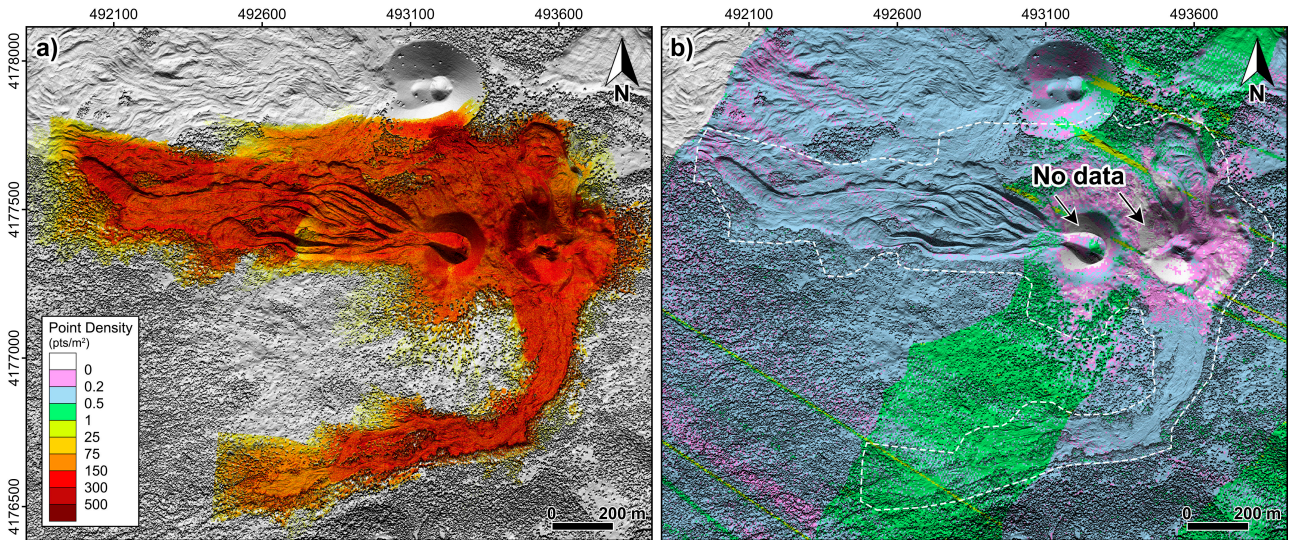


**Fig. 5.4** Point density distributions of the SfM and LiDAR 3D models. a) Point density distribution of the 1974 lava flow reconstructed using UAV-SfM methods. b) LiDAR point density distribution over the investigated area. The dotted line indicates the area reconstructed using the UAV-Sony NEXT system. The legend is the same of frame a.

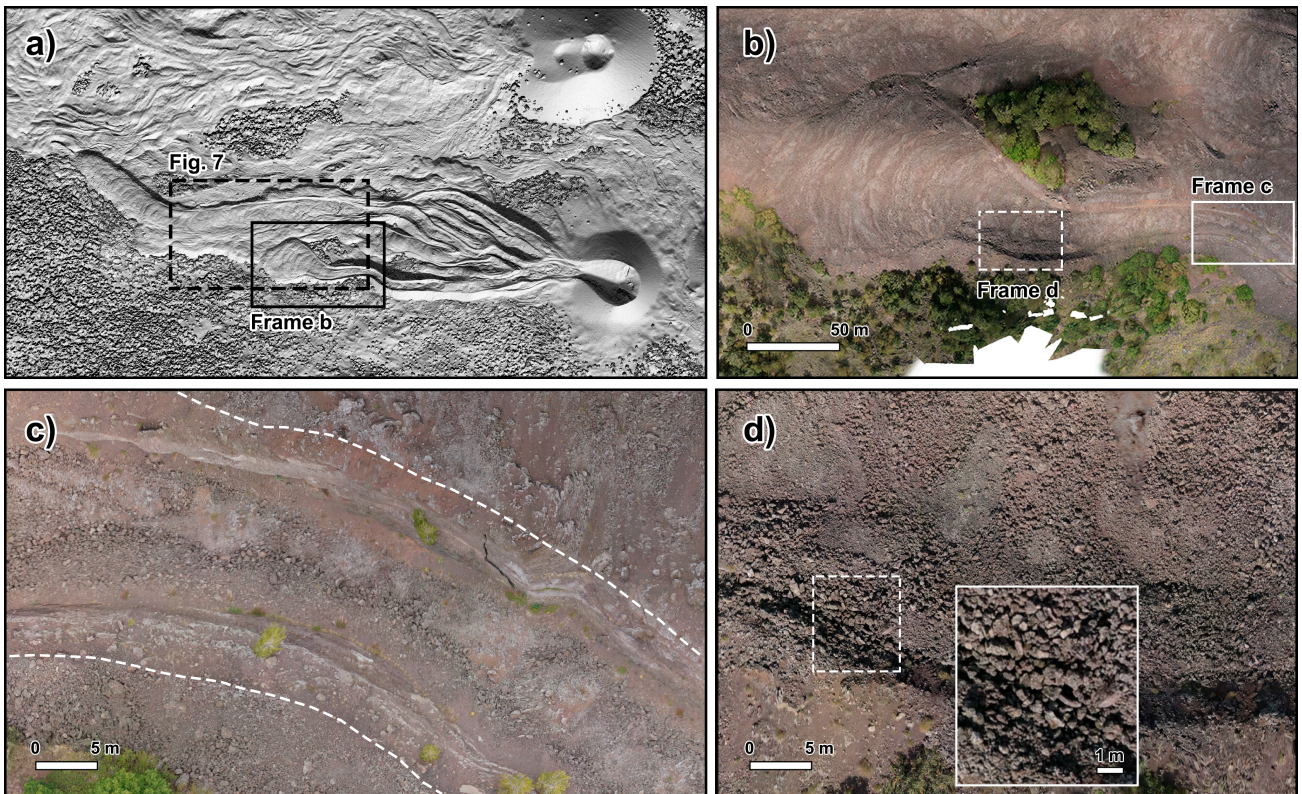


**Fig. 5.5** Specific zone extracted from the 3 cm orthomosaic image showing the cm-scale grain distribution of the lava surface at different scales. a) Location of the frame b; and b) Lava flow channel and dispersed flow showing the location of frame c and d; c) Section of lava channel imaged by the othomosaic. Different grain size from the levee (dashed lines) to the middle of the channel is evident; d) Lava channel near the transition zone imaged by the othomosaic. The presence of block with different grain size over the lava surface is evident. In the inset the area delimited by dashed box of the frame d is shown. Blocks of dimension less than 1 m can be easily identified and counted.

### 5.3.2. SfM DEM accuracy

Elevations for each pixel in the drone-data-derived DEM take the mean value for all points within the pixel. Thus, to describe variability inside each pixel we use the standard deviation ( $\sigma$ ) for each pixel. Generally, variability within a pixel was 1-3 cm, being maximized over vegetated zones (especially trees) where  $\sigma$  was over 1 m, depending on the height of the bush or tree (Fig. 5.6). We also found linear artifacts around the individual image edges. Artifacts corresponded to pixels in which we have a high (10 – 15) number of points. To clean up these artifacts, we rejected all points that were greater than  $2\sigma$  from the mean, and recalculated the pixel mean altitude. To understand the difference between the two DEMs, we re-sampled the UAV-derived DEM to 1-m; so as to make it comparable with the spatial resolution of the LIDAR DEM. The RMS error, across zones where we had both LIDAR and drone coverage, and excluding vegetated regions, was 0.22 m.

### 5.3.3 DEM-derivative maps

Using the original 1-m LIDAR DEM of the 1974 lava flow field, and the UAV-data-derived 20-cm DEM, we next derived parameters that, as described in Chapter 3, can be useful for lava flow morphometric analysis, that is: shaded-relief, sky view factor (SVF) and openness down maps (Fig. 5.7). These were obtained from the UAV-data-derived DEM placed into the LIDAR DEM. Placement of the former into the latter is merely aesthetically pleasing, allowing a rectangular region of analysis and output map to be set-up. To complete this merge, each 1-m LIDAR DEM pixel was divided into twenty-five 20-cm pixels across which values were interpolated. These values were used to fill the empty areas of the rectangular grid, especially around the irregular area that contains the drone coverage (Fig.5.3).

The sky view factor is described by a solid angle ( $\Omega$ ), open to the sky and expressed in terms of the total sky view possible from the given pixel, i.e.,  $SVF = \Omega/2\pi$  (see Chapter 4). It is thus the fraction of the sky visible from each pixel and ranges from zero to one, and was calculated following Zakšek et al. (2011). As described in Chapter 4, this approach assumes that there is a diffuse light source emitted across the entire celestial hemisphere. Ridges will be incident to nearly all of the in-coming light, and so will have values close to one; for depressions the opposite case will hold. As shown in Chapter 4, this method is extremely effective in mapping ridges, which in our case include levee rims (Fig. 7c and d). Yokoyama et al., (2002) introduced two parameters called positive and negative openness (hereafter called openness up and down respectively). The former measures the “openness of the terrain to the sky” while the latter is the “below-ground” openness (Yokoyama et al., 2002). The openness up takes high values on crests and ridges and it is

very similar to the SVF (see Chapter 3), the openness down takes high values inside valleys, gullies and craters. Because narrow cracks and fractures will form sharp incisions, they will have high openness down values (Fig. 5.7e and f). Thus, the openness down map is extremely effective in locating highly fractured areas of the lava flow surface so much so that the map can be called “crack map”.

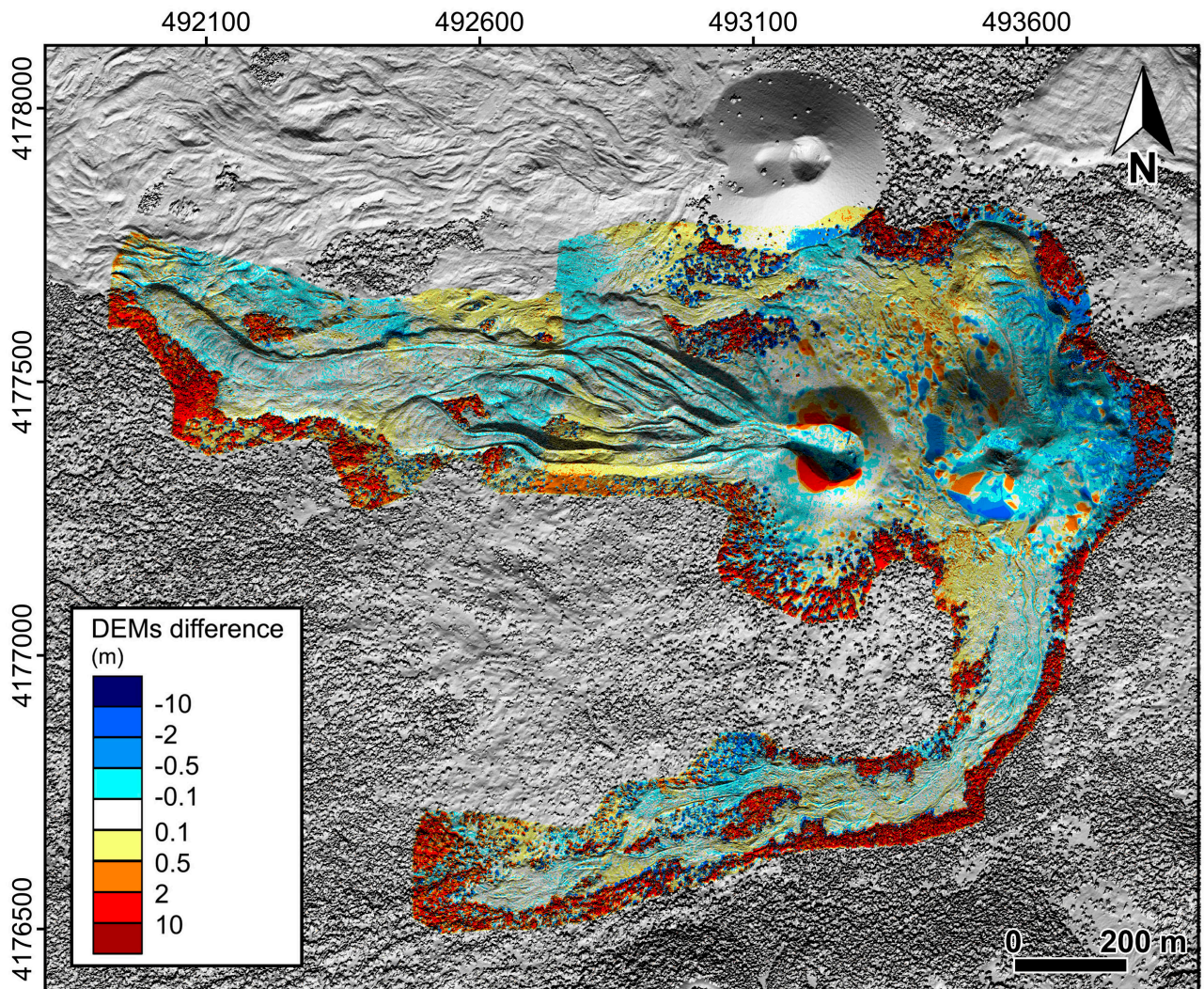


**Fig. 5.6** SfM and LiDAR DEMs difference quantifies the displacement and show its distribution. The areas interested by relevant differences are vegetated or correspond to the no-data or low data density in the LiDAR DEM.

#### 5.4. 20-cm versus 1-m DEMs: Qualitative and quantitative analysis

In 2005 we completed an airborne LiDAR campaign on Etna, which allowed construction of a 1-m spatial resolution DEM covering most of the edifice (Favalli et al., 2009). One-meter-pixel LiDAR data have already allowed us to complete morphological analyses of lava channels (Mazzarini et al.,

2005) and channel-fed systems (Favalli et al., 2010a), and to carry out best-fit modeling of lava flow through channelized systems (Harris et al., 2007). As reported by Cashman et al. (2013), other relevant lava flow features that can be mapped to aid in interpretation of lava flow emplacement dynamics are surface folds, tumuli, fractures, blocks, and lobate flow fronts. These features have often sub-meter spatial scales and are difficult to resolve using the 1-m LiDAR DEM. Generally speaking, over surfaces where roughness has a vertical and horizontal scale of variation that is less than 1-m, which is the case over pahoehoe and 'a'a flow surfaces (e.g., Crown and Baloga 1999), 1-m DEMs are not capable of imaging the whole spectrum of variation. We thus use our 20-cm DEM to explore what new structures are apparent in such sub-metric data.

#### **5.4.1. Interpretation of lava flow surfaces**

In Fig. 5.7 we compare the distal section of an 'a'a flow system using the 20-cm and 1-m data. Because the spatial scale of roughness is less than 1-m, only in the 20-cm derived products we acquire a sense of roughness and micro-structure. The texture of the 20-cm openness down map (Fig. 5.7e and Fig. 5.8) in particular reveals three classes of roughness: relatively smooth (therefore fine grained); rough (coarse grained); and spotty (scattered large blocks). Next, we see that the detail of surface structure allows the fractal form of the folds, which involve folding scales from a few meters to tens of meters, to be resolved. For example, the frontal fold in the image of Fig. 5.7 and Fig. 5.8 is about 20 m wide. However, cross-flow this develops into a double-fold system each of which is 10 m wide. At the right bank we have at-least four components to the fold, as revealed only in the 20-cm openness down map. The 20-cm SVF map (Fig. 5.7c) reveals that the crests of the folds are rougher than the troughs. Reference to the 20-cm shaded relief confirms that fold crests are dominated by finer-grained material than the troughs, the troughs being blockier (Fig. 5.7a).

#### **5.4.2 Crust structures: a tripartite classification and flow regime association**

The new combination of 3-cm orthophotos and 20-cm DEM allows us to define three types of crust structure and relate them to positions within a channel-fed 'a'a flow system. These crust structures are: (i) flow parallel shear-lines; (ii) raft zones; and (iii) folded zones (Fig. 5.5 and Fig. 5.8). Each are associated with different spatial distributions of cracking, roughness and clast size, and characterize different flow regimes.

Flow parallel shear-lines are found at the channel edges. These structures are long, narrow continuous depressions in which cracking is intense and clasts sizes are intermediate between the small clasts of the levee wall and the larger clasts of the channel (Fig. 5.5c and Fig. 5.8). Where

levees are well-formed and distinct, these shear-lines run along the base of the levee inner-wall, and are typically less than 2 m wide and 0.25 m deep. Given their location, they must result from intense shearing between the moving channel lava and the static levee lava. In zones where initial levees are just beginning to form, these subtle features are the only geomorphological marker that delimits the moving lava from the stagnant marginal lava. As Lipman and Banks (1987) pointed out, across this distal “transitional” channel zone the channel-levee boundary can be indistinct because the channel is, in effect, brim full and the levees have no positive expression. These linear features are thus extremely useful in delimiting the channel in the distal reach of the flow system, where their topographic subtleness means that it is generally the crack map that identifies these structures distally.

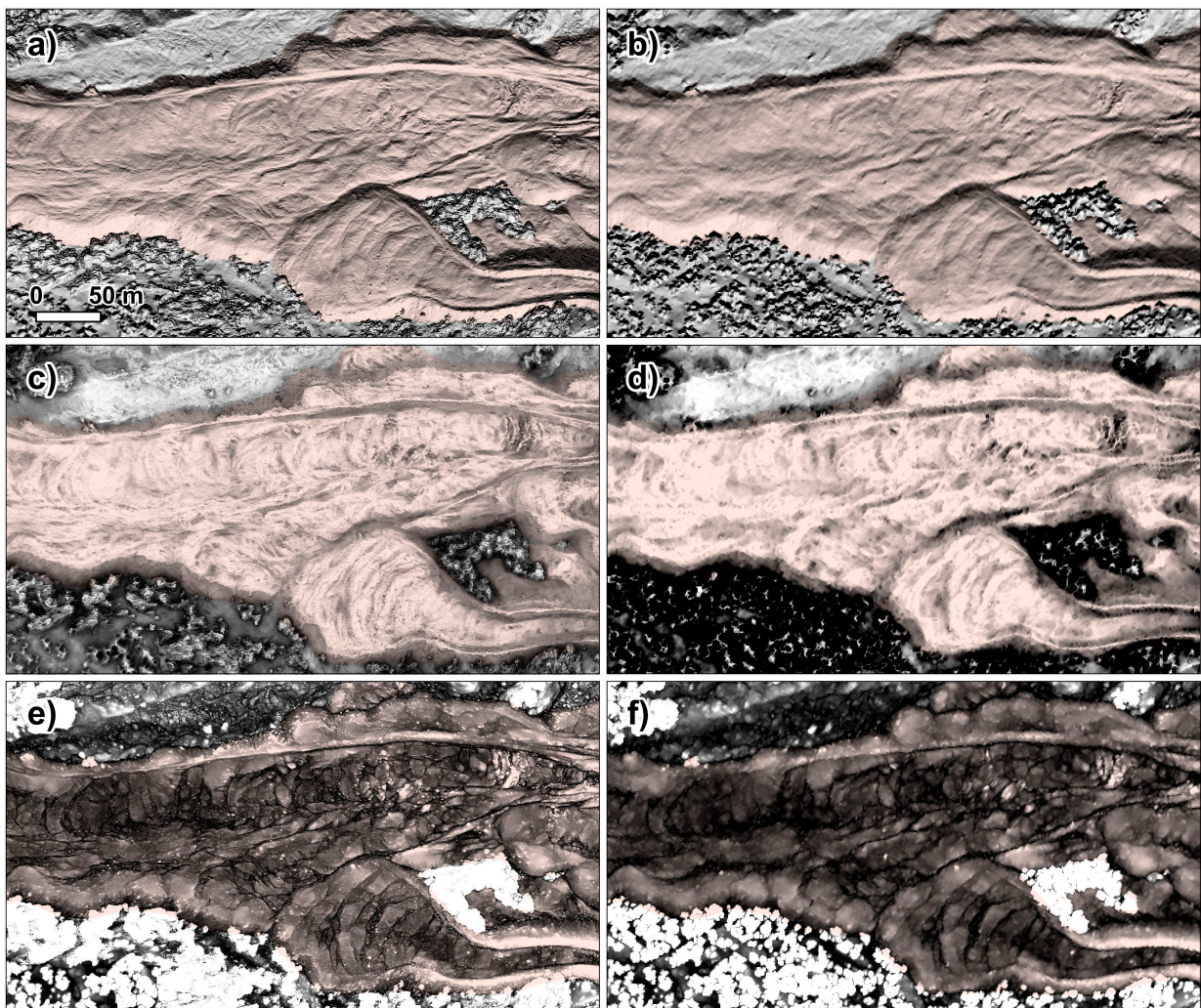


**Fig. 5.7** SfM-UAV and LiDAR DEMs qualitative comparison of a selected zone. Location of the selected zone is shown in Fig. 5.5. a, c and e) are the hillshaded map, Sky View Factor image (“channel-map”) and openness down image (“crack-map”) of a selected area derived from the 20 cm DEM; b, d and f) are the same maps derived from the 1 m DEM.

Rafts generally form as the system changes from a stable to a transitional channel regime. Over this zone, the channel broadens significantly. In our case, the channel broadens, over a distance of 170 m, from 8 m at the exit of the stable channel to 70 m in the transitional channel. Rafts are only apparent in the openness down map (Fig. 5.7e), being characterized by topographically higher poorly cracked areas, surrounded by lower, heavily cracked areas. Dimensions are up to 10 m, and raft distributions resemble patterns created by pahoehoe slab breakup (e.g. Guest and Stofan, 2005). Close to the levee, raft long axes are orientated down-flow; but towards the channel-center orientations are random. We interpret these rafts as being formed by break-up of crust zones, previously moving in a coherent manner in the narrow proximal channel reach, as the flow exits the stable channel and enters a much wider channel reach.

Folded zones involve arcuate, cross-flow ridges with their apexes pointing down-flow. They are repeated structures involving ridges of relatively small clasts with low degrees of cracking separated by depressions of coarser-grained breccia with high degrees of cracking. Our ridges have wavelengths of 10 m and amplitudes of 1 m. They are found towards the flow front, and form down-flow of the raft zones. We interpret them as being “ogives” (Cas and Wright 1988) associated with folding due to piling up of lava behind a static or slowly moving flow front (Gregg et al., 1998). They are thus associated with zones where forward motion of the flow front has ceased, or has significantly decreased, but where flow has continued to be supplied into the back of the distal section of the system so as to cause deformation.

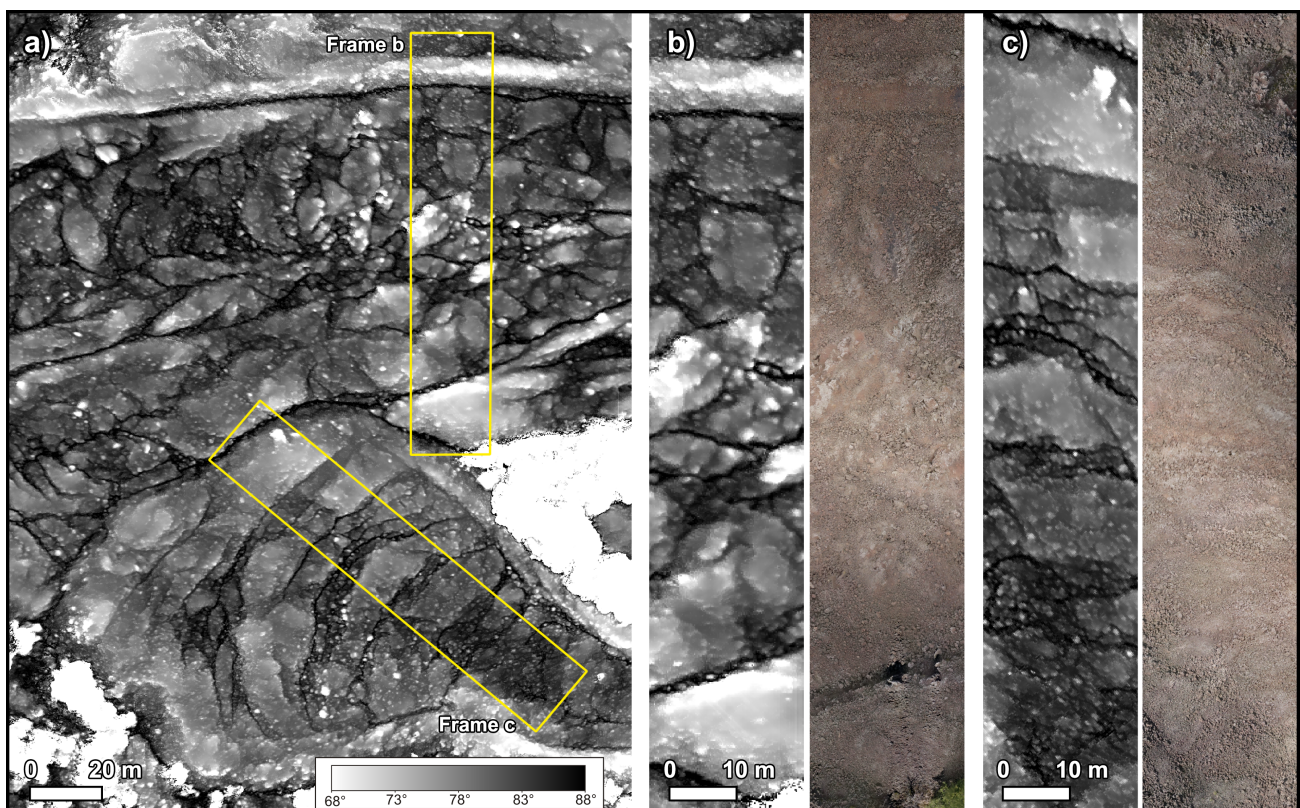


**Fig. 5.8** Openness down map of a selected area including a dispersed flow and lava channel of two different flows, calculated from the SfM-UAV DEM. a) Overview of the selected area show the presence of blocks at different size; b) Openness down map (left side) at major scale in which it is possible distinguish three classes of blocks. Orthomosaic (right) shows different information highlighting the presence various grain size on the lava surface; and c) Openness map (left) and orthomosaic (right) of a dispersed flow.

### 5.4.3 Qualitative analysis of surface folds

Lava surface folding involves surface-parallel shortening, and will not occur unless the viscosity of the fluid decreases with depth (Gregg and Fink 2000; Lescinsky and Merle 2005). Surface folds are common on lava flows of all compositions and they range in amplitude ( $A$ ) and wavelength ( $\lambda$ ) from centimeters (in pahoehoe flows) to tens or hundred meters (in obsidian flows). Wavelengths of folding depend primarily on the compressive stresses, temperature profile of the flow, and the viscosity and density of the lava (Fink and Fletcher 1978; Fink 1980). Surface folds can be characterized using high-spatial resolution DEMs either as linear transects along the flow axis or by generating spectrograms via Fourier analysis (Lescinsky et al., 2007; Cashman et al., 2013).

Fourier transforms of vertical profiles can be used to determine the frequencies (and  $\lambda$ ) of sinusoidal patterns present in the data. However conventional Fourier transforms are not able to determine the location along the profile of the component sinusoids, but instead give an “average” spectrum for the entire data set (Lescinsky et al., 2007). The  $S$ -transform method allows local spectral analysis to provide local values of amplitude and phase of sinusoidal spatial components, allowing local structure and patterns to be identified. The spatial component of the  $S$ -transform is obtained by multiplying the spatial data with a moving Gaussian window and by determining the Fourier transform for every point (Stokwell et al., 1996; Lescinsky et al., 2007). The Fourier transform is given by:

$$F(k) = \int_{-\infty}^{+\infty} f(x)e^{-2\pi xk} dx \quad 5.1$$

where  $k$  represents frequency,  $x$  the distance,  $f(x)$  the given data series, and  $F(k)$  the Fourier transform. The one-dimensional  $S$ -transform is given by:

$$S(k, u) = \int_{-\infty}^{+\infty} f(x) \left\{ \frac{|k|}{\sqrt{2\pi}} e^{-[(u-x)^2 k^2]/2} \right\} e^{-2\pi xk} dx \quad 5.2$$

where  $u$  is the location within the profile, and  $S(k,u)$  corresponds to the calculated  $S$ -spectrum coefficients. The term within the curly brackets is the local Gaussian window at  $x$ . Additional details on the derivation and use of the  $S$ -transform is described by Stockwell et al., (1996) and Lescinsky et al. (2007). Because the range of  $\lambda$  resolvable by the Fourier and  $S$ -transform is a function of the spatial resolution of the data, as well as of the length of the data profile, we compare the spectral analysis of two selected vertical profiles extracted from SfM and LiDAR data.

$S$ -spectrum plots of two selected topographic profiles (Figs. 5.9 and 5.10) reveal the presence of horizontal bands and patches of high coherence values. Significant features are identified as those that have higher coherence than surrounding values of similar wavelength, and which correspond to sinusoidal structures (Lescinsky et al., 2007). Synthetic sinusoids of appropriate  $\lambda$  and amplitude are apparent in the profiles of Figs. 5.9 and 5.10.  $S$ -spectrum plots of topographic profiles in the 20-cm data reveal numerous horizontal bands and patches of high coherence values that are absent in the 1-m topographic profiles.  $S$ -spectrum plots of the Fig. 5.9 transect reveal, for the LiDAR DEM, only one feature with  $\lambda = 8.0$  m. The same transect taken down the SfM DEM reveals two bands with different wavelengths ( $\lambda = 4.6$  and  $\lambda = 3.3$  m). These overlap at points along the profile, indicating a superposition of multiple structures and implying multiple formation events (Fink and Fletcher 1978). Fig. 5.10 gives the  $S$ -spectrum of a different profile over the 1974 lava flow. In this case in the SfM  $S$ -spectrum plot we find as many as three discrete formation events. The  $\lambda$  for these features are 2.6, 4.4, and 5.8 m. Conversely, in the LiDAR  $S$ -spectrum only one feature, with  $\lambda = 4.7$ , is identifiable (Fig. 5.10).

## 5.5. Hazard assessment applications

During an effusive eruption it is of paramount importance to map, in as precise and timely manner as possible, the location and direction of newly forming lava flows and their distribution systems. This is normally carried out through helicopter surveys, supported by airborne thermal camera operations or through satellite mapping (e.g., Harris et al., 2005b; Spampinato et al., 2011; Ganci et al., 2012a, 2012b; Harris 2013). However, ash emission from explosive activity at nearby eruptive fissures, or from smoke from forests burning at the lava flow front, can impede or even ground traditional airborne surveys, as during Etna's 2002-03 eruption (Andronico et al., 2005; Bonaccorso et al., 2016).

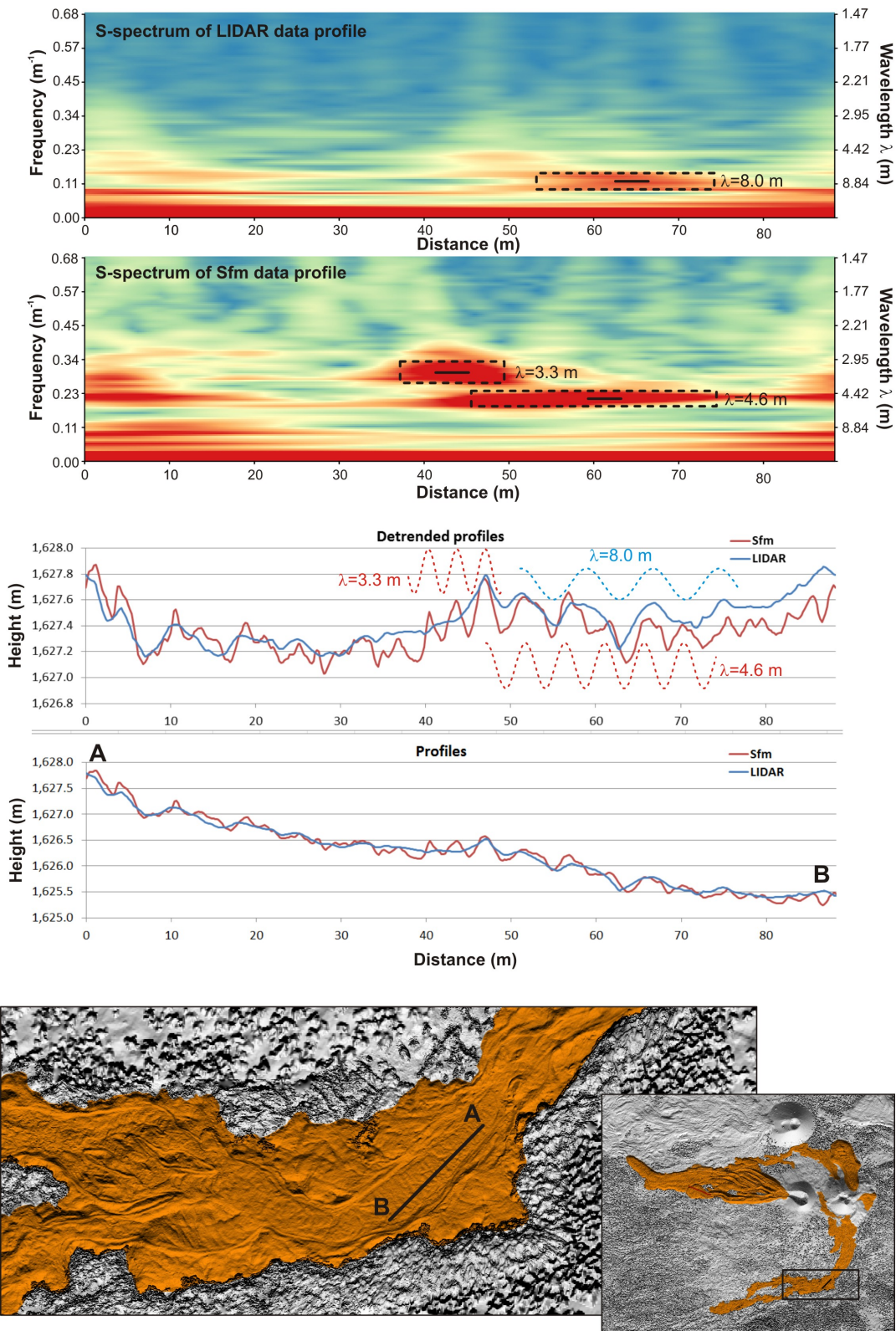


**Fig. 5.9a** 1974 lava flow profiles measured on DEMs with corresponding  $S$ -spectrum plots. Red and yellow in  $S$ -spectrum plots correspond to high coherence and blue to lower coherence. Dashed black lines on  $S$ -spectrum plots are used to highlight zone of high coherence; black lines correspond to specific wavelengths listed in plots.  $S$ -spectrum of LiDAR data shows one horizontal bands of high coherence,  $S$ -spectrum of the same profile taken on SfM DEM shows two horizontal bands of high coherence. In the detrended (for the mean slope) profile, dashed lines indicate synthetic sinusoids with appropriate wavelengths. and amplitudes. Topographic profiles reveal the different levels of details between the two DEMs.

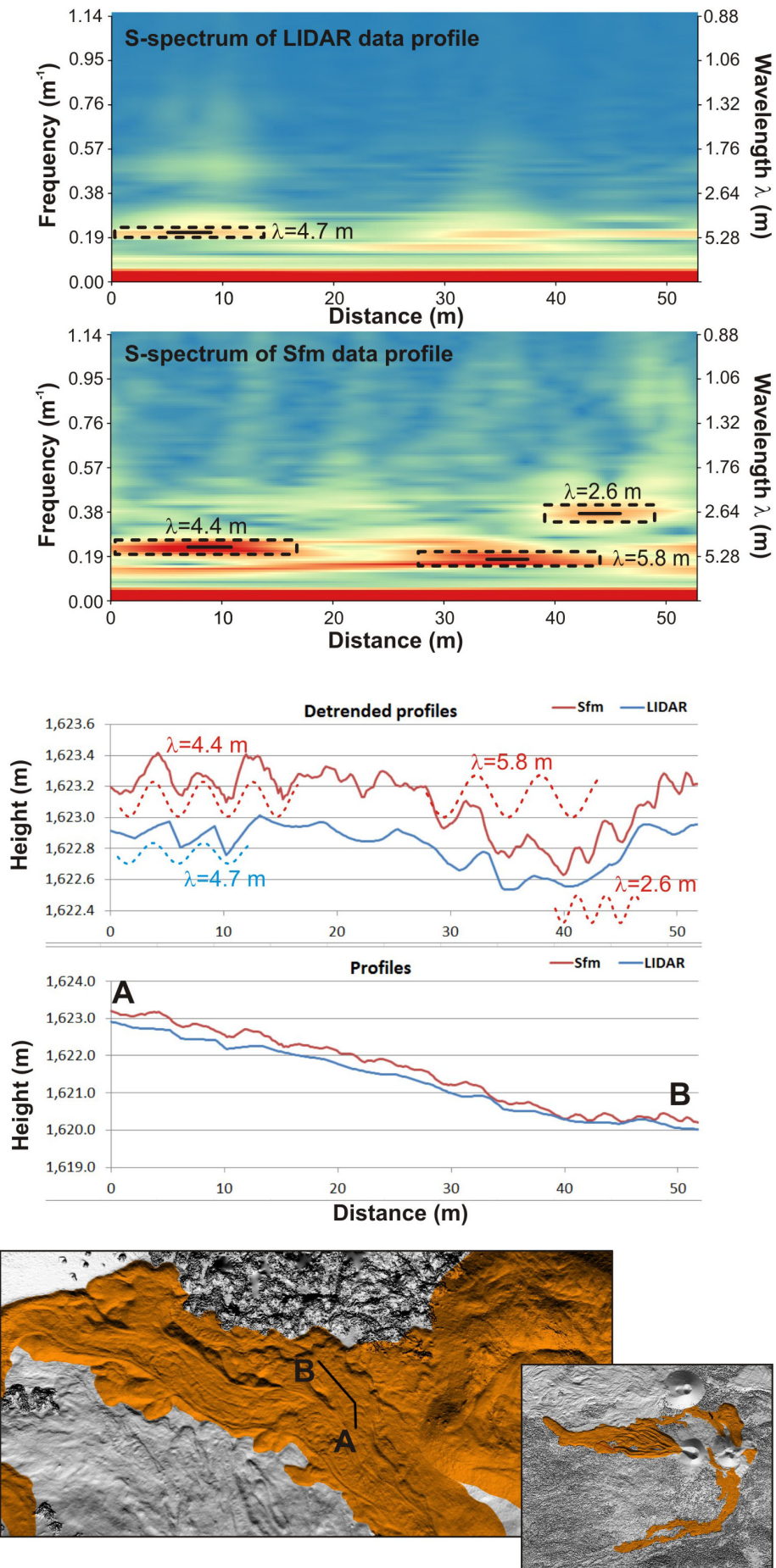


**Fig. 5.9b** 1974 lava flow profiles measured on DEMs with corresponding *S*-spectrum plots. Red and yellow in *S*-spectrum plots correspond to high coherence and blue to

lower coherence. Dashed black lines on *S*-spectrum plots are used to highlight zone of high coherence; black lines correspond to specific wavelengths listed in plots. *S*-spectrum of LiDAR data shows one horizontal bands of high coherence, *S*-spectrum of the same profile taken on SfM DEM shows three horizontal bands of high coherence. In the detrended profile, dashed lines indicate synthetic sinusoids with appropriate wavelengths and amplitudes. Topographic profiles show the different levels of details between the two DEMs.

Under such conditions the use of drones to obtain timely, and extremely high-spatial resolution, data of a developing lava flow field is an extremely attractive option. Such a data-supply allows immediate analysis of flow morphology and structure, as well as analysis of changes in flow geometry over short (10's of minutes) time scales. Reporting, based on such up-to-the-minute data, allows a scientist-in-charge (of monitoring an active site) to advise civil protection authorities, and then populations at risk, regarding the hazard to which they are exposed, and to provide updates on a regular basis. What's more, the drone-based platform provides a low-cost, flexible option (in terms of deployment, as well as spatial and temporal resolution), which can be deployed as needed with low-risk to those involved with implementing the observation tasks.

Take the following scenario. (1) We obtain a SfM-UAV-derived DEM in which we detect shear-lines, like those observed in [Fig. 5.7](#), in a just-started eruption. We know that such structures form when a sheet flow becomes channelized. (2) Given that a channel focuses lava towards vulnerable populations more efficiently than sheet flow, this represents a concern; so that we need to know the development, orientation, dimensions and extension (with time) of such features. Thus, (3) we track the evolution of the supply-system, carrying out frequent surveys by drone to obtain continuously-updated DEMs to detect and track the changes in position, orientation and size of channels comprising the distribution system. (4) Mature lava channel systems will further develop into lava tube systems, and the hazard increases as this now increases the potential for more distant communities to be inundated by lava. At this point, it becomes of paramount importance to map the distribution of breakouts and supply from ephemeral vents, because these will reveal the presence of well-fed lava tubes developing within the lava flow field (Calvari and Pinkerton 1998; Duncan et al., 2004) and the emission points.

SfM-UAV DEMs obtained on an hourly-to-daily basis allows the formation of channels to be detected and followed, and the rate of expansion of lava coverage and mass eruption rate to be calculated (Slatcher et al., 2015). When master tubes develop within the lava flow field, and when population centers are threatened by lava extending from a tube-fed system, civil protection authorities may even decide to intervene with mitigation measures aimed at breaking the tube and allow lava to flow on the surface further up-flow, such as has been done on Etna in the past (Barberi et al., 1993). Similar measures have been employed at erupting cones and channels, so as to attempt

to divert advancing lava (Harris 2014). Such intervention measures also require precise knowledge of the position, size and depth of structures, and of their distribution along the lava flow field. UAV and SfM methods allow fast, precise and frequent mapping of the entire lava flow field, or critical sections within it, to be carried out in safety and with great detail.

---

## Conclusions

---

Morphometric analysis provides crucial information for better understanding the dynamics of lava flow and emplacements. Precise, quantitative analyses of topographic changes related to effusive eruptions allow to infer key parameters for the assessment of lava flow hazards, namely lava volume, area and thickness and magma discharge rate. Lava flow morphometry is related to the flow properties when it was active. For this reason, measurements of channel-fed lava flow morphometric parameters are essential for defining the flow system and the associated flow dynamics. In addition, morphometric analysis provides benchmark, initial and boundary conditions, data that are indispensable for modelling lava flow, with tremendous implications for lava flow hazard assessment.

Multi-temporal, high-resolution topographic data can nowadays be considered the most suitable data for performing an accurate morphometric analysis of effusive products. In this thesis, we used multi-temporal high-resolution digital elevation models (DEMs) obtained by the airborne LiDAR system to carry out an extensive morphometric analysis on the Mount Etna (Italy) lava flows. The datasets used in this work were acquired during five different surveys performed in September 2004, September 2005, November 2006, June 2007 and September 2010. However, the acquisition of airborne LiDAR data is extremely expensive, mostly due to flight time costs, and this inhibits rapid deployment and high-frequency data collection, which are fundamental in active volcanic areas. In order to overcome these limits, in the last part of this work we tested the effectiveness to produce high spatial resolution DEMs over large areas by the combined use of Unmanned Aerial Vehicle (UAV) and Structure from Motion method (SfM), which guarantees low acquisition costs and rapid deployment in case of eruption.

The difference between the 2005 and 2004 LiDAR-DEMs showed a combined volume gain of  $\sim 62.2 \pm 1.2 \times 10^6 \text{ m}^3$  for an identified total area covered by volcanic products of  $\sim 2.8 \times 10^6 \text{ m}^2$ . The average thickness was 22 m, with a maximum thickness reaching 90 m. The volume gain is completely ascribed to the 2004-05 eruption. There was no evidence of summit activity among the two LiDAR surveys, apart from isolated explosions at Voragine in October 2004. However, the first

LiDAR survey was conducted after the onset of the eruption. The volume of volcanic product emitted before the 2004 survey was calculated by differentiating the 2004 DEM and the 1998 10 m TINITALY DEM. The measured final volume of the 2004-05 lava flow field results to be  $\sim 63.3 \pm 1.4 \times 10^6 \text{ m}^3$  for a mean eruption rate of  $\sim 4.1 \pm 0.1 \text{ m}^3 \text{ s}^{-1}$ . Our volume estimations are consistent with the measurements of Del Negro et al. (2015), who found a volume of  $62.3 \times 10^6 \text{ m}^3$  by differentiating pre- and post-DEMs obtained from different sources. Conversely, the volumes here calculated are significantly higher than those from Neri and Acocella (2006), who measured a volume gain of  $\sim 40 \times 10^6 \text{ m}^3$ .

The difference between the 2007 and 2005 LiDAR-DEMs for the only Valle del Bove showed a combined volume gain of  $\sim 42.0 \pm 3.1 \times 10^6 \text{ m}^3$  ascribed mainly to three phases of the activity: July 2006, September-December 2006, and March-May 2007. The volume of the July 2006 eruptive phase was estimated at  $\sim 4 \times 10^6 \text{ m}^3$  (Neri et al., 2006; Vicari et al., 2009), and the volume of products erupted during the paroxysms in spring 2007 at  $\sim 4.5 \times 10^6 \text{ m}^3$ . The resulting volume of lava emplaced on the eastern flank between September and December 2006 is then  $\sim 33.5 \pm 4 \times 10^6 \text{ m}^3$ . Considering also the contribution of the south lava field, the total inferred volume of the 2006 eruption is  $\sim 38 \pm 5 \times 10^6 \text{ m}^3$ . The total volume computed for the 2006 eruption (July-December) is about twice the previously published volume estimates based on field observations (Behncke et al., 2008). Furthermore, the data obtained during the November 2006 LiDAR survey permit to obtain a “snapshot” of the dimensions of the eruption that was underway at that time and also provide a tool to observe, at very high resolution, the dynamics of an active compound lava flow field. What is evident from the comparison of the 2006-2005 and 2007-2006 DEM difference maps is that the 2006 eruption reached its peak after the mid-November survey.

The difference between the 2007 and 2010 LiDAR-DEMs shows a combined volume gain of  $86.4 \pm 2.1 \times 10^6 \text{ m}^3$  for an identified total area covered by volcanic products of  $6.86 \text{ km}^2$ . Comparison of the 2007 and 2010 DEMs indicates that the 10 May 2008 paroxysm at the proto-NSEC was an outstanding event for the high volume of lava emitted in 4 h. While much of this lava flow was buried by the subsequent lavas of the 2008–2009 flank eruption, it was possible to map the area, thanks to a helicopter survey carried out less than a day before the onset of the flank eruption. For the surviving portion of the lava flow, the comparison of the 2007 and 2010 DEMs reveals an average thickness of 3 m, which, if applied to the entire mapped area of the flow, yields a volume of  $5.73 \times 10^6 \text{ m}^3$ . Subtraction of the lavas of the September 2007 to May 2008 paroxysms from the total volume of lava flows resulting from the comparison of the two DEMs allows to define more precisely the volume of the 2008–2009 flank eruption, which thus far has been estimated separately on the basis of satellite or field data. The volume is  $74.01 \pm 2.46 \times 10^6 \text{ m}^3$ , not very different from the more approximate volume estimated at  $77 \times 10^6 \text{ m}^3$  by Neri et al., (2011) based on field data and quite close to the dense rock equivalent volumes previously derived from

satellite data (e.g.,  $61 \times 10^6 \text{ m}^3$  by Ganci et al., 2012 and  $68 \times 10^6 \text{ m}^3$  by Harris et al., 2011). Based on our volume calculation, the average effusion rate of the 2008–2009 flank eruption was thus  $\sim 2 \text{ m}^3 \text{ s}^{-1}$ . The average thickness of the 2008–2009 lava flow-field was 14 m, but locally the thickness exceeded 50 m.

The precise determination of eruptive volumes and eruption rates is of great significance, because it renders a realistic impression of the volcano and its dynamics. It can be checked against data acquired with other methods to evaluate their accuracy and improve their application for future eruptions. The final outcome is a more complete and precise understanding of the potential hazard and impact of future eruptions and their likelihood of invading populated areas downslope from the Valle del Bove.

The same LiDAR dataset used for volume calculation was used in this work for an extensive morphometric analysis of selected channel-fed lava flows. Morphometric analysis of lava flows implies to detect and to delineate specific morphometric elements, i.e. flow base, levees and channel bed base. This can be everything but easy because of the extreme complexities of volcanic areas, which are characterized, for example, by the superimposing of lava flows, coalescent cones and volcanoes, huge ash fallout and, last but not least, if active, they are often dramatically changed by new eruptions. Mapping lava flows is particularly difficult when visualized as hillshaded map, because their linear and orientated shapes may be displayed in a different manner depending on the direction of illumination used. For this reason, we had to find more informative maps capable of enhancing specific lava flow elements. Digital Elevation Models permit the extraction of many different parameters, starting from a single matrix of elevation values. We performed a review of well-known and less common DEM-derived parameters such as hill-shading, slope and aspect, curvature, roughness, Sky View Factor (*SVF*), openness, and Red Relief Image Maps (RRIM). Since several of them can have similar or almost the same informative content, we were also produced a correlation matrix for rapidly detecting which parameters were correlated and which are not. In order to have the most uncorrelated content from a DEM, the following parameters should be produced: various type of hill-shading, slope, a curvature, a *TPI* with high *R*, roughness, negative openness, openness and a choice among *SVF*, *SVF2* and openness up. From this analysis it results that the base of the flow and the base of lava channels, characterized by a particular slope break, can be easily detected using the openness down map. Otherwise *SVF*, either alone or combined in RRIM, is very useful to distinguish volcanic features that are slightly raised with respect to their surroundings, since it enhances the perception of the relative height of surface elements. Uniform diffuse sky illumination of *SVF* is actually hill-shading but it eliminates the azimuth biases and also enhances the perception of the relative height of surface elements. Since *SVF* takes high values on crests and ridges, it helps to detect and map the levees of lava channels and to distinguish among superimposed channels. It is worth noting that openness down is uncorrelated with *SVF* parameters.

A large number of very accurate morphometric parameters were extracted from eleven channel-fed lava flows emitted during the 2006 and 2007-09 Etna eruptions and imaged by the 2007 and 2010 LiDAR DEMs. The morphometric analysis also involved the 2005 LIDAR DEM as pre-existing topography for the 2006 flows. In this work, for the first time, we were able to provide large amounts of data about pre-emplacement slope without interpolating the pre-existing topography under the flow. The morphometric analysis of selected lava flows is conducted through a semi-automatic procedure that measures the parameters over DEMs and that implies the tracking of surface-specific elements such as flow axes and base, levee ridges and edges of the channel-bed. Tracking is supported by the automatic detection of surface-specific points and is performed using the sky view factor and openness as maps for a most effective DEM visualization. The results of morphometric analysis support an inverse relation between the slope and channel width, at least for large-scale observation, even if there may be some exceptions. This relation stresses the importance of topography for predicting the path of the flow and for investigating the emplacement dynamics. The average slope of levees is consistent with the pre-existing slope, namely it can be used when the slope of topography cannot be measured, which occurs most of the time. Channel and channel-bed widths have to some extent the same trends, i.e. the local minima and maxima are generally aligned. Channel widths are usually much wider than the levees, while the channel-bed width can be greater, smaller or equal to the height of levees. The channels tend to be largely symmetrical.

Chapter 2 reports that Mount Etna in only six years emitted  $\sim 190 \times 10^6 \text{ m}^3$  of eruptive products. This calls for frequent DEM updating, at least after the main eruptive events. The airborne LIDAR system is able to provide topographic data with proper coverage and spatial resolution, but mission deployment is rather costly, thus prevent a frequent employment of this technology. For this reason, we tested the performance of a system that uses an Unmanned Aerial Vehicle (UAV) platform equipped with a consumer grade camera for acquiring photographs and Structure from Motion (SfM) method to generate a high-resolution DEM of the 1974 Mount Etna lava flow field.

For monitoring and surveillance of volcanic terrains, UAVs are ideal platforms for acquiring photogrammetric data to map structures that inform on lava flow emplacement dynamics. Vehicles, otherwise known as drones, allow surveys of inaccessible, kilometer scale areas, with low cost and minimal hazard to personnel. This is a distinct advantage over a volcanic terrain where time scales of change are fast (minutes to hours), involve vertical spatial scales of millimeters to meters, and are extremely hazardous to approach. This is an argument that has been applied for several decades, but the advent of the drone means that an operator can truly update the topography every few minutes for an outlay of just a few thousand euro (this being the price of the drone, the camera, and the autopilot software). Better, easy-to-use SfM-based software allows to update a pre-existing DEM, or to create a new DEM, in a timely fashion. The new UAV-mounted digital camera capability, coupled with SfM methods, permitted to generate a 20-cm resolution DEM for the 1974 Mount

Etna lava field, allowing analysis of sub-meter-scale features over an area of several square kilometers. The 20-cm resolution allowed morphometric analysis of lava surface features such as folds, blocks, and cracks in a manner that was not possible with the 1-m LiDAR-derived DEM. In addition, these data allowed us to further push the spectral analysis of surface folding over a much larger spectrum of frequencies than is possible using a LiDAR-derived DEM. In this regard, geometry of surface folding can be used to constrain the thickness and viscosity of the folded layer (from the fold wavelength) and compressional stress (from the fold amplitude).

In conclusion, high-resolution Digital Elevation Models provide the means to infer a large amount of key parameters that can be used for investigating the dynamics of lava flow and emplacements, and for the assessment of associated hazards. Essential for an effective morphometric analysis of lava flow is the availability of pre-emplacment topography. In an active volcanic area, this calls for a continuous updating of high-resolution topography. It is thus crucial to invest in technologies and research able to provide high-resolution DEMs in a short time and at reasonable costs.

---

## References

---

- Acocella V. and Neri M. (2003). What makes flank eruptions? The 2001 Mount Etna eruption and its possible triggering mechanisms. *Bulletin of Volcanology* 65, 517–529.
- Akima H. (1978). A method of bivariate interpolation and smooth surface fitting for irregularly distributed data points. *ACM Transactions on Mathematical Software (TOMS)* 4(2), 148-159.
- Andronico D., Branca S., Calvari S., Burton M., Caltabiano T., Corsaro R.A., Del Carlo P., Garfi G., Lodato L., Miraglia L., Muré F., Neri M., Pecora E., Pompilio M., Salerno G. and Spampinato L. (2005). A multi-disciplinary study of the 2002–03 Etna eruption: insights into a complex plumbing system. *Bulletin of Volcanology* 67, 314–330.
- Andronico D. and Lodato L. (2005). Effusive Activity at Mount Etna Volcano (Italy) During the 20th Century: A Contribution to Volcanic Hazard Assessment. *Natural Hazards* 36, 407–443.
- Andronico D., Scollo S., Cristaldi A. and Caruso S. (2008). The 2002-03 Etna explosive activity: Tephra dispersal and features of the deposit. *Journal of Geophysical Research* 113, B04209.
- Andronico D., Scollo S., Cristaldi A. and Ferrari F. (2009). Monitoring ash emission episodes at Mt. Etna: the 16 November 2006 case study. *Journal of Volcanology and Geothermal Research* 180 (2-4), 123–134.
- Bagnardi M., González P.J. and Hooper A. (2016). High-resolution digital elevation model from tri-stereo Pleiades-1 satellite imagery for lava flow volume estimates at Fogo Volcano. *Geophysical Research Letters* 43(12), 6267–6275.
- Bailey J.E., Harris A.J., Dehn J., Calvari S. and Rowland S.K. (2006). The changing morphology of an open lava channel on Mt. Etna. *Bulletin of Volcanology* 68(6), 497–515.
- Baltsavias E.P. (1999a). Airborne laser scanning: basic relations and formulas. *ISPRS Journal of photogrammetry and remote sensing*, 54(2), 199–214.
- Baltsavias E.P. (1999b). A comparison between photogrammetry and laser scanning. *ISPRS Journal of photogrammetry and Remote Sensing*, 54(2), 83–94.
- Baltsavias E.P. (1999c). Airborne laser scanning: existing systems and firms and other resources. *ISPRS Journal of Photogrammetry and Remote Sensing* 54(2), 164–198.

- Barberi F., Carapezza M.L., Valenza M. and Villari L. (1993). The control of lava flow during the 1991-1992 eruption of Mt. Etna. *Journal of Volcanology and Geothermal Research* 56, 1–34.
- Behncke B., Neri M. and Nagay A. (2005). Lava flow hazard at Mount Etna (Italy): New data from a GIS-based study, in *Kinematics and Dynamics of Lava Flows*, edited by M. Manga and G. Ventura, *Spec. Pap. Geol. Soc. Am.*, 396, 189–208.
- Behncke B., Neri M., Pecora E. and Zanon V. (2006). The exceptional activity and growth of the Southeast Crater, Mount Etna (Italy), between 1996 and 2001. *Bulletin of Volcanology* 69, 149–173.
- Behncke B., Calvari S., Giammanco S., Neri M. and Pinkerton, H. (2008). Pyroclastic density currents resulting from the interaction of basaltic magma with hydrothermally altered rock: an example from the 2006 summit eruptions of Mount Etna, Italy. *Bulletin of Volcanology* 70(10), 1249-1268.
- Behncke B., Falsaperla S. and Pecora, E. (2009). Complex magma dynamics at Mount Etna revealed by seismic, thermal, and volcanological data. *Journal of Geophysical Research, Solid Earth* 114(B3).
- Behncke B., Branca S., Corsaro R.A., De Beni E., Miraglia L. and Proietti C. (2014). The 2011–2012 summit activity of Mount Etna: birth, growth and products of the new SE crater. *Journal of Volcanology and Geothermal Research* 270, 10–21.
- Behncke B., Fornaciai A., Neri M., Favalli M., Ganci G. and Mazzarini F. (2016). Lidar surveys reveal eruptive volumes and rates at Etna, 2007–2010. *Geophysical Research Letters* 43(9), 4270–4278.
- Bonaccorso A., Cannata A., Corsaro R.A., Di Grazia G., Gambino S., Greco F., Miraglia L. and Pistorio A. (2011a). Multidisciplinary investigation on a lava fountain preceding a flank eruption: The 10 May 2008 Etna case. *Geochem. Geophys. Geosyst.* 12, Q07009.
- Bonaccorso A., Bonforte A., Calvari S., Del Negro C., Di Grazia G., Ganci G., Neri M., Vicari A. and Boschi E. (2011b). The initial phases of the 2008–2009 Mount Etna eruption: A multidisciplinary approach for hazard assessment. *Journal of Geophysical Research* 116, B03203.
- Bonaccorso A., Calvari S. and Boschi E. (2016) Hazard mitigation and crisis management during major flank eruptions at Etna volcano: reporting on real experience. In: Harris AJL, De Groeve T., Garel F., Carn S.A. (Editors) *Detecting, Modelling and Responding to Effusive Eruptions*, Geological Society London, Special Publications (IAVCEI) Series 426.
- Bonforte A., Guglielmino F. and Puglisi G. (2013). Interaction between magma intrusion and flank dynamics at Mt. Etna in 2008, imaged by integrated dense GPS and DInSAR data. *Geochem. Geophys. Geosyst.* 14, 2818–2835.

- Bottari A., Lo Giudice E., Patanè G., Romano R. and Sturiale, C. (1975). L'eruzione etnea del gennaio-marzo 1974. *Riv. Min. Sic* 154(156), 175-198.
- Branca S. and Del Carlo P. (2004). Eruptions of Mt. Etna during the past 3200 years: A revised compilation integrating the historical and stratigraphic records, in *Mt. Etna: Volcano Laboratory, Geophys. Monogr. Ser.*, vol. 143, edited by A. Bonaccorso et al., pp. 1–27, AGU, Washington, D.C.
- Buckley A., Hurni L., Kriz K., Patterson T. and Olsenholler J. (2004). Cartography and visualization in mountain geomorphology. *Geographic Information Science and Mountain Geomorphology*. Springer, Praxis, Chichester, UK, 253–287.
- Burton M.R., Neri M., Andronico D., Branca S., Caltabiano T., Calvari S., Corsaro R.A., Del Carlo P., Lanzafame G., Lodato L., Miraglia L., Salerno G. and Spampinato L. (2005). Etna 2004-05: An archetype for geodynamically-controlled effusive eruptions. *Geophysical Research Letter* 32, L09303.
- Calvari S. and Pinkerton H. (1998). Formation of lava tubes and extensive flow field during the 1991-93 eruption of Mount Etna. *Journal of Geophysical Research* 103(B11), 27291–27302.
- Calvari S. and Pinkerton H. (1999). Lava tube morphology on Etna and evidence for lava flow emplacement mechanisms. *Journal of Volcanology and Geothermal Research* 90, 263–280.
- Carracedo J.C., Rodríguez Badiola E., Guillou H., Paterne M., Scaillet S., Pérez Torrado F.J., Paris R., Fra-Paleo U. and Hansen A. (2007). Eruptive and structural history of Teide Volcano and rift zones of Tenerife, Canary Islands. *Geol. Soc. Amer. Bull.* 119 (9), 1027–1051.
- Carrivick J.L., Smith M.W. and Quincey D.J. (2016). *Structure from Motion in the Geosciences*. John Wiley & Sons.
- Cas R.A.F. and Wright J.V. (1988). Lava flows In *Volcanic Successions Modern and Ancient* 58–91. Springer Netherlands.
- Cashman K.V., Thornber C. and Kauahikaua J. (1999). Cooling and crystallization of lava in open channels, and the transition of Pāhoehoe Lava to 'A'ā. *Bulletin of Volcanology* 61, 306–323
- Cashman K.V., Soule S.A., Mackey B.H., Deligne N.I., Deardorff N.D. and Dietterich H.R. (2013). How lava flows: New insights from applications of lidar technologies to lava flow studies. *Geosphere* 9(6), 1664–1680.
- Cayley A. (1859). On Contour Lines and Slope Lines. *Philosophical Magazine: A Journal of Theoretical, Experimental and Applied Physics* 18, 264–268.
- Chevrel M.O., Platz, T., Hauber E., Baratoux D., Lavallée Y. and Dingwell D.B. (2013). Lava flow rheology: a comparison of morphological and petrological methods. *Earth and Planetary Science Letters* 384, 109–120.

- Chiba T., Kaneta S.I. and Suzuki Y. (2008). Red relief image map: new visualization method for three dimensional data. *The International Archives of the Photogrammetry, Remote Sensing and Spatial Information Sciences* 37, 1071–1076.
- Clarke K.C. (1988). Scale-based simulation of topographic relief. *The American Cartographer* 15(2), 173–181.
- Coblentz D. and Karlstrom K.E. (2011). Tectonic geomorphometrics of the western United States: Speculations on the surface expression of upper mantle processes. *Geochemistry, Geophysics, Geosystems* 12(11).
- Corsaro, R.A. and Miraglia, L. (2005). Dynamics of 2004 – 2005 Mt. Etna effusive eruption as inferred from petrologic monitoring. *Geophys. Res. Lett.* 32, L13302.
- Corsaro R.A. and L. Miraglia (2014). The transition from summit to flank activity at Mt. Etna, Sicily (Italy): Inferences from the petrology of products erupted in 2007–2009. *Journal Volcanology and Geothermal Research* 275, 51–60.
- Corsaro R.A., Métrich N., Allard P., Andronico D., Miraglia L. and Fourmentraux C. (2009). The 1974 flank eruption of Mount Etna: An archetype for deep dike-fed eruptions at basaltic volcanoes and a milestone in Etna's recent history. *Journal of Geophysical Research, Solid Earth* 114(B7).
- Crown D.A. and Baloga S.M. (1999). Pahoehoe toe dimensions, morphology, and branching relationships at Mauna Ulu, Kilauea Volcano, Hawai'i. *Bulletin of Volcanology* 61(5), 288–305.
- Daneš Z.F. (1972). Dynamics of lava flows. *Journal of Geophysical Research* 77(8), 1430–1432.
- De Beni E., Behncke B., Branca S., Nicolosi I., Carluccio R., D'Ajello Caracciolo F. and Chiappini M. (2015). The continuing story of Etna's New Southeast Crater (2012–2014): Evolution and volume calculations based on field surveys and aerophotogrammetry. *Journal Volcanology Geothermal Research* 303, 175–186.
- Del Negro C., Cappello A. and Ganci, G. (2016). Quantifying lava flow hazards in response to effusive eruption. *Geological Society of America Bulletin* 128(5-6), 752-763.
- Deardorff N.D. and Cashman K.V. (2012). Emplacement conditions of the c. 1,600-year bp Collier Cone lava flow, Oregon: a LiDAR investigation. *Bulletin of volcanology* 74(9), 2051–2066.
- Dietterich H.R., Soule S.A., Cashman K.V. and Mackey BH (2015). Lava Flows in 3D. *Hawaiian Volcanoes: From Source to Surface*, 483–505.
- Dietterich H.R. and Cashman K.V. (2014). Channel networks within lava flows: Formation, evolution, and implications for flow behavior. *Journal of Geophysical Research, Earth Surface* 119(8), 1704–1724.

- Dragoni M., Bonafede M. and Boschi E. (1986). Downslope flow models of a Bingham liquid: implications for lava flows. *Journal of Volcanology and Geothermal Research* 30(3-4), 305–325.
- Duncan A.M., Guest J.E., Stofan E.R., Anderson S.W., Pinkerton H. and Calvari S. (2004). Development of tumuli in the medial portion of the 1983 aa flow-field, Mount Etna, Sicily. *Journal of Volcanology and Geothermal Research* 132, 173–187.
- Eitel J.U., Höfle B., Vierling L.A., Abellán A., Asner G.P., Deems J.S. and Mandlbürger G. (2016). Beyond 3-D: The new spectrum of lidar applications for earth and ecological sciences. *Remote Sensing of Environment* 186, 372–392.
- El-Sheimy N., Valeo C. and Habib A. (2005). *Digital terrain modeling: acquisition, manipulation, and applications*. Artech House.
- Evans I.S. (1979). Statistical characterization of altitude matrices by computer. An integrated system of terrain analysis and slope mapping.
- Evans I.S. and Cox, N.J. (1999). Relations between land surface properties: altitude, slope and curvature. In: Hergarten, S., Neugebauer, H.J. (Eds.), *Process Modelling and Landform Evolution*. Springer, Berlin, pp. 13–45.
- Falsaperla S., Behncke B., Langer H., Neri M., Salerno G.G., Giammanco S., Pecora E. and Biale E. (2014). “Failed” eruptions revealed by pattern classification analysis of gas emission and volcanic tremor data at Mt. Etna, Italy. *Int. J. Earth. Sci.* 103, 297–313.
- Fara H.D. and Scheidegger A.E. (1963). An eigenvalue method for the statistical evaluation of fault plane solutions of earthquakes. *Bulletin of the Seismological Society of America* 53(4), 811–816.
- Farquharson J.I., James M.R. and Tuffen H. (2015). Examining rhyolite lava flow dynamics through photo-based 3D reconstructions of the 2011–2012 lava flowfield at Cordón-Caulle, Chile. *Journal of Volcanology and Geothermal Research* 304, 336–348.
- Favalli M., Fornaciai A. and Pareschi M.T. (2009). LIDAR strip adjustment: Application to volcanic areas. *Geomorphology* 111(3), 123–135.
- Favalli M., Fornaciai A., Mazzarini F., Harris A., Neri M., Behncke B., Pareschi M.T., Tarquini S., Boschi E (2010a). Evolution of an active lava flow field using a multitemporal LIDAR acquisition. *Journal of Geophysical Research, Solid Earth* 115(B11).
- Favalli M., Harris A.J., Fornaciai A., Pareschi M.T. and Mazzarini F. (2010b). The distal segment of Etna’s 2001 basaltic lava flow. *Bulletin of Volcanology* 72(1), 119–127.
- Favalli M., Tarquini S. and Fornaciai A. (2011). DOWNFLOW code and LIDAR technology for lava flow analysis and hazard assessment at Mount Etna. *Annals of Geophysics* 54, 5.
- Favalli M., Tarquini S., Fornaciai A. and Boschi, E. (2012a). Dispersion index of topographic surfaces. *Geomorphology* 153, 169–178.

- Favalli M., Fornaciai A., Isola I., Tarquini S. and Nannipieri L. (2012b) Multiview 3D reconstruction in geosciences. *Computers and geosciences* 44,168–176.
- Favalli M. and Fornaciai A. (2017), Visualization and comparison of DEM-derived parameters. Application to volcanic areas. Accepted to *Geomorphology*.
- Fink J.H. and Fletcher R.C. (1978). Ropy pahoehoe: Surface folding of a viscous fluid. *Journal of Volcanology and Geothermal Research* 4(1),151–170.
- Fink J. (1980). Surface folding and viscosity of rhyolite flows. *Geology* 8(5), 250–254.
- Florinsky I. (2016). *Digital terrain analysis in soil science and geology*. Academic Press.
- Fornaciai A., Behncke B., Favalli M., Neri M., Tarquini S. and Boschi, E. (2010b). Detecting short-term evolution of Etnean scoria cones: a LIDAR-based approach. *Bulletin of Volcanology* 72(10), 1209–1222.
- Fornaciai A., Bisson M., Landi P., Mazzarini F., Pareschi M.T. (2010a). A LiDAR survey of Stromboli volcano (Italy): Digital elevation model-based geomorphology and intensity analysis. *International Journal of Remote Sensing* 31(12), 3177–3194.
- Fornaciai A., Favalli M., Karátson D., Tarquini S. and Boschi E. (2012). Morphometry of scoria cones, and their relation to geodynamic setting: a DEM-based analysis. *J. Volcanol. Geotherm. Res.* 217/218, 56–72.
- Ganci G., Vicari A., Cappello A. and Del Negro C. (2012a). An emergent strategy for volcano hazard assessment: From thermal satellite monitoring to lava flow modeling. *Remote Sensing of Environment* 119, 197-207.
- Ganci G., Harris A.J.L., Del Negro C., Guehenneux Y., Cappello A., Labazuy P., Calvari S., Gouhier M. (2012b). A year of lava fountaining at Etna: Volumes from SEVIRI. *Geophysical Research Letters* 39, L06305.
- GRAFCAN (2009). *Mapa Topográfico de las Islas Canarias (1:5.000)*. Cartográfica de Canarias, Spain.
- Gregg T.K., Fink J.H. and Griffiths R.W. (1998). Formation of multiple fold generations on lava flow surfaces: Influence of strain rate, cooling rate, and lava composition. *Journal of Volcanology and Geothermal Research* 80(3), 281–292.
- Gregg T.K. and Fink J.H. (2000). A laboratory investigation into the effects of slope on lava flow morphology. *Journal of Volcanology and Geothermal Research* 96(3), 145–159.
- Griffiths R.W. (2000). The dynamics of lava flows. *Annual Review of Fluid Mechanics* 32(1), 477–518.
- Grosse P., van Wyk de Vries B., Euillades P.A., Kervyn M. and Petrinovic I.A. (2012). Systematic morphometric characterization of volcanic edifices using digital elevation models. *Geomorphology* 136, 114–131.

- Guest J.E. and Stofan E.R. (2005). The significance of slab-crustal lava flows for understanding controls on flow emplacement at Mount Etna, Sicily. *Journal of Volcanology and Geothermal research*, 142(3), 193–205.
- Harris A.J. and Rowland S. (2001). FLOWGO: a kinematic thermo-rheological model for lava flowing in a channel. *Bulletin of Volcanology* 63(1), 20–44.
- Harris A.J., Bailey J., Calvari S. and Dehn J. (2005a). Heat loss measured at a lava channel and its implications for down-channel cooling and rheology. *Geological Society of America Special Paper* 396, 125–146.
- Harris A.J., Dehn J., Patrick M., Calvari S., Ripepe M. and Lodato L. (2005b). Lava effusion rates from hand-held thermal infrared imagery: an example from the June 2003 effusive activity at Stromboli. *Bulletin of Volcanology* 68, 107–117.
- Harris A., Favalli M., Mazzarini F. and Pareschi M.T. (2007). Best-fit results from application of a thermo-rheological model for channelized lava flow to high spatial resolution morphological data. *Geophysical Research Letters* 34(1).
- Harris A.J., Favalli M., Mazzarini F., Hamilton C.W. (2009). Construction dynamics of a lava channel. *Bulletin of Volcanology* 71(4), 459–474.
- Harris A.J. and Rowland S.K. (2009). Effusion rate controls on lava flow length and the role of heat loss: a review. THORDARSON, T., SELF, S., LARSEN, G., ROWLAND, S. K. & HOSKULDSSON, A. (eds) *Studies in Volcanology: The Legacy of George Walker*. Special Publications of IAVCEI, 2, 33–51. Geological Society, London.
- Harris A., Steffke A., Calvari S. and Spampinato L. (2011). Thirty years of satellite-derived lava discharge rates at Etna: Implications for steady volumetric output. *Journal of Geophysical Research, Solid Earth* 116(B8).
- Harris A.J. (2013). *Thermal Remote Sensing of Active Volcanoes: A User's Manual*. Cambridge University Press. (Cambridge, UK): 728 p
- Harris A.J. (2014). Basaltic Lava Flow Hazard. In *Volcanic Hazards, Risks, and Disasters*.
- Hengl T. (2006). Finding the right pixel size. *Computers and Geosciences* 32(9), 1283–1298.
- Hengl T. and Evans, I.S. (2009). Mathematical and digital models of the land surface. In: Hengl, T., Reuter H.I. (Eds.), *Geomorphometry: Concepts, Software, Applications*. Elsevier, Amsterdam, pp. 31–63.
- Hengl T. and Reuter H.I. (2009). *Geomorphometry: Concepts, Software, Applications*. Elsevier, Amsterdam.
- Hiller J.K. and Smith M. (2008). Residual relief separation: digital elevation model enhancement for geomorphological mapping. *Earth Surf. Process. Landf.* 33, 2266–2276.

- Ho Y.X., Landy M.S. and Maloney L.T. (2006). How direction of illumination affects visually perceived surface roughness. *Journal of Vision* 6(5), 634–648.
- Hobson R.D. (1972). Surface roughness in topography: a quantitative approach. In R.J. Chorley (Ed.), *Spatial Analysis in Geomorphology*, Methuen & Co, London, pp. 221–245.
- Hon K., Kauahikaua J., Denlinger R. and Mackay K. (1994). Emplacement and inflation of pahoehoe sheet flows: Observations and measurements of active lava flows on Kilauea Volcano, Hawaii. *Geological Society of America Bulletin* 106, 351–370.
- Horn B.K.P. (1981). Hill shading and the reflectance map. *Proc. IEEE* 69 (1), 14–47.
- James F. and Roos M. (1977) MINUIT, CERN Program Library Entry D506.
- James M.R. and Robson S. (2012). Straightforward reconstruction of 3D surfaces and topography with a camera: Accuracy and geoscience application. *Journal of Geophysical Research: Earth Surface* 117(F3).
- James M.R. and Varley N. (2012). Identification of structural controls in an active lava dome with high resolution DEMs: Volcán de Colima, Mexico. *Geophysical Research Letters*, 39(22).
- James M.R. and Robson S. (2014). Sequential digital elevation models of active lava flows from ground-based stereo time-lapse imagery. *ISPRS Journal of Photogrammetry and Remote Sensing* 97, 160–170.
- Karátson D., Telbisz T. and Wörner G. (2012). Erosion rates and erosion patterns of Neogene to Quaternary stratovolcanoes in the Western Cordillera of the Central Andes: an SRTM DEM based analysis. *Geomorphology* 139, 122–135.
- Karátson D., Yepes J., Favalli M., Rodríguez-Peces M.J., Fornaciai A. (2016). Reconstructing eroded paleovolcanoes on Gran Canaria, Canary Islands, using advanced geomorphometry. *Geomorphology* 253, 123-134.
- Kauahikaua J., Cashman K.V., Mattox T.N., Heliker C.C., Hon K.A., Mangan M.T. and Thornber C.R. (1998). Observations on basaltic lava streams in tubes from Kilauea Volcano, island of Hawai'i. *Journal of Geophysical Research* 103(B11), 27303–27323.
- Kennelly P. J. (2008). Terrain maps displaying hill-shading with curvature. *Geomorphology*. 102(3), 567–577.
- Keszthelyi L. (1995). A preliminary thermal budget for lava tubes on the Earth and planets. *Journal of Geophysical Research* 100, 20411–20420
- Kilburn C.R. and Guest J.E. (1993). aa lavas of Mount Etna, Sicily. *Active lavas: monitoring and modelling*. UCL Press, London, 73-106.
- Kilburn C.R. (2004). Fracturing as a quantitative indicator of lava flow dynamics. *Journal of Volcanology and Geothermal Research* 132, 209-224.
- Kolzenburg S., Favalli M., Fornaciai A., Isola I., Harris A.J., Nannipieri L. and Giordano D. (2016). Rapid Updating and Improvement of Airborne LIDAR DEMs Through Ground-Based SfM 3D

- Modeling of Volcanic Features. *IEEE Transactions on Geoscience and Remote Sensing* 54(11), 6687–6699.
- Kuo W.L., Steenhuis T.S., McCulloch C.E., Mohler C.L., Weinstein D.A., DeGloria, S.D. and Swaney D.P. (1999). Effect of grid size on runoff and soil moisture for a variable-source-area hydrology model. *Water Resources Research*, 35(11) 3419–3428.
- Lescinsky D.T. and Merle O. (2005). Extensional and compressional strain in lava flows and the formation of fractures in surface crust. *Geological Society of America Special Papers* 396, 163–179.
- Lescinsky D.T., Skoblenick S.V. and Mansinha L. (2007). Automated identification of lava flow structures using local Fourier spectrum of digital elevation data. *Journal of Geophysical Research, Solid Earth* 112(B5).
- Lev E. and James M.R. (2014). The influence of cross-sectional channel geometry on rheology and flux estimates for active lava flows. *Bulletin of Volcanology* 76(7), 1–15.
- Li Z., Zhu C. and Gold, C. (2004). *Digital terrain modeling: principles and methodology*. CRC press.
- Lipman P.W and Banks N.G. (1987). AA flow dynamics, Mauna Loa 1984. *US Geol Surv. Prof. Pap.* 1350, 1527–1567.
- Lowe D (2004). Distinctive Image Features from Scale Invariant Keypoints. *International Journal of Computer Vision* 60(2), 91–110.
- Luhmann T., Robson S., Kyle S. and Boehm, J. (2014). *Close-range photogrammetry and 3D imaging*. Walter de Gruyter.
- Malin M.C. (1980). Lengths of Hawaiian lava flows. *Geology* 8(7), 306-308.
- Mark D.M. (1979). Phenomenon-based data-structuring and digital terrain modeling. *Geo-processing* 1(1), 27–36.
- Mattox T.N., Heliker C., Kauahikaua J. and Hon K. (1993). Development of the 1990 Kalapana Flow Field, Kilauea Volcano, Hawaii. *Bulletin of Volcanology* 55, 407–413.
- Mazzarini F., Pareschi M.T., Favalli M., Isola I., Tarquini S. and Boschi E. (2005). Morphology of basaltic lava channels during the Mt. Etna September 2004 eruption from airborne laser altimeter data. *Geophysical Research Letters* 32(4).
- Mazzarini F., Pareschi M.T., Favalli M., Isola I., Tarquini S. and Boschi E. (2007). Lava flow identification and aging by means of lidar intensity: Mount Etna case. *Journal of Geophysical Research, Solid Earth*, 112(B2).
- Mazzarini F., Favalli M., Isola I., Neri M. and Pareschi, M. T. (2008). Surface roughness of pyroclastic deposits at Mt. Etna by 3D laser scanning. *Annals of Geophysics* 51(5-6), 813-822.
- McKean J. and Roering J. (2004). Objective landslide detection and surface morphology mapping using high-resolution airborne laser altimetry. *Geomorphology* 57(3), 331–351.

- Miyamoto H. and Sasaki, S. (1997). Simulating lava flows by an improved cellular automata method. *Computers and Geosciences* 23(3), 283–292.
- Mitasova H., Harmon R.S., Weaver K.J., Lyons N.J. and Overton M.F. (2012). Scientific visualization of landscapes and landforms. *Geomorphology* 137(1), 122–137.
- Nannipieri L., Fornaciai A., Favalli M., Cipolla V. (2016). Manuale delle operazioni con SAPR e analisi del rischio. *Rapporti Tecnici INGV*, 346, ISSN 2039-7941. <http://www.ingv.it/editoria/rapporti/2016/rapporto346/>
- Nelson A., Reuter H.I. and Gessler P. (2009). DEM production methods and sources. *Developments in soil science* 33, 65-85.
- Neri, M. and Acocella, V. (2006). The 2004–2005 Etna eruption: implications for flank deformation and structural behaviour of the volcano. *Journal of Volcanology and Geothermal Research* 158(1), 195-206.
- Neri M., Behncke B., Burton M., Giammanco S., Pecora E., Privitera E. and Reitano D. (2006). Continuous soil radon monitoring during the July 2006 Etna eruption. *Geophys. Res. Lett.* 33, L24316.
- Neri M., Acocella V., Behncke B., Giammanco S., Mazzarini F. and Rust D. (2011). Structural analysis of the eruptive fissures at Mount Etna (Italy). *Annals of Geophysics* 54 (5), 464–479.
- Neri M., De Maio M., Crepaldi S., Suozzi E., Lavy M, Marchionatti F, Calvari S., Buongiorno M.F. (2017). Topographic Maps of Mount Etna’s Summit Craters, updated to December 2015. *Journal of Maps*, in review.
- Nichols R.L. (1939). Viscosity of lava. *The Journal of Geology* 47(3), 290-302.
- Nouwakpo S.K., Weltz M.A. and McGwire K. (2015). Assessing the performance of structure-from-motion photogrammetry and terrestrial LiDAR for reconstructing soil surface microtopography of naturally vegetated plots. *Earth Surface Processes and Landforms*. DOI: 10.1002/esp.3787
- Olaya V. (2009). Basic land-surface parameters. In: Hengl, T., Reuter, H.I. (Eds.), *Geomorphometry: Concepts, Software, Applications*. Elsevier, Amsterdam, pp. 141–169.
- Park S. and Iversen J.D. (1984). Dynamics of lava flow: Thickness growth characteristics of steady two-dimensional flow. *Geophysical Research Letters* 11(7), 641–644.
- De Reu J., Bourgeois J., Bats M., Zwertvaegher A., Gelorini V., De Smedt P., ... and Van Meirvenne M. (2013). Application of the topographic position index to heterogeneous landscapes. *Geomorphology* 186, 39-49.
- Richter N., Favalli M., de Zeeuw-van Dalssen E., Fornaciai A., da Silva Fernandes R.M, Rodriguez N.P., Levy J., Victória S.S. and Walter T.R. (2016). Lava flow hazard at Fogo Volcano, Cape Verde, before and after the 2014–2015 eruption. *Natural Hazards and Earth System Sciences Discussions* 16, 1925–1951.

- Robert B., Harris A., Gurioli G., Médard E., Sehlke A. and Whittington A. (2014). Textural and rheological evolution of basalt flowing down a lava channel. *Bulletin of Volcanology* 76(6), 824.
- Shary P.A. (1991). The second derivative topographic method. *The Geometry of the Earth Surface Structures*, 30–60.
- Shary P.A. (1995). Land surface in gravity points classification by a complete system of curvatures. *Mathematical Geology* 27(3), 373–390.
- Shary P.A. (2008). Models of topography. In *Advances in Digital Terrain Analysis* (pp. 29-57). Springer Berlin Heidelberg.
- Shepard M.K., Campbell B.A., Bulmer M.H., Farr T.G., Gaddis L.R. and Plaut J.J. (2001). The roughness of natural terrain: a planetary and remote sensing perspective. *Journal of Geophysical Research* 106, 32,777–32,795.
- Slatcher N., James M.R., Calvari S., Ganci G., Browning J. (2015). Quantifying effusion rates at active volcanoes through integrated time-lapse laser scanning and photography. *Remote Sensing* 7 14967–14987.
- Smith M.J. and Clark C.D. (2005). Methods for the visualisation of digital elevation models for landform mapping. *Earth Surface Processes and Landforms* 30, 885–900.
- Smith M.J. (2011). Chapter eight – digital mapping: visualisation, interpretation and quantification of landforms. In: Smith, M.J., Paron, P., James, S.G. (Eds.), *Developments in Earth Surface Processes*. Elsevier, Amsterdam, pp. 225–251.
- Snavely N. (2008). Bundler user’s manual.
- Sobel I. and Feldman G. (1973). A  $3 \times 3$  Isotropic Gradient Operator for Image Processing. In Duda, R., Hart, P., (Eds.), *Pattern Classification and Scene Analysis*. Wiley, New York, pp. 271–272.
- Spampinato L., Calvari S., Oppenheimer C. and Boschi E (2011). Volcano surveillance using infrared cameras. *Earth-Science Reviews* 106, 63–91.
- Sparks R.S.J., Pinkerton H. and Hulme G. (1976). Classification and formation of lava levees on Mt. Etna, Sicily. *Geology* 4(5), 269–271.
- Steyn D. (1980). The calculation of view factors from fisheye-lens photographs. *Atmos. Ocean* 18, 254–258.
- Stevens N.F., Wadge G. and Murray J.B. (1999). Lava flow volume and morphology from digitised contour maps: a case study at Mount Etna, Sicily. *Geomorphology* 28(3), 251–261.
- Stockwell R.G., Mansinha L. and Lowe R.P. (1996). Localization of the complex spectrum: the S transform. *IEEE transactions on signal processing* 44(4), 998–1001.
- Szeliski R. (2011). Structure from motion. In *Computer Vision* (pp. 303-334). Springer London.

- Tanguy J.C. and Kieffer G. (1977). The 1974 eruption of Mount Etna. *Bulletin Volcanologique*, 40(4), 239–252.
- Tarolli P. (2014). High-resolution topography for understanding Earth surface processes: opportunities and challenges. *Geomorphology* 216, 295–312.
- Tarquini S., Vinci S., Favalli M., Doumaz F., Fornaciai A. and Nannipieri L. (2012a). Release of a 10-m-resolution DEM for the Italian territory: Comparison with global-coverage DEMs and anaglyph-mode exploration via the web. *Computers and Geosciences* 38(1), 168–170.
- Tarquini S., Favalli M., Mazzarini F., Isola I. and Fornaciai A. (2012b). Morphometric analysis of lava flow units: case study over LIDAR-derived topography at Mount Etna, Italy. *Journal of volcanology and geothermal research* 235, 11–22.
- Tazieff, H. (1974). *The making of the earth: volcanoes and continental drift*. Saxon House.
- Tuffen H., James M.R., Castro J.M. and Schipper C.I. (2013). Exceptional mobility of a rhyolitic obsidian flow: observations from Cordón Caulle, Chile, 2011–2013. *Nature Communication* 2709.
- Ullman S. (1979). The interpretation of structure from motion. *Proceedings of the Royal Society of London B: Biological Sciences* 203(1153), 405–426.
- Umino S., Nonaka M. and Kauahikaua J. (2006). Emplacement of subaerial pahoehoe lava sheet flows into water: 1990 Kupaianaha flow of Kilauea volcano at Kaimu Bay, Hawai'i. *Bulletin of Volcanology* 69, 125–139.
- Vicari A., Ciraudò A., Del Negro C., Herault A. and Fortuna L. (2009). Lava flow simulations using discharge rates from thermal infrared satellite imagery during the 2006 Etna eruption, *Natural Hazard* 50, 539-550.
- Walker G.P.L., Huntingdon A.T., Sanders A.T. and Dinsdale J.L. (1973). Lengths of lava flows and discussion. *Philosophical Transactions of the Royal Society of London A: Mathematical, Physical and Engineering Sciences* 274(1238), 107–118.
- Wehr A. and Lohr U. (1999). Airborne laser scanning—an introduction and overview. *ISPRS Journal of photogrammetry and remote sensing* 54(2), 68-82.
- Wehr A. (2009). LiDAR systems and calibration. *Topographic Laser Ranging and Scanning Principles and Processing*, 129.
- Westoby M.J., Brasington J., Glasser N.F., Hambrey M.J. and Reynolds J.M. (2012). ‘Structure-from-Motion’ photogrammetry: A low-cost, effective tool for geoscience applications. *Geomorphology* 179, 300–314.
- Wilson J.P. and Gallant, J. C. (Eds.), 2000. *Terrain analysis: principles and applications*. Wiley.
- Woodcock N.H. (1977). Specification of fabric shapes using an eigenvalue method. *Geological Society of America Bulletin* 88(9), 1231–1236.

- Wright R., Flynn L.P. and Harris A.J. (2001). Evolution of lava flow-fields at Mount Etna, 27–28 October 1999, observed by Landsat 7 ETM+. *Bulletin of Volcanology* 63,1–7.
- Yokoyama R., Shirasawa M. and Pike R.J. (2002) Visualizing topography by openness: a new application of image processing to digital elevation models. *Photogrammetric engineering and remote sensing* 68(3), 257–266.
- Zakšek K., Oštir K. and Kokalj Ž. (2011) Sky-view factor as a relief visualization technique. *Remote Sensing* 3(2), 398–415.
- Zevenbergen L.W. and Thorne C.R. (1987). Quantitative analysis of land surface topography. *Earth surface processes and landforms* 12(1), 47–56.